(ATINER)

Athens Journal of Sciences

(ATINER)

Volume 6, Issue 1, March 2019

Articles

ATHENS INSTITUTE FOR EDUCATION AND RESEARCH
A World Association of Academics and Researchers
8 Valaoritou Str., Kolonaki, 10671 Athens, Greece.
Tel.: 210-36.34.210 Fax: 210-36.34.209
Email: info@atiner.gr URL: www.atiner.gr
(ATINER) Established in 1995 (ATINER)

Mission

ATINER is a ***World Non-Profit Association*** of Academics and Researchers based in Athens. ATINER is an independent **Association** with a **Mission** to become a forum where Academics and Researchers from all over the world can meet in Athens, exchange ideas on their research and discuss future developments in their disciplines, **as well as engage with professionals from other fields**. Athens was chosen because of its long history of academic gatherings, which go back thousands of years to *Plato's Academy* and *Aristotle's Lyceum*. Both these historic places are within walking distance from ATINER's downtown offices. Since antiquity, Athens was an open city. In the words of Pericles, **Athens*"...is open to the world, we never expel a foreigner from learning or seeing".*** ("Pericles' Funeral Oration", in Thucydides, *The History of the Peloponnesian War).* It is ATINER's **mission** to revive the glory of Ancient Athens by inviting the World Academic Community to the city, to learn from each other in an environment of freedom and respect for other people's opinions and beliefs. After all, the free expression of one's opinion formed the basis for the development of democracy, and Athens was its cradle. As it turned out, the Golden Age of Athens was in fact, the Golden Age of the Western Civilization. *Education* and *(Re)searching* for the 'truth' are the pillars of any free (democratic) society. This is the reason why *Education* and *Research* are the two core words in ATINER's name.

The Athens Journal of Sciences
ISSN NUMBER: 2241-8466- DOI: 10.30958/ajs
Volume 6, Issue 1, March 2019
Download the entire issue (PDF)

Athens Journal of Sciences
Editorial and Reviewers' Board

President's Message

All ATINER's publications including the e-journals are open access without any costs (submission, processing, publishing, open access paid by authors, open access paid by readers etc.) and are independent of the presentations made at any of the many small events (conferences, symposiums, forums, colloquiums, courses, roundtable discussions) organized by ATINER throughout the year. The intellectual property rights of the submitted papers remain with the author.

Before you submit, please make sure your paper meets some basic academic standards, which include proper English. Some articles will be selected from the numerous papers that have been presented at the various annual international academic conferences organized by the different divisions and units of the Athens Institute for Education and Research.

The plethora of papers presented every year will enable the editorial board of each journal to select the best ones, and in so doing, to produce a quality academic journal. In addition to papers presented, ATINER encourages the independent submission of papers to be evaluated for publication.

The current issue of the Athens Journal of Sciences (AJS) is the first issue of the sixth volume (2019). The reader will notice some changes compared with the previous issues, which I hope is an improvement. An effort has been made to include papers which extent to different fields of the Natural and Formal Sciences. One paper is related to environmental science, one to computer science, one to energy science, and the other to chemistry and corrosion science.

Gregory T. Papanikos, President
Athens Institute for Education and Research

Athens Institute for Education and Research

A World Association of Academics and Researchers

7th Annual International Conference on Chemistry
22-25 July 2019, Athens, Greece

The Chemistry Unit of ATINER, will hold its **7th Annual International Conference on Chemistry, 22-25 July 2019, Athens, Greece** sponsored by the Athens Journal of Sciences. The aim of the conference is to bring together academics and researchers of all areas of chemistry and other related disciplines. You may participate as stream organizer, presenter of one paper, chair a session or observer. Please submit a proposal using the form available (https://www.atiner.gr/2019/FORM-CHE.doc).

Academic Members Responsible for the Conference

- **Dr. Ellene Tratras Contis**, Head, Chemistry Unit, ATINER & Professor of Chemistry, Eastern Michigan University, USA.
- **Dr. Nicolas Abatzoglou**, Head, Environment Unit, ATINER & Professor, Department of Chemical & Biotechnological Engineering, University of Sherbrook, Canada, Chair Pfizer, PAT in Pharmaceutical Engineering, Director GREEN-TPV and GRTP-C & Pwelcomes.

Important Dates

- Abstract Submission: **25 March 2019**
- Acceptance of Abstract: 4 Weeks after Submission
- Submission of Paper: **24 May 2019**

Social and Educational Program

The Social Program Emphasizes the Educational Aspect of the Academic Meetings of Atiner.

- Greek Night Entertainment (This is the official dinner of the conference)
- Athens Sightseeing: Old and New-An Educational Urban Walk
- Social Dinner
- Mycenae Visit
- Exploration of the Aegean Islands
- Delphi Visit
- Ancient Corinth and Cape Sounion

Conference Fees

Conference fees vary from 400€ to 2000€
Details can be found at: https://www.atiner.gr/2019fees

Athens Institute for Education and Research

A World Association of Academics and Researchers

7th Annual International Conference on Physics
22-25 July 2019, Athens, Greece

The Physics Unit of ATINER, will hold its **7th Annual International Conference on Physics, 22-25 July 2019, Athens, Greece** sponsored by the Athens Journal of Sciences. The aim of the conference is to bring together academics and researchers of all areas of physics and other related disciplines. You may participate as stream organizer, presenter of one paper, chair a session or observer. Please submit a proposal using the form available (https://www.atiner.gr/2019/FORM-PHY.doc).

Important Dates

- Abstract Submission: **25 March 2019**
- Acceptance of Abstract: 4 Weeks after Submission
- Submission of Paper: **24 May 2019**

Academic Member Responsible for the Conference

- **Dr. Ethel Petrou**, Academic Member, ATINER & Professor and Chair, Department of Physics, Erie Community College-South, State University of New York, USA.
- **Dr. Bala Maheswaran**, Head, Electrical Engineering Unit, ATINER & Professor, Northeastern University, USA.

Social and Educational Program

The Social Program Emphasizes the Educational Aspect of the Academic Meetings of Atiner.

- Greek Night Entertainment (This is the official dinner of the conference)
- Athens Sightseeing: Old and New-An Educational Urban Walk
- Social Dinner
- Mycenae Visit
- Exploration of the Aegean Islands
- Delphi Visit
- Ancient Corinth and Cape Sounion

More information can be found here: https://www.atiner.gr/social-program

Conference Fees

Conference fees vary from 400€ to 2000€
Details can be found at: https://www.atiner.gr/2019fees

Matching the Spatial Distribution of Upland and Lowland Pollen Grains with the Temperature and Humidity in the Columbia Basin

By Peter Siska[*]
Vaughn Bryant[†]
I-Kuai Hung[‡]
Pierre Goovaerts[♦]

Airborne pollen is a highly influential factor in biosphere and also in anthroposphere; pollen is a source of food for numerous species of animals and is responsible for the transfer of genetic material in the biosphere. Fossil pollen grains are indicators of past climatic changes and play an important role in forensic analysis. Pollen is also an allergen causing rhinitis. In order to properly identify pollen and plant relationships, detailed studies of pollen distribution and accumulation in the environment are needed. In this paper, special attention was paid to the geographic distribution of pollen with respect to biologic and geomorphic conditions. Geomorphology (size and shapes) of land features is closely connected to changes in temperature, moisture, air pressure, wind speed, wind direction and precipitation, which in turn affect the distribution and dynamic of biomass change. The spatial patterns of two bioclimatic variables: temperature and evapotranspiration were studied with respect to the distribution of arid and forest pollen. Results indicate a significant relationship between elevation, pollen depositions patterns, and changes in bioclimatic parameters. This relationship exhibits a concentric pattern which reflects a basin geomorphology. The importance of understanding the correlation between pollen dispersion patterns and actual vegetation communities is one of the essential means used to understand paleo-vegetative records, and it can become an important guide in geolocation questions related to using pollen as a forensic tool.

Keywords: *Ecosystem, Geomorphology, Geostatistics, Pollen Grains, Spatial Analysis.*

Introduction

The purpose of this research is to determine the differences between spatial distribution patterns for two pollen groups and the way they represent basin geomorphology. In addition, the study looks at the pollen transport on the slopes

[*]Professor, Louisiana State University, USA.
[†]Professor, Texas A&M University, USA.
[‡]Professor, Stephen F. Austin University, USA.
[♦]Chief Scientist, BioMedware Inc., USA.

of the surrounding mountains. Pollen grains are transported in the atmosphere away from their source by laminar or turbulent flows of air. This transport is heavily influenced by the local geomorphology and consequently depends on bioclimatic conditions. A basin is a unique geomorphic feature that consists of two distinct parts: (a) - the outer and elevated natural wall that rises up to the drainage divide enclosing an inner space and (b) - the basin floor. This geomorphic structure has developed its own climatic and biologic identity resembling a closed natural system consisting of a unique microclimate. The basic hypothesis is that pollen grains produced at the bottom of the basin stay there and move only within the basin perimeter, but pollen grains from the elevated slopes also accumulate in larger amounts on the basin floor. This study focuses on the ecosystems in the Columbia Basin, which resembles a natural, elongated bowl that extends in a roughly east-west direction in the northwestern part of the United States. The lower part of the basin is covered by thick basalt deposits that provide valuable minerals to a variety of plants in this ecosystem. The geomorphology of the studied area dictates the tight relationship between the basin microclimate and the biosphere. Due to the high wall of Cascade Mountains in the west, the incoming moisture from Pacific Ocean is blocked and the central part of the basin remains dry; the precipitation gradually increases with elevation, especially in the eastern part of the basin. The variability of the soils' physical and chemical characteristics depends on the lithology. Basalt underlies the entire bottom of the Columbia Basin, and its breakdown and disintegration causes the release of minerals into the pedosphere. The weathering of this material mixed with sand, silt and loess deposited during and immediately after the Wisconsin Glacial Period of the Late Quaternary results in a soil parent material that is rich in minerals and continues to influence ecosystems today.

The first pollen study happened more than a century ago when Lennart von Post recovered pollen from buried deposits and compared them with samples of modern pollen grains found in different types of plant communities (Fries 1967). What he discovered would lay the groundwork for the field of pollen analysis and for the application of using pollen spectra from modern pollen environments (called pollen prints) as analogs for interpreting past vegetation cycles (Manten 1967). During the decade since it was first developed, palynologists depended on modern pollen data to form qualitative and intuitive interpretations of fossil pollen analyses of buried sediments. One thing became clear from the beginning of the study by von Post (1916), there is not a 1:1 relationship between what one finds in the pollen record of a plant community and the actual ratios of the major plants growing in that same community. Experiments and research through decades of study revealed that some plant genera and species such as the grasses, conifers, oaks, elm, ash, ragweed, and many others produce and disperse millions of pollen grains into the atmosphere because they use a type of pollination, wind-pollination, which is haphazard and few pollen grains actually reach their intended destination and complete fertilization. This means that millions and even billions of spent pollen grains fall to the surface in a coating called "the pollen rain." Studies also noted that other types of plants, such as roses, sunflowers, carnations, tulips, and others rely on insects such as bees, wasps, and butterflies, or other

means (i.e., bats, humming birds, sugar glider, beetles, etc.) to carry pollen from one plant to another of the same species. This second method is highly efficient and the plants need to produce smaller amounts of pollen that normally do not become airborne until the flowers die. These factors are what makes it impossible to construct a true 1:1 relationship of the pollen rain to the actual plants that produced the pollen; nevertheless, with modern statistical methods, palynologists believe they can resolve this problem.

Palynologists soon discovered there were other factors that influenced the distribution of pollen in the landscape. Wind currents, humidity, temperature, ground surface obstacles including rocks, mountains, forests, and manmade building structures could divert and/or trap certain types and amounts of dispersed pollen and thus remove it from the normal pollen rain (Tauber 1967). Most important was the adiabatic lapse rate during and immediately after the dispersion of pollen from anthers. The lapse rate varies strongly with temperature, and moisture, which creates the temperature profile of the atmosphere (Steiner et al. 2015). Thus, high convection currents can be created by surface radiation and a high adiabatic lapse during dry conditions, while inversions can trap cold air below streams of hot air suppressing pollen dispersion, especially in valleys and basins. Forest fires, timber cutting, earthquakes, tsunamis, and floods also effect the distribution of pollen that has been dispersed. Hurricanes, tornadoes, and strong winds can recycle pollen previously deposited on the surface and carry it to new locations, making interpretations about the original plant communities difficult and sometimes confusing (Liu and Fearn 2000).

In the Columbia Basin, over 100 samples are recorded in the North American Pollen Database (Whitmore et al. 2005) as well as more than 60 bioclimatic variables covering 130 major pollen taxa in North America. The Columbia Basin and adjacent slopes contain records for 44 of the 130 plant pollen types scattered throughout the bottom and adjacent slopes around the basin. In this project, the pollen count data were grouped into two categories: basin floor (lowland pollen) and upland pollen. The lowland group is represented by *Artemisia*, *Aster*X, Chenoams (Amaranthaceae) and Poaceae. These are the main pollen producers. They are located mostly at the bottom of the Columbia Basin where drier conditions support the growth of these species. In contrast, the upland group consists of *Abies, Alnus*X, *Betula, Larix, Picea, Pinus* and *Tsuga* – tree taxa. The upland environment is dominated by lower temperatures, higher evapotranspiration regimes and higher precipitation levels. In addition, geomorphology is mostly composed of slope gradients and a variety of slope aspects that change continuously around the basin, leading to the reception of different types of solar radiation. Therefore, this research underlines the connectivity between geomorphic and bioclimatic characteristics; even subtle changes in terrain morphology can change the heat and moisture distribution as well as have an impact on the local and macro-scale.

Literature Review

Much attention has been paid in literature to the pollen records of the basin floor in the Columbia Basin (Mack and Bryant 1974, Barnosky 1984, Mack et al. 1996). These studies indicate that the mostly treeless floor has been dominated by *Artemisia* pollen for the last 100 thousand years. In addition, the phytolith and pollen record in this area near the center of the basin confirm the existence of an alternating xeric *Festuca-Poa* and mesic *Festuca-Koeleria* grassland vegetation (Blinnikov et al. 2002). Pollen deposition in arid areas has been studied in other regions of the world. For example, five major pollen types (Cheno-Ams (Amaranthaceae), Poaceae, *Juniperus*, *Pinus, and Quercus*) in the Big Bend desert ecosystem were analyzed spatially in relationship with the source vegetation from the desert floor and the nearby Chisos Mountains (Siska et al. 2001). Similarly, in the Quidam Basin of the Tibetan Plateau, *Artemisia* pollen and Cheno-Ams were studied using the relative representation index and principal component analysis (Zhao and Herzschuh 2009). The correlation between pollen dispersion and two climatic variables (temperature and moisture) is one of the most common themes in pollen literature. Minckley and Whitlock (2000) studied the distribution of pollen grains along the gradients of temperature and effective moisture in the western USA. They determined that east of the Cascade Mountain Range in the basin floor, shrub steppe and woodlands dominate and the effective moisture is low. In that rain shadow area, *Artemisia*, Cupressaceae and *Pinus* pollen are dominant. In contrast, in the higher areas of higher effective moisture, *Pinus*, *Abies* and *Picea* pollen are common. The humidity and temperature have a strong influence on microsporangium dehiscence and pollen dispersal; for example, this is documented in studies of *Cedrus deodora* in the Himalayas (Khanduri and Sharma 2002). Temperature and humidity also have an impact on the daily pollen concentrations of olive tree (*Olea europaea*) pollen in the Mediterranean region (Recio et al. 1997).

Perhaps, Siska and Polacik (2014) have conducted the most comprehensive work that relates to many pollen types in diverse bioclimatic conditions in the Columbia Basin. Using a factorial analysis of 44 pollen types and 69 bioclimatic variables, they delineated homogeneous environmental regions in the basin. In a basin environment which is usually surrounded by a backdrop of mountains, a turbulent flow of air causes pollen deposition to move uphill or downhill. According to Frei (1997), local pollen grains can be easily transported over 2,000 m high mountain slopes in the complex topography of the Swiss Alps. For example, the *Castanea* pollen that was dispersed by plants at low elevations on the southern slopes of the Alps was trapped at the location of Guetsch, Switzerland (2,300 m). Therefore, people suffering from allergic rhinitis may also be exposed to large quantities of pollen even at high elevations in the Alps. When pollen grains are ruptured due to a high humidity environment, numerous microscopic sub-pollen particles (SPPs) are created. These microscopic SPPs can form a cloud and remain at high altitudes in the atmosphere while travelling long distances (Steiner et al. 2015). Moreover, pollen dispersal in a basin environment has its own characteristics. Prentice (1985) modified Sutton's equation and predicted that

the basin's pollen source area is a function of basin size and deposition velocity of pollen types. Both Sutton's and Prentice's models assume continuity in pollen dispersal. Jackson and Lyford (1999) based their dispersion model on Gaussian puffs, due to the nature of how pollen leaves anthers in a series of "puffs" rather than as one continuous type of emission. Pollen is also one of the most favorite subjects to visualize as indicated in the work of Siska et al. (2012) and Desjardins et al. (2017).

Methodology

One of the most important analytical tools for characterizing the spatial distribution of pollen is geostatistics. Since pollen grains are microscopic particles invisible to the human eye, interpolation methods are needed to reveal the patterns of spatial distribution of different types of pollen grains in order to know what and where these quantities are accumulating on the ground. Geostatistics provides a set of statistical tools that take into account the spatial relationship between pollen counts and predicts the values at unsampled locations under the constraints of unbiasedness and minimum error variance (Goovaerts, 1998). A spatial structure is expected according to the first law of geography stating that pollen counts that are close to each other in space are more alike than those further apart. The presence of such a spatial structure is a prerequisite to the application of geostatistics, and its description is a preliminary step towards spatial prediction. In geostatistical literature, spatial patterns are usually described in terms of dissimilarity among the observations as a function of the separation distance, using a curve called the semivariogram. In this project, we describe the spatial structure by fitting cubic variogram models to both upland and basin floor pollen grain counts. The cubic variograms are in the form:

$$\gamma(\mathrm{h}) = \begin{cases} c_0 \left[7\left(\frac{h}{a_0}\right)^2 - \frac{35}{4}\left(\frac{h}{a_0}\right)^3 + \frac{7}{2}\left(\frac{h}{a_0}\right)^5 - \frac{3}{4}\left(\frac{h}{a_0}\right)^7 \right] & \text{for } h \le a_0 \\ c_0 & \text{for } h > a_0 \end{cases}$$

The existence of this spatial correlation allows for the interpolation of pollen data at locations where no samples were collected. Kriging is a generic name adopted by geostatisticians for a family of generalized least-squares regression algorithms. Like straightforward interpolation methods, such as inverse distance methods, kriging estimates the unknown value as a weighted average of data collected at neighboring locations. It is apparent that there is a significant variation in the local means of pollen counts across the study area, but ordinary kriging (OK) allows one to account for local variation in the mean by limiting the domain of stationarity to the local neighborhood centered on the location being estimated (Goovaerts, 1998). The ordinary kriging equation is then:

$$Z_{OK}(u) = \sum_{\alpha=1}^{n} \lambda_\alpha \; Z(u_\alpha) + \left(1 - \sum_{\alpha=1}^{n} \lambda_\alpha\right) m(u)$$

where lambda represents kriging weights, Z_{OK} are the kriging estimates and $Z(u_\alpha)$ are the sample values at locations u_α. By forcing the kriging weights to sum to one, the system is then radically simplified and the knowledge of the mean value $m(u)$ is no longer necessary.

Besides using geostatistical methods, the zonal statistic function was used to calculate the amount of pollen grains in each land use zone. In addition to computing the sum of pollen grains in each land use category, the mean, variance, minimum, maximum amounts of pollen, then range and density per square kilometer of pollen grains were also calculated. The main contribution of this analysis is to understand pollen and its source relationships. This analysis also answers the question about what quantities of pollen accumulate in the areas that are dominantly inhabited by the source vegetation. It is assumed that the largest amount of pollen will be dispersed close to the plant of dispersal. While this intuitive knowledge regarding the largest amount of pollen deposition near its own source region is often confirmed, the proportion of the pollen that accumulates elsewhere is often unknown. Therefore parallel mapping of pollen and vegetation was conducted and the amount of pollen grains was calculated in every source plant pixel. In an effort to establish more specific pollen-source relationships, two representatives from both groups were selected for zonal analysis: Cheno-Ams for the lowland (basin floor) pollen and PineX from upland group; these were chosen for their prolific pollen production.

Results

The variograms show a strong spatial structure that reflects the natural processes operating in the Columbia Basin region as well as a parabolic behavior at the origin, indicating continuous changes in space. Both variograms reach a sill at a similar range a_0, i.e., the distance beyond which pollen counts become spatially uncorrelated (Figure 1).

Figure 1. *Cubic Variograms of the Basin Floor* (left) *Upland Pollen Groups* (right)

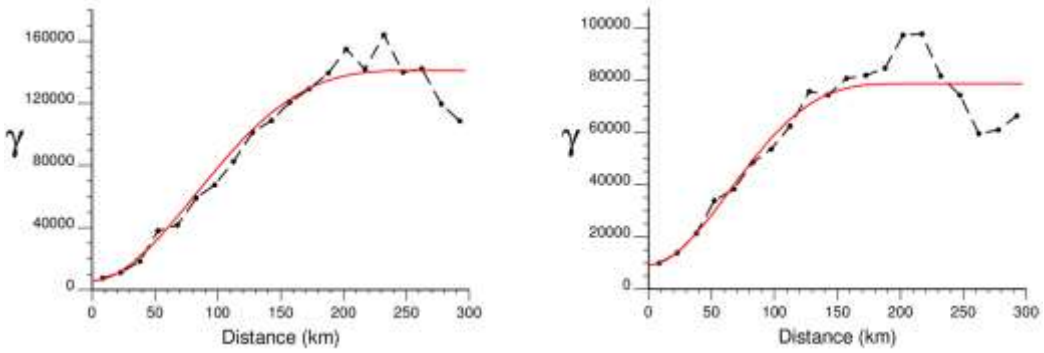

Maps of kriging estimates (Figure 2) highlight a significant difference in spatial patterns between basin floor pollen assemblages and upland pollen deposition. For the lowland group, dominating concentric patterns of pollen accumulation reveal the influence of the basin geomorphology. This is the result of the prevailing vegetation cover, basin morphology and wind influence. The lower portion of the prevailing wind system is from the southwest area, which is forced to turn along the slopes of the adjacent Cascade Mountains in a rotating fashion inside the basin interior. As the speed decreases at the end of the rotation, the pollen rain drops in the central and north-central part of the basin. Pollen accumulation is at its highest near the confluence of two major rivers (the Snake and Columbia Rivers at Kennewick). On the other hand, the spatial distribution of upland pollen indicates a very different pattern. In most areas of the Columbia Basin, the spatial distributions of upland and lowland pollen are exactly opposite. The central and north central parts of the basin contain the smallest counts of upland pollen with some overlap in the southeastern part. This area with low amounts of upland pollen coincides with the area where the amount of lowland pollen is the highest. On the other hand, the eastern and southeastern part of the Columbia Basin is heavily overloaded with upland pollen grains, while the lowland pollen counts in those areas are very low. Finally, the upland and lowland pollen amounts vary similarly in the third sub region with both groups exhibiting low pollen deposition and accumulation. This southwestern area begins roughly north of Highway 84 and continues in a southern direction, and indicating a significant decrease of both upland and basin types of pollen; therefore, there is a stronger positive geographic relationship between upland and lowland pollen counts. The explanation for the existence of these three sub-regions can be partially found in the matching pollen distribution patterns with their parent plant sources. Figure 3, shows the distribution of vegetation cover in the Columbia Basin.

Figure 2. *Spatial Distribution of Basin Floor* (left) *Upland Pollen Groups (right)*

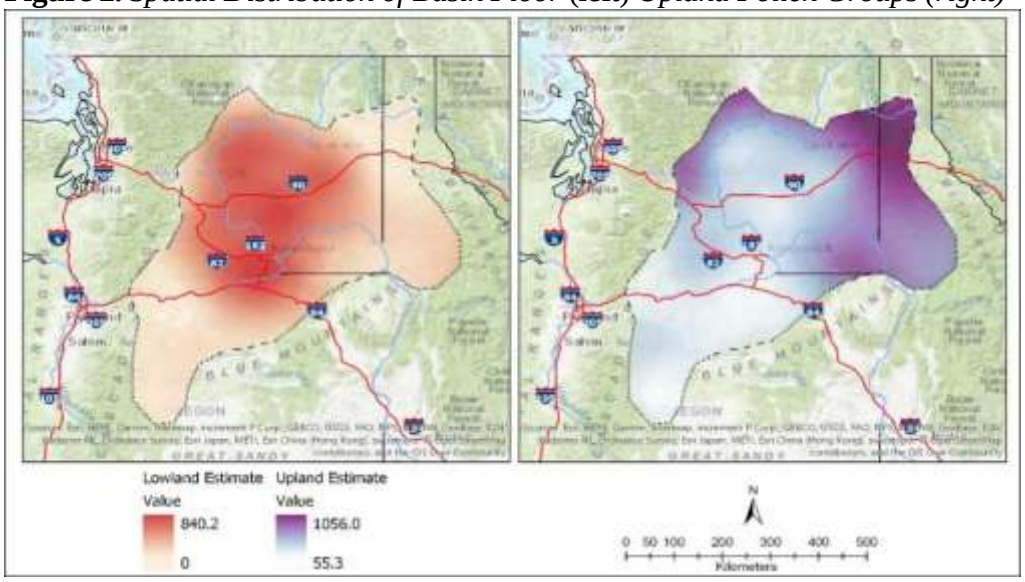

Figure 3. *National Landuse and Landcover Vegetation Categories*

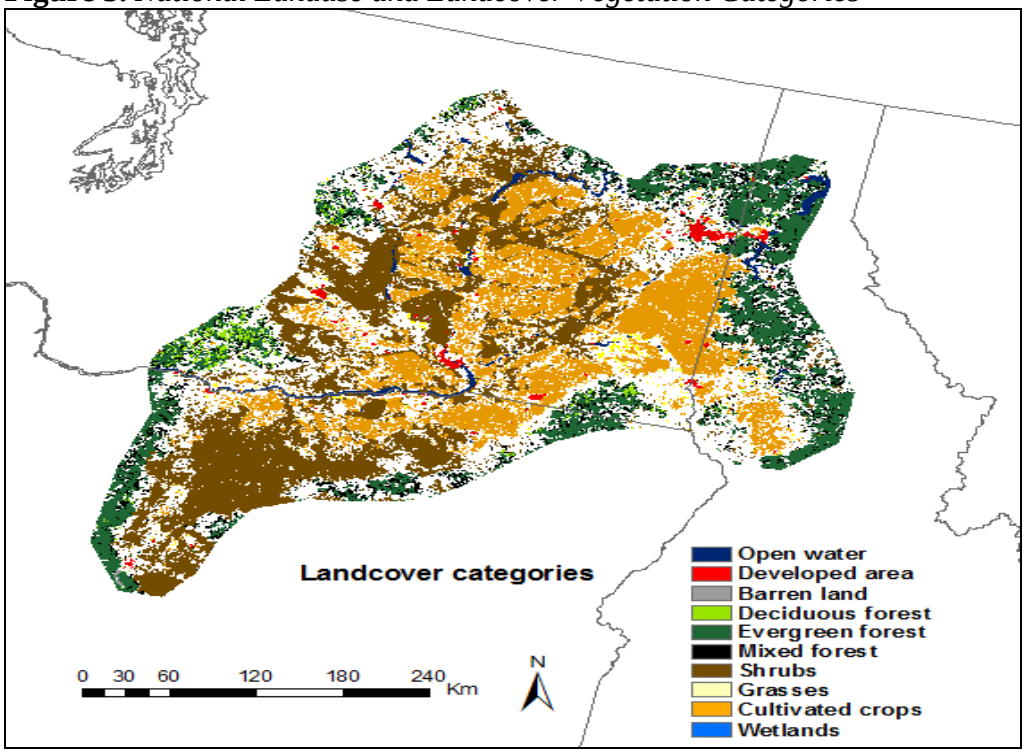

The land use zones (vegetation types) are represented by fifteen categories and zonal statistic function computes the quantities of selected pollen types in each land use category. These categories are: the open water category (code 11) that includes all areas of open water with less than 25 percent vegetation or the soil cover, the open space developed areas (code 21) that include a mixture of construction work and lawn grasses and less than 20% of impervious surfaces caused partly by single family housing, golf courses, parks and recreation places. The category with low intensity developed areas (code 22) consists from impervious surfaces (20-49%) and single-family housing units. The medium intensity developed areas (code 23) have typically between 50-79% impervious surfaces and consists of mostly single family housing units. The last high intensity developed category (code 24) includes urban development with a high density of population, apartment complexes, condensed single housing units, commercial, and industrial areas which contribute to impervious surfaces that occupy between 80 to 100% of the total area. The category of barren land areas (code 31) includes bedrock, desert pavement, a variety of other rock material, strip mines, and sand dunes where the vegetation represents less than 15 percent of the total area. The next category is the deciduous forest (code 41) which occupied a less significant amount of space than the evergreen forest (code 42). It includes trees taller than five meters. The total extent of forests is more than 20 percent of the vegetation cover, and more than 75% of the tree species in this category maintain their leaves year around. Category 43 is dominated by mixed forest where trees are smaller than five meters and occupy more than 20% of the total vegetation cover.

The areas that are overgrown by shrubs (marked code 52) play one of the most significant roles in the Columbia Basin. Shrubs are less than five meter tall and occupy more than 20% of the total vegetation cover. The naturally grown grasses (code 71), on the other hand, occupy a smaller portion of the basin floor. They are dominated by grammanoid or herbaceous vegetation with more than 80% of the total population. Agriculture plays an important role in the vegetation system of the basin floor because it is based on irrigation. For mapping purposes the agricultural land use is divided into category 81 that includes pasture and hay areas with a grass-legume mixture planted for livestock, and category 82, that includes cultivated crops used for the production of corn, soybeans, vegetables, tobacco, cotton, orchards and vineyards. The crop vegetation accounts for more than 20% of total vegetation. Woody wetlands and palustrine shrub wetland (codes 90 and 91) occupy only small areas in the Columbia Basin.

The highest amount of upland pollen matches with the coniferous forest that extends along the western slope of the Bitterroot Mountains and the northern slopes of the Blue Mountains. This extension also proceeds to the southern slopes of the Thompson-Okanagan Rocky Mountains system. However, more than half of the Columbia Basin rim does not exhibit elevated amounts of upland pollen despite the fact that the land cover map indicates the existence of a coniferous forest in the northwestern part of the area. A corner of the Columbia Basin north of Highway 84 indicates low amounts of upland or lowland pollen in spite of the fact that there is a significant patch of deciduous forest. In fact, the complete southwestern region is characterized by a low amount of accumulated pollen (Figure 2). The main cause for this pattern is the southwestern winds that carry pollen grains towards the central part of the basin. In addition, the eastern slopes of the Cascades are overgrown with low pollen producers, as opposed to most conifers, such as hemlock and juniper. Therefore, the hypothesis that the rim of the basin will contain elevated amounts of coniferous pollen in all areas was not confirmed. As indicated in the literature review, two climatic parameters, temperature and humidity both have a significant impact on pollen dispersion. Therefore, two other environmental parameters were included into this analysis: temperature and evapotranspiration (Figure 4). On the other hand, the eastern part with its lower temperatures and high amount of upland pollen grains exhibits the highest loss of water through evapotranspiration. Perhaps the most complex area is the southwestern region that indicates low upland and lowland pollen accumulation and dispersal; this area also exhibits low temperatures. The loss of water through evapotranspiration by plants is one of the highest here (Figure 4). This area is covered by shrub vegetation and also has a streak of coniferous forest. The high level of evapotranspiration is attributed to the shrubs and shrub-steppe ecosystem. In this area, the shrub-steppe exhibits the most continuous spatial extent.

Figure 4. *Spatial Patterns of Temperature* (left) *Evapotranspiration* (right)

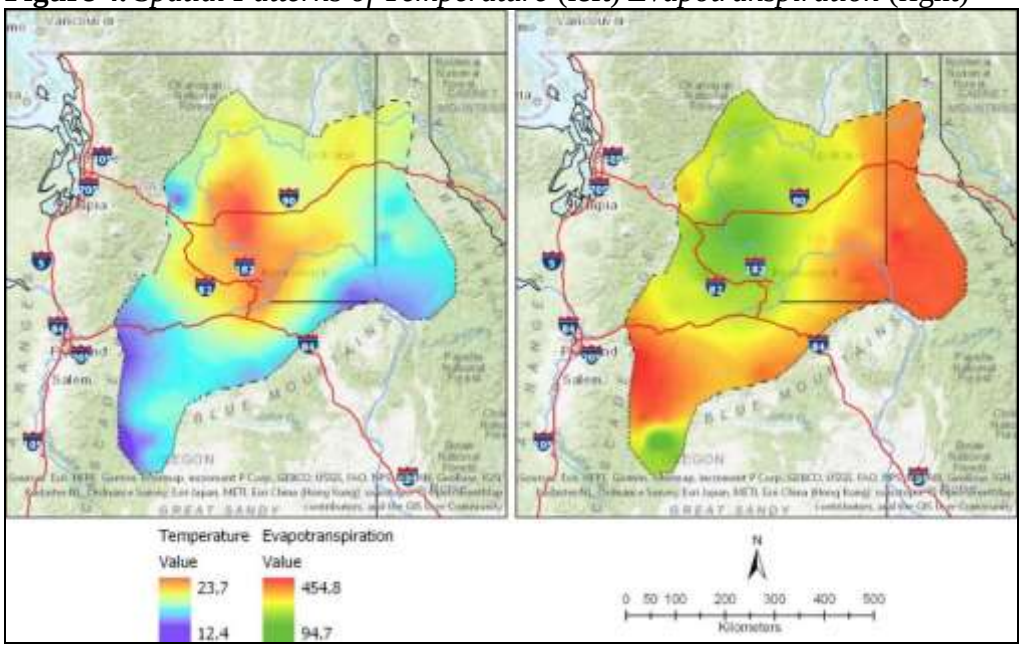

Discussion

One of the main goals of pollen spatial analysis is to identify the relationships between pollen sources and pollen grain dispersal as well as accumulation. In order to answer the question "where do pollen grains accumulate in relationship to their sources," parallel mapping was used and zonal statistics were calculated. In order to fulfill this task, land cover data – vegetation types (Homer et al. 2004) were used and pollen grains were counted within the boundaries of specific vegetation classes (Figure 3). The research indicates that in the interior of the Columbia Basin, most of the pollen grains coming from the lowland group, accumulate in the "shrub-scrub" vegetation category (corresponding to number 52 class on the land cover map); almost 25,000 pollen grains were measured in the samples with an average of 453 pollen grains per sample. There is also a significant deposition of grass and sedge pollen grains in the cultivated crops area (class 82). The total number of pollen grains was lower than the basin floor pollen, yet over 600 pollen grains on average were found in each sample. The deposition of the basin floor pollen in the evergreen forest was significantly lower than 3000 pollen grains in samples with an average of 113 pollen grains per sample; however, it also includes the contribution of semiarid pollen in the uplands. Significantly larger amounts of semiarid (basin floor) pollen accumulated in the developed open space land cover (class category 21) that could cause allergy problems to those sensitive to airborne pollen grains. The accumulation per sample (over 800 pollen grains per sample) indicated that it is the highest amount of pollen in the vegetation category groups. Other categories such as woody wetlands, grassland herbaceous, and barren land were represented by only very limited amounts of pollen. It was also surprising to find an insignificant

accumulation of basin floor pollen in the deciduous forests. The spatial analysis of upland pollen deposition revealed that sixty percent of upland pollen is almost equally deposited in three main vegetation zones. Twenty percent of the upland pollen grains were deposited in the evergreen forest areas (class 42) but 23.5% was deposited in the shrub and scrub category area (class 52) while 17.1% was deposited in the area of cultivated crops. As we noted, a large amount of upland pollen was actually deposited in the basin floor areas of the Columbia Basin. Over 10% of all pollen from the open spaces was also deposited with medium intensity in developed urban areas.

In order to establish pollen and source vegetation relationships in more detail, two representatives from both groups were selected and zonal statistics were used to quantify the accumulation of these two pollen types in all of the fifteen vegetation categories that play a significant role in the Columbia Basin. The first type is pollen from the family Amaranthaceae, which includes the former family Chenopodiaceae (previously called Cheno-Ams). These herbs and shrubs are one of the most common plant species found in the arid and semiarid areas. They also occupy the central part of the Columbia Basin floor. Figure 5 shows pollen grain densities in each of the land use-vegetation categories. As noted, the highest densities of the Cheno-Am type pollen accumulated in pastures and cultivated crops areas. Hence, agriculture was developed in places where the original plant species in the Amaranthaceae dominated. Agriculture can only exist in this area through irrigation. The developed regions also indicated high pollen densities of Cheno-Ams, another proof that urbanization encroaches into lowland pollen producers and the potential problem for rhinitis increases. The lowest amount of Amaranthaceae pollen is as expected in areas occupied by tree vegetation.

Figure 5. *The Density of Amaranthaceae Pollen (Cheno-Ams) in Vegetation Groups*

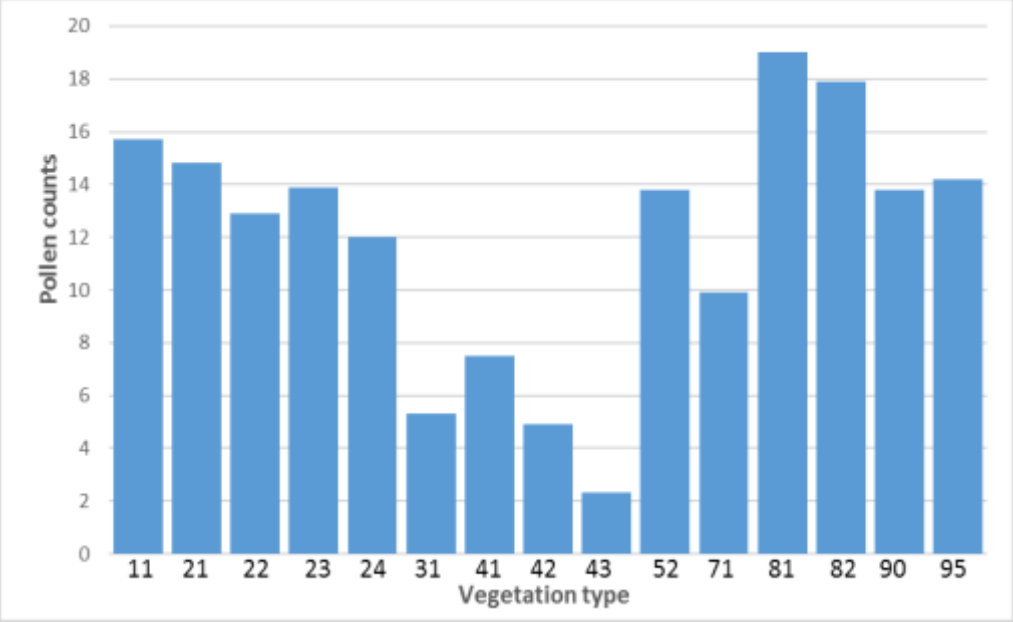

In terms of total pollen accumulation as indicated in Figure 7, there are only four main areas where Amaranthaceae pollen is deposited: (1) source plants (shrub/scrub category), (2) agricultural areas (category 82), (3) evergreen forests (category marked by letter 42), and (4) grassland-herbaceous areas (category 71). While Cheno-Ams pollen accumulation in the shrub/scrub, agricultural land, and grasslands is expected, the high pollen accumulation in the evergreen forest region is surprising. It shows the prevailing wind pattern. The laminar airflow from the southwestern area carries pollen in a west-east direction to the evergreen forests that dominate the eastern part of the Columbia Basin. It is the turbulent flow of air that takes this lowland pollen to a higher elevation and contributes to the creation of a transitional zone where a mixture of upland and lowland pollen grains occur. Therefore, this analysis is useful for understanding local wind patterns, pollen grain transport, and potential environmental pollution.

Pines are one of the largest pollen producing plant species on planet. This is confirmed by the density deposition of pine pollen per square kilometer compared to Cheno-Am pollen and by the total quantities of pollen grains in each vegetation zone (Figure 6). The largest densities of pine pollen grains are located in deciduous and evergreen forest areas that are dominated by trees taller than five meters, and there is a relatively small deposition in areas occupied by the Amaranthaceae species. However, there are still large pollen densities of pine pollen in areas that are occupied by grasses and herbs (category 71). In the pasture and grass zone is the density of Cheno-Am pollen naturally high; however, the pine pollen is also relatively high in grass zone.

Figure 6. *The Density of Pine Pollen in Vegetation Groups*

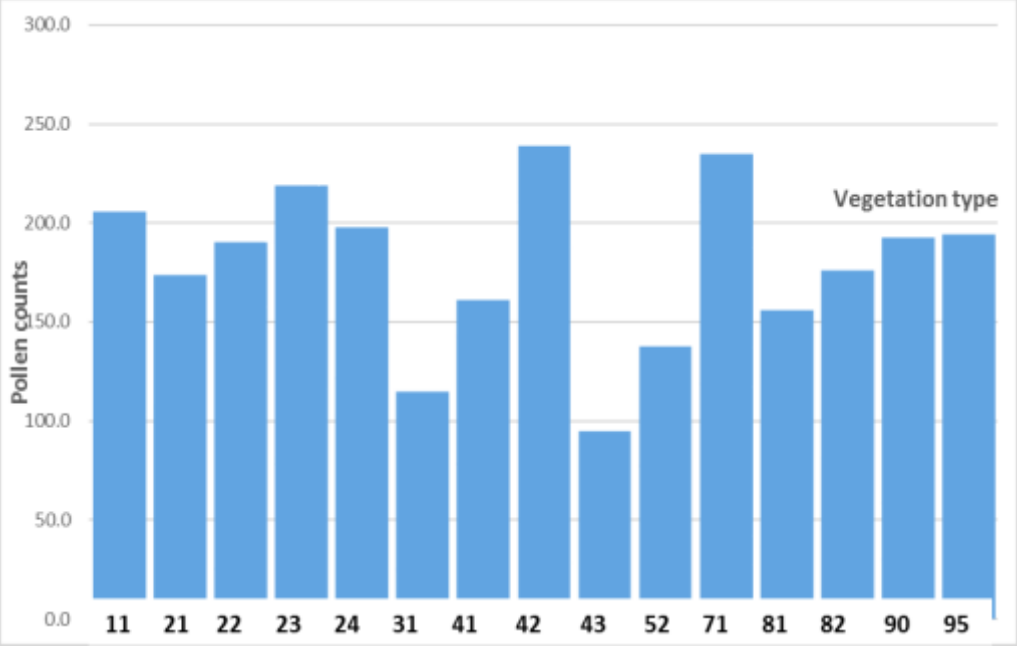

The urban areas and open water category receive about the same proportion of total pollen amounts from both groups (upland and lowland). Deciduous forests and mixed forests exhibit the smallest accumulation of pollen from both Cheno-

Ams and pine pollen. In the evergreen forest and shrub-scrub vegetation areas we observe an "ecologic pollen swap." This means that co-existence of pine and Cheno-Am pollen is a mirror image of respective source vegetation. In evergreen forest high density of pine pollen coexists with large amount of Cheno-Am pollen whereas in shrub-scrub areas high densities of Cheno-Am pollen coexist with large amount of pine pollen. This ecological "coexistence" between Cheno-Ams and pine pollen is a typical characteristic of the Columbia Basin and perhaps all dry basin ecosystems where geomorphology controls environment. Another interesting characteristic in Columbia Basin is the existence of transitional zone where significant mixing of the upland and lowland pollen grains is taking place. This "mixing" of pollen marks a special lowland-upland boundary where the basin floor is connected to the mountain backdrop. In the Columbia Basin, this boundary is between 400-700 meters in elevation. Finally, both types of pollen grains significantly contribute to agricultural areas where crop vegetation dominates landuse (Figures 7 and 8). This indicates that agriculture is occupying areas that were in the past supplied by pine and shrub-scrubs pollen grains. What used to be a zone of species competition has today been taken over by human activities. Therefore, there is a significant mixing here of naturally occurring pollen with agricultural plants pollen mainly corn, tobacco, cotton and orchards. The woody wetlands and emergent herbaceous wetland areas with perennial vegetation receives only a minimal amount of pollen from the Cheno-Ams and pine species, indicating a similarity in the upland-lowland pollen categories.

Figure 7. *The Total Sum of Amaranthaceae Pollen Grains in Individual Vegetation Categories*

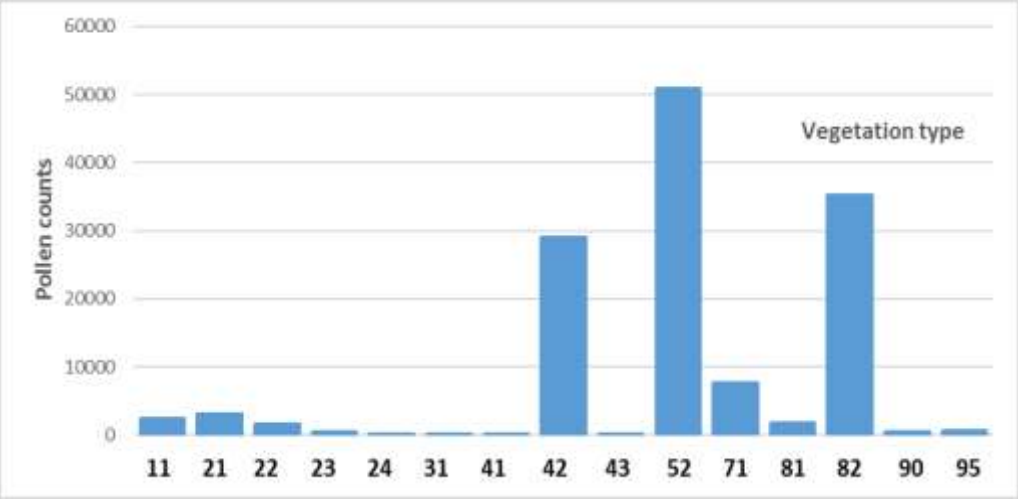

Another important aspect of this study was understanding the pollen accumulation patterns in this specific geomorphic setting (a basin) and the significance of the local bioclimatic influence. The importance of elevation is only implicitly deduced at this point. The elevation increases from the center of the basin to its sides in each direction. The spatial patterns of lowland/upland pollen grains, temperature, and evapotranspiration share clear similarities. Higher elevations in the basin slopes, especially in the eastern part, also show high

evapotranspiration values in the same region where coniferous forests with low temperatures are located. In those areas, there is an abundance of upland pollen. In contrast, at the center of the basin, lowland pollen is heavily accumulating in areas with the highest temperatures and lowest evapotranspiration. Agricultural land use and heavily based irrigation is causing the loss of moisture as well as affecting the natural regime of this dry, almost arid ecosystem. Temperature and humidity are also influencing the dehiscence of anthers and the release of pollen grains into the environment. With increasing elevation, the temperature decreases which slows down the microsporangium dehiscence and release of pollen into the atmosphere. This release is delayed by elevation on the slopes of rising mountains and contributes to the seasonal variability of pollen amounts in mountainous ecosystems.

Figure 8. *The Total Sum of Pine Pollen Grains in Individual Vegetation Categories*

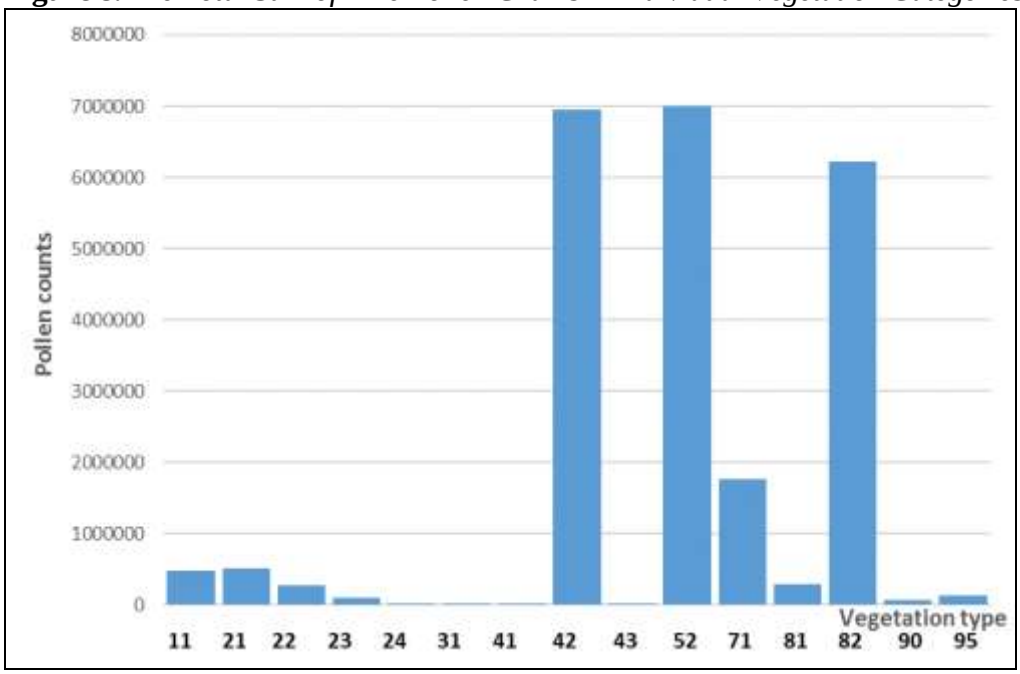

Conclusions

The spatial distribution of pollen deposition and accumulation was studied in relationship to temperature, evapotranspiration and geomorphological setting. This study confirmed that pollen is a sensitive component of the natural environment and its dispersion/accumulation in the soil is a function of the natural geomorphology that controls temperature, humidity, underground and surface water flow as well as wind patterns. In addition, the spatial distribution of pollen is also related to its producer sources (vegetation) that varies in elevation as well as geographically (Franklin and Dyrness 1988). The distribution of modern pollen rain with respect to pollen producers can also be used in paleo-environmental work relating to fossil pollen assemblages reflecting the patterns of past vegetation

and climatic changes (Minckley and Whitlock 2000). In this work, we determined that depositions and accumulations of pollen grains is a sensitive indicator of many environmental changes such as climate or biosphere. In addition, pollen grain depositions and accumulations mark important breakpoints in the relief that change the character of pollen deposition and therefore the local bioclimatic conditions. Therefore, geomorphology can be an important characteristic causing changes in the natural as well as social aspects of the environment and affects how natural and human systems adapt to life on this planet.

Further investigation is necessary to confirm the existence of a 400-700 meter elevation breakpoint that marks a significant change in the Columbia Basin environment. The study also revealed that especially people with severe pollen allergies should avoid the maximum quantities of pollen grains that fall in the basin area. The match between vegetation and pollen amounts is most noticeable in the basin floor and in the eastern part of the study area. The influence of a southwesterly wind pattern is visible in the spatial pattern of the upland pollen distribution that follows a typical southwest-northeast direction. The amount of pollen gradually changes on the slopes of the mountains where pollen grains are moved in both directions: upwards and downwards. The meeting place forms a special transitional zone of downslope-upslope accumulation and transport. This transitional zone in the Columbia Basin is between 400-700 meters in elevation. The existence of this transitional zone of pollen accumulation from upwards and downwards pollen transport is also mentioned in the Qaidam Basin (Zhao and Herzschuh 2009). It underlines the influence of geomorphic conditions on the biosphere, atmosphere and hydrosphere of the studied area.

Acknowledgements

The research by Dr. Goovaerts was funded by grant R44 ES022113-02 from the National Institute of Environmental Health Sciences. The views stated in this publication are those of the author and do not necessarily represent the official views of the NIEHS. Dr. Siska's research was partially funded by Centrum for scientific and technological information in Bratislava, Slovak Republic.

References

Barnosky CW (1984) Late Pleistocene and Early Holocene Environmental History of Southwestern Washington State U.S.A. *Canadian Journal of Earth Science* 21(6): 619-629.

Blinnikov M, Busacca A, Whitlock C (2002) Reconstruction of the Late Pleistocene Grassland of the Columbia Basin, Washington, USA, based on Phytolith Records in Loess. *Paleography, Paleoclimatology, Paleoecology* 177(1-2): 77-101.

Desjardins MR, Hohl A, Griffith A, Delmelle E (2017) Fine Scale Visualization of Pollen Concentrations across the Eastern United States: A Space-Time Parallel Approach. Technical Report. University of North Carolina. http://www.geocomputation.org/2017/papers/68.pdf.

Franklin JF, Dyrness CT (1988) *Natural Vegetation of Oregon and Washington.* Corvallis, OR: OSU Press.

Frei T (1997) Pollen Distribution at High Elevation in Switzerland: Evidence for Medium Range Transport. *Grana* 36(1): 34-38. DOI: 10.1080/00173139709362587.

Fries M (1967) Lennart von Post's pollen diagram series of 1916. *Rev. Palaeobotan. Palynol.* 4(1-4): 9-13.

Goovaerts P (1998) *Geostatistics for Natural Resources Evaluation.* NY: Oxford Univ. Press.

Homer C, Huang C, Yang LL, Wylie B, Coan M (2004) Development of 2001 National Land-Cover Database for the United States. *Photogramm Eng.Rem.S.* 70(7): 829-840. https://doi.org/10.14358/PERS.70.7.829.

Jackson ST, Lyford ME (1999) Pollen Dispersal Models in Quaternary Plant Ecology: Assumptions, Parameters, and Prescriptions. *Botanical Review* 65(1): 39-75.

Khanduri VP, Sharma CM (2002) Pollen Production, Microsporangium Dehiscence and Pollen Flow in Himalayan Cedar (Cedrus Deodara Roxb. Ex D. Don). *Annals of Botany* 89(5): 587-593.

Liu K, Fearn M (2000) Reconstruction of Prehistoric Landfall Frequencies of Catastrophic Hurricanes in Northwestern Florida from Lake Sediment Records. *Quaternary Research* 54(2): 238-245. https://doi.org/10.1006/qres.2000.2166.

Mack RN, Bryant V (1974) Modern Pollen Spectra from the Columbia Basin, Washington. *Northwest Science* 48(3): 183-194.

Mack RN, Bryant V, Fryxell R (1996) Pollen Sequence from the Columbia Basin, Washington: Reappraisal of Post-Glacial Vegetation. *American Midland Naturalist* 95(2): 390-397. DOI: 10.2307/2424402.

Manten AA (1967) Lennart Von Post and the Foundation of Modern Palynology, *Rev. Palaeobotan.Palynol.* 1(1-4): 11-22. https://doi.org/10.1016/0034-6667(67)90105-4.

Minckley T, Whitlock C (2000) Spatial Variation of Modern Pollen in Oregon and Southern Washington, USA. *Review of Paleobotany & Palynology* 112(1-3): 99-123. https://doi.org/10.1016/S0034-6667(00)00037-3.

Prentice IC (1985) Pollen Representation, Source Area, and Basin Size: Toward a Unified Theory of Pollen Analysis. *Quaternary Research* 23(1): 76-86. https://doi.org/10.1016/0033-5894(85)90073-0.

Recio M, Cabezudo B, Trigo MD, Toro FJ (1997) Accumulative Air Temperature as a Predicting Parameter for Daily Airborne Olive Pollen (*Olea Europaea* L.) during the Pre-Peak Period in Málaga (Western Mediterranean Area). *Grana* 36(1): 44-48. DOI= https://doi.org/10.1080/00173139709362589.

Siska PP, Bryant VJr, Jones JJ (2001) The Spatial Analysis of Modern Pollen Rain in Big Bend National Park. *Palynology* 25(1): 199-216. DOI: 10.1080/01916122.2001.9989560.

Siska PP, Hung I, Bryant VJr (2012) The Mapping of Composite Pollen from Point Sampled Data and Cartographic Generalization. *Papers of the Applied Geography Conferences* 35. https://core.ac.uk/display/46600822.

Siska P, Polacik S (2014) Influence of Environmental Parameters on Spatial Distribution of Pollen Grains in Columbia Basin. Proceedings of the 2014 International Conference on Power Systems, Energy, Environment. Interlaken, Switzerland: Energy, Environment and Structural Engineering Series 22.

Steiner A, Brooks SD, Deng C, Thornton DCO, Pendleton MW, Bryant V (2015) Pollen as Atmospheric Cloud Condensation Nuclei. *Geophysical Research Letters* 42(9): 3596-3602. DOI. 10. 1002/2015GL064060.

Tauber H (1967) Investigations of the Mode of Pollen Transfer in Forested Areas. *Rev. Palaeobotan. Palynol.* 3(1-4): 277-286. https://doi.org/10.1016/0034-6667(67) 90060-7.

Von Post L (1916) Om Skogstradpollen i Sydsvenska Torfmosselagerfoljder. *Geol. Foren. Stocklwlm Forh.* 38: 384-390.

Whitmore J, Gajewski K, Sawada M, Williams JW, Shuman B, Bartlein PJ, Minckley T, Viau AE, Webb III T, Shafer S, Anderson P, Brubaker L (2005) Modern Pollen Data from North America and Greenland for Multi-Scale Paleoenvironmental Applications. *Quaternary Science Reviews* 24(16-17): 1828-1848.

Zhao Y, Herzschuh U (2009) Modern Pollen Representation of Source Vegetation in the Qaidam Basin and Surrounding Mountains, North-Eastern Tibetan Plateau. *Veget Hist Archaeobot* 18(3): 245-260.

Human Activity Recognition Making Use of Long Short-Term Memory Techniques

By Richard Wainwright[*] & Alex Shenfield[†]

The optimisation and validation of a classifiers performance when applied to real world problems is not always effectively shown. In much of the literature describing the application of artificial neural network architectures to Human Activity Recognition (HAR) problems, postural transitions are grouped together and treated as a singular class. This paper proposes, investigates and validates the development of an optimised artificial neural network based on Long-Short Term Memory techniques (LSTM), with repeated cross validation used to validate the performance of the classifier. The results of the optimised LSTM classifier are comparable or better to that of previous research making use of the same dataset, achieving 95% accuracy under repeated 10-fold cross validation using grouped postural transitions. The work in this paper also achieves 94% accuracy under repeated 10-fold cross validation whilst treating each common postural transition as a separate class (and thus providing more context to each activity).

Keywords: *LSTM, Neural Networks, Postural, Recurrent Neural Network; Human Activities.*

Introduction

Human activity recognition (HAR) is an old concept. Similar to ubiquitous computing, a sensor is used to collect data from the user to try and assist a user with a given task. HAR has a vast number of applications, including in the military domain, medical facilities, fitness tracking and in regular daily life. Nike have produced running shoes that contain integrated motion sensors to provide feedback and running statistics for athletes (Johnson 2018).[1] Similarly, Apple's latest watch OS update contains automatic activity/fitness detection to alert a user on their watch that they are working out and should begin to track this information (Hardwick 2018).

It is apparent that HAR is becoming more common in all aspects of daily life and therefore, this topic has become very attractive to researchers. Ongoing work means that basic activities including sitting and walking can be monitored and tracked reliably with a high level of accuracy if the user wears a high number of sensors nodes - unfortunately, it is not realistic to wear a large number of sensors. The introduction and popularity of the smartphone has helped to push research in this field, as these devices are usually equipped with both Gyroscopes and accelerometers; with some high-end devices providing 3 axial velocities from the accelerometer. People carry these devices with them all the time, so it provides an

[*]Researcher, Sheffield Hallam University, Sheffield, UK.
[†]Senior Lecturer and Researcher, Sheffield Hallam University, Sheffield, UK.
[1]Johnson D (2018) *Smart Shoes: Tracking Fitness through your Feet*.

obvious non-intrusive way of monitoring activities. Moreover, these devices are generally carried all day, so data can be collected anywhere. This allows us to obtain realistic data from real life situations.

This paper outlines an effective approach of detecting human activities making use of Long-Short Term Memory techniques with the novel aspect of additionally classifying postural transitions. Results presented show that this novel classification method is extremely effective as it provides high accuracy detection with a small number of false positives. 10-Fold repeated cross validation is introduced to validate the results obtained from the model.

The rest of the paper is organised as follows: The next section provides a brief background to existing HAR techniques within the smartphone/smart watch industry and introduces Long-Short-Term Memory recurrent neural network techniques. Section "Human Activity Recognition on Given Dataset" outlines the model setup and describes what validation methods were used and how they were applied to the proposed model. Section "Results" then describes the major milestones of the research completed and some potential developments for further work.

Background and Previous Work

Machine Learning Methods / Related Works

Machine learning techniques have been used for automatic classification of HAR throughout the literature. These ML techniques have been supervised, semi-supervised and unsupervised with all different methods proposed. Standard models such as Frequentist and Bayesian models (for example, binary decision tree and threshold-based classifiers) have been implemented (Ermes et al. 2008, Coley et al. 2005). In addition, geometric models were introduced to detect HAR with papers describing K-Nearest Neighbours, Artificial Neural Networks and also Support Vector Machines (Maurer et al. 2006, Khan et al. 2010). Liu et al. (2016) made use of single frame images from Microsoft Kinects and RNN LSTM classifiers to correctly identify the activities in the images. The results obtained 95% peak accuracy when making gate modifications to the LSTM.

Currently, no obvious model or classifier is the most appropriate for HAR as all the different techniques have established performances that are comparable. In ML, the most effective classification method is generally application specific with additional considerations including computing power, energy consumption and memory requirements all are considered trade-offs for producing a reliable model.

Evaluation Metrics and Performance

The validation and evaluation of HAR classification algorithms is generally made by using statistical analysis methods and readily available datasets. Confusion matrices are widely used in the ML community as a quick way of evaluating a classification model. Confusion Matrices allow clear insight in to the

types of errors made by the systems (false positives and true negatives) and correctly predicted results. Furthermore, the matrix allows the extrapolation of additional information including model accuracy, precision and F1-score. Confusion matrices, overall confusion matrix accuracy, best loss and best accuracy per fold will described and compared in this paper, they can be reviewed in the results section.

Long Short-Term Memory

Hochreiter and Schmidhuber (1996) proposed Long Shot Term Memory (LSTM) Units in the mid-90s as an alternative method of recurrent neural networks in order to combat the vanishing gradient problem

Unlike other networks, LSTMs preserve and maintain the errors so that they can be easily backpropagated through layers, which also make LSTMs useful for time series problems as this error can also be backpropagated through time. Preserving the error allows the recurrent network to continue to learn and train the model over a vast number of time steps. This solution opens a channel that allows causes and effects to be linked therefore removing the error at the source.

Analog gates are used in LSTMS where information can be stored, written to or read from – similarly to data stored within a computer. This gated cell contains information outside the regular flow of the recurrent neural network (RNN). The use of anlaog gates are implemented with element wise multiplication by varying functions such as sigmoids which are always in the range of 0-1. The implementation of analog over digital functions means that they are easily differentiated, therefore, making them suitable for backpropagation.

Each gate acts on the information/signals once they receive them, information can be blocked or passed on based on its strength and import. These signals are also filtered with each gates weight. These weights behave similarly to normal NN input and hidden states as they are adjusted throughout the RNN learning process. The cells learn when to permit data to: enter, be deleted or leave through the iterative processes found from backpropagating the errors, adjusting the weights and making informed guesses.

Architecture of LSTMs

LSTMs networks are unlike other networks as they comprised of memory blocks that are called cells. Each cell has two different states which are transferred to the next cell, the cell state and also the hidden state. Three major mechanisms called gates are responsible for remembering things and manipulations to the memory. These gates are known as the Forget gate, Input gate and Output gate. Each of these gates is discussed below but the overall architecture is shown in Figure 1 (Staudemeyer and Omlin 2016).

Figure 1. *LSTM Architecture Overview*

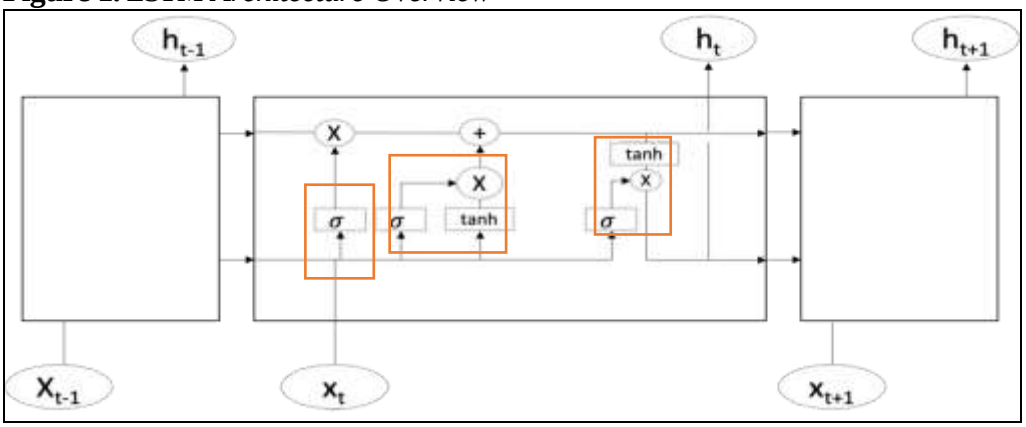

Forget Gate

A forget gate is designed for eradicating information from the current cell state. The LSTM performance is optimized by the removal of any unnecessary information that is no longer needed by the LSTM to understand things or to remove any information that isn't important anymore. The forget gate removes this information by the multiplication of a filter. A forget gate will take in two different inputs:

$$h_{t-1} \quad (1)$$

$$x_t \quad (2)$$

Equation (1) is the notation used to describe the hidden state from the previous cell whereas (2) is the input at that given time step. The two inputs are multiplied by the weight matrices at those times with an additional bias added. The resulting value then has a sigmoid function applied to it. Subsequently a vector with values from 0 to 1 is produced. The sigmoid function is responsible for telling the forget gate whether to discard or maintain the values. A resultant '0' means that the values will be forgotten along with the information it contains. Alternatively, a '1' means that the forget gate should retain that entire piece of information. The cell state and the vector output of the sigmoid are multiplied together.

Input Gate

The input gate is used to make sure that the all of information that is added to the cell stated is important and not redundant. The input gate can be described in a three-step process.

A) The first step of the process is similar to the forget gate as it filters information from (1) and (2). Values are regulated as to what values

should be added to the cell state by multiplying by another sigmoid function.

B) The results are then multiplied by a $\tan_h$ function which creates another output vector with values from -1 to +1.
C) Lastly, the values from the regulatory filter (A) and the values of the vector produced from $\tan_h$ (B) are multiplied together with any additional useful information from the cell state added on via an addition operation.

Output Gate

The selection of useful information from the current cell state and presenting it as an output is done with the output gate.

A) A vector is produced by apply the tan function again to the cell state. Therefore, producing another vector with values in the range of -1 to +1.
B) A filter that uses a sigmoid function and that makes use of values from both (1) and (2) is developed so that it can regulate the values from (A) is created.
C) The multiplication of steps (A) and (B) and using them as outputs is required for the final step. The information is also used as the hidden state in the next cell (Srivastava 2017).

Human Activity Recognition

HAR is a thriving research topic in deep learning. In order to design an effective HAR system each of the steps of data acquisition must be considered. The steps are defined as: data acquisition from the sensor, pre-processing the data, feature extraction and training/classification an overview of the HAR process is shown in Figure 2. The dataset used in this problem was captured by making use of an android smartphone attached to the user's body at which point they were asked to complete a list of 12 different human activities that make up each of our classes and is available at (Dua and Karra Taniskidou 2017). The performance of any HAR research will be affected by the techniques used at each of the activity recognition process steps. Moreover, in any monitoring system the performance will be greatly affected by the sensor used (Hassan et al. 2017).

Figure 2. *HAR Process Diagram*

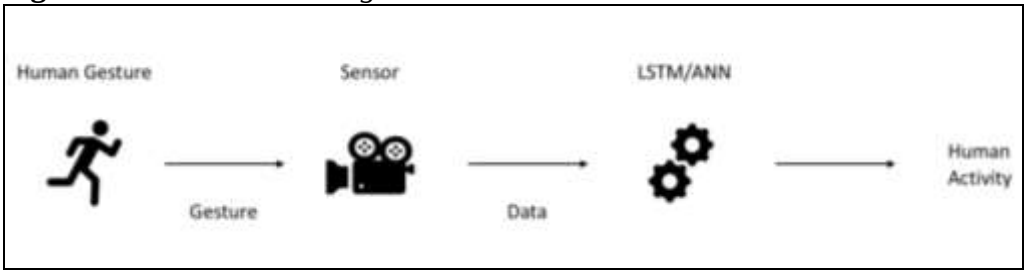

The experiments were carried out, using 30 volunteers with ages between 19 and 48. Each volunteer performed the twelve activities that included: walking, standing, sitting, walking upstairs, walking downstairs, laying, standing to sitting, sitting to standing, sitting to laying, laying to sitting, standing to laying and laying to standing whilst the smartphone was attached to their waist. The experiments were all recorded in order to make the process of labelling the activities easier. The chosen smartphone for the experiments was a Samsung Galaxy S2 smartphone as it contains both an accelerometer and a gyroscope that helps capture angular velocity and 3-axial linear acceleration at a constant 50Hz this sampling rate is high enough to accurately capture the change in movements during the human activity. The following sections describe the signal processing of the data and any filtering used on the raw signals. The resulting dataset was divided up in to two different sets 70% was described as the training data set for training the model whereas the remaining 30% was used as the test data in order to validate the trained model (Reyes-Ortiz et al. 2012).

Signal Processing

The incoming gyroscope and accelerometer was put through many stages of pre-processing before it was input in to the training model. Noise was reduced by making use of both a median and third order low pass Butterworth filter. The filter has a cut off frequency of 20Hz. The frequency threshold was selected as literature describes that the energy spectrum of the human body lies in the range between 0 Hz and 15 Hz. Following this pre-processing we obtained a triaxial acceleration signal that was clean. The clean signal can also be conveyed as the summation of two acceleration vectors which can be named as gravitational component G and BA which is the body motion acceleration. These signals were segmented making use of another low pass filter with an optimal cut off of 0.3 Hz (Reyes-Ortiz et al. 2014).

After segmentation, the signals were divided up using fixed-width sliding windows; each window has a span of 2.56s with a 50% overlap (Reyes-Ortiz et al. 2016).

Human Activity Recognition on Given Dataset

Problem Domain

Detecting human activities making use of gyroscope readings poses many challenges due to the inconsistency of the data, therefore introducing interclass variability in to the dataset. For example, the action of sitting to standing and then standing to sitting can be different in different environments and between different users. Moreover, human behaviour changes and multiple tasks can be completed simultaneously therefore making it harder to correctly recognise an activity.

The work presented in this paper offers an alternative to existing research completed on the dataset by using various methods of Deep learning and machine

learning techniques to create a reliable and robust model of human activity recognition.

LSTM Design

The data was divided up in to training and validation data in a 70:30 split. Preliminary visualisation of the data showed that there were different general trends and patterns for different activities although there was variability between gyroscope data of the same class.

The LSTM model for the experiments was developed making use of the Keras LSTM (Brownlee 2017) classifier with all of the code written in python. Repeated 10-fold cross validation was used in order to effectively evaluate the classifier. Figure 3 shows how cross validation is applied to a system over each iteration.

Keras

Francois Chollet (a Google engineer) developed and maintains Keras. Keras is a python library for deep learning capable of using multiple backends. It was developed in order to make it fast and easy to develop models and complete research on different techniques. It is designed to run on any version of python later than 2.7 however it is recommended to run on version 3.5. It can run on any GPU with only a small amount of set up required (Keras 2018).[2]

Tensorflow

A Tensorflow environment in order to make use of Kera's deep learning classifiers was used for this research. Tensorflow is a ML framework developed by Google. It is the second one they have developed, it is used to build, test and train different deep learning models. Tensorflow can be used to complete complex numerical computations making use of dataflow graphs (Tensorflow 2018).

K Fold Cross Validation

In k-fold cross-validation the original dataset is partitioned randomly into equal sizes, the number of these partitions is defined by the K variable. The data is then further divided so that a single K sample of the data is retained and kept unseen; this is used as the validation data for testing the model. The remaining K-1 subsets are used as the main training data. This cross-validation process can then be repeated K number of times (the folds) with each different K sub sets used once as the validation data. This has many advantages over other validation techniques as all of the observations are made making use of both the training and validation data at the same time. Furthermore, each validation set is used exactly once means

[2]*Keras: The Python Deep Learning Library*. [Online]. https://keras.io.

that the models are not just trained for the same test and train data sets. Figure 3 shows how the data for each fold is partitioned for each fold.

Stratified K-fold cross validation was introduced to try and combat datasets that are not evenly balanced between the different classes. Each fold is selected so that each fold contains a similar proportion of class labels.

Repeated cross-validation repeated the cross-validation n number of times. With n random portions of the original sample yielded. The n results are then averaged out in order to produce a singular estimation of the model (Brownlee 2018).

Figure 3. *Cross Validation Model*

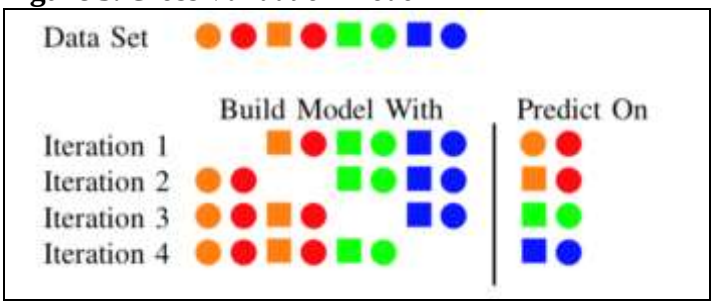

Results

Figure 4. *Histogram of Activities and Postural Transitions*

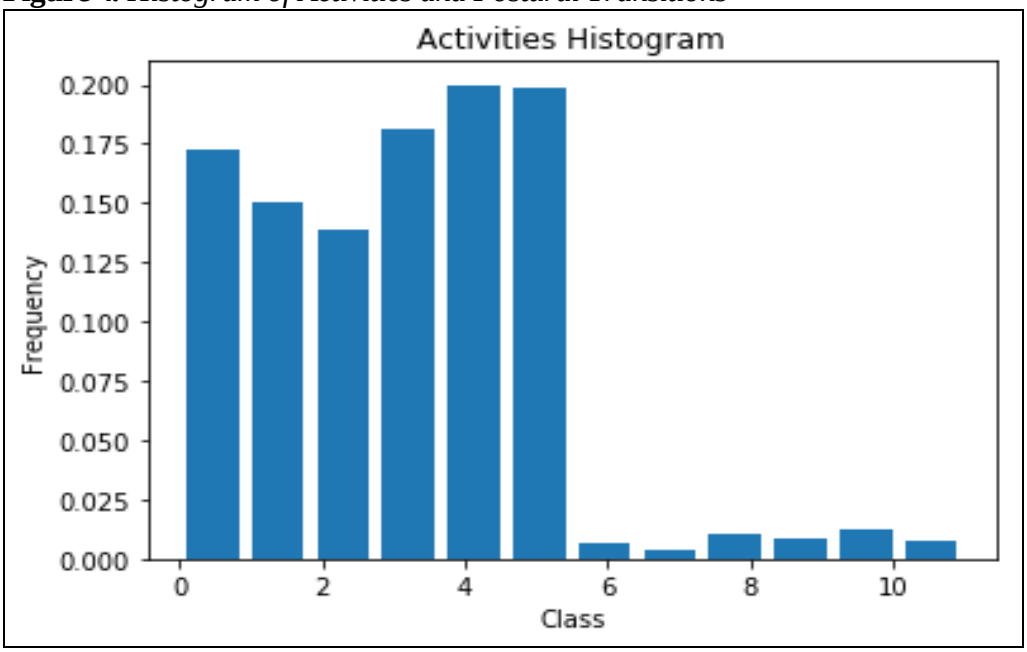

In this section, the LSTM framework presented in this paper is validated using the HAR dataset from (Reyes-Ortiz et al. 2016). Based on the amount of data and number of inputs and output classes, three different experiments are performed. The data used is the pre-processed train and test data with all of the data labels

given to the outputs. The three tests are designed to show the trade-offs between time taken to train the model and the number of neurons for each layer. Confusion matrices are used to analyse the results. A fourth test was introduced to combat the imbalanced data by grouping together all of the postural transitions. Figure 4 shows a histogram of the different classes, with classes 1-6 representing standard activities and classes 7-12 are the postural transitions. It can be clearly seen that the data set contains significant class imbalance towards the standard activities. Reyes-Ortiz et al. (2016) balance the data by grouping together all of the postural transitions; however, for the purposes of these experiments we will keep them apart.

Each experiment comprised of a consistent number of epochs with varying number of neurons, the details of which can be read in Table 1.

Table 1. *Number of Epochs and Neurons per Experiment*

	Number of Epochs	Number of Neurons	Number of Classes
Experiment 1	50	350	12
Experiment 2	50	100	12
Experiment 3	50	10	12

Each experiment was completed by using cross validation methods as described previously. Each test used ten-fold cross validation, with the best loss and accuracy per fold reported below. It is evident that the accuracy and the loss of the model improve as the number of neurons increases, with 350 LSTM neurons providing the best results. The accuracies presented represent the classification accuracies for each of the 12 different classes that were considered. It is important to note that these values will change for each iteration of the test as the NN does not always follow the same path. Tables 2 and 3 present the average performance for each test and the results from each fold. It can be seen that there is a clear trade-off between the time taken to train the model and the number of neurons used. As a direct result, it can be considered that continual training or online training of the model as outlined in Reyes-Ortiz et al. (2014) could be an acceptable way to improve the accuracy.

Table 2. *Best Accuracy and Best Loss per Fold in Each Different Test*

	Experiment 1		**Experiment 2**		**Experiment 3**	
Fold	**Accuracy**	**Loss**	**Accuracy**	**Loss**	**Accuracy**	**Loss**
1	0.94723	0.19128	0.91892	0.21641	0.82368	0.51748
2	0.93179	0.18562	0.90991	0.22369	0.75933	0.60864
3	0.92921	0.19149	0.90090	0.24912	0.77477	0.57704
4	0.94080	0.18151	0.91763	0.23443	0.72844	0.69128
5	0.95882	0.12116	0.93694	0.21028	0.75289	0.64023
6	0.92798	0.18684	0.93308	0.19595	0.75289	0.64865
7	0.94594	0.16575	0.91634	0.24413	0.79794	0.56883
8	0.91366	0.20554	0.90077	0.26693	0.75902	0.60082
9	0.94459	0.18222	0.90980	0.23877	0.81959	0.50970
10	0.94329	0.16544	0.89819	0.27480	0.80026	0.56522

Table 3. *The Average Best Loss and Accuracy*

Experiment 1	Average Best Accuracy	0.9383270973630582
	Average Best Loss	0.17768648393192576
Experiment 2	Average Best Accuracy	0.9142482320317372
	Average Best Loss	0.23466352699422233
Experiment 3	Average Best Accuracy	0.7768827370225013
	Average Best Loss	0.5927918261168678

Results presented in Reyes-Ortiz et al. (2013b) have shown that they can accurately determine HA with an overall 96% accuracy making use of SVM. These results are comparable to those obtained from the tests completed; however, they have introduced two alternative classes: a class of unknown – where the SVM cannot accurately predict the class - and a class where they have grouped together all of the postural transitions.

Confusion Matrix Experiment 1

Table 4. *Confusion Matrix without Normalisation for Experiment 1*

True Values		Walking	Walking Upstairs	Walking Downstairs	Sitting	Standing	Laying	Standing to sit	Sit to Stand	Sit to Lie	Lie to Sit	Stand to Lie	Lie to Stand
	Walking	**1211**	8	7	0	0	0	0	0	0	0	0	0
	Walking Upstairs	30	**1013**	25	0	1	0	3	0	1	0	0	0
	Walking Downstairs	16	30	**941**	0	0	0	0	0	0	0	0	0
	Sitting	1	0	1	**1150**	136	2	1	0	2	0	0	0
	Standing	0	1	0	116	**1305**	0	0	1	0	0	0	0
	Laying	0	0	0	0	0	**1407**	0	0	0	4	1	1
	Standing to sit	0	6	2	1	0	0	**31**	3	0	0	4	0
	Sit to Stand	1	0	0	1	0	0	3	**12**	3	1	2	0
	Sit to Lie	0	0	0	2	0	1	1	2	**42**	2	24	1
	Lie to Sit	0	0	0	0	0	2	0	0	2	**37**	4	15
	Stand to Lie	1	4	1	1	1	2	4	1	26	2	**46**	1
	Lie to Stand	0	0	0	0	0	3	0	0	5	25	1	**23**
		Predicted Values											

Confusion Matrix Experiment 2

Table 5. *Confusion Matrix without Normalisation for Experiment 2*

True Values		Predicted Values											
		Walking	Walking Upstairs	Walking Downstairs	Sitting	Standing	Laying	Standing to sit	Sit to Stand	Sit to Lie	Lie to Sit	Stand to Lie	Lie to Stand
	Walking	1195	21	10	0	0	0	0	0	0	0	0	0
	Walking Upstairs	61	959	45	0	2	0	5	0	0	0	1	0
	Walking Downstairs	27	45	914	0	0	0	0	0	0	0	1	0
	Sitting	0	0	1	1119	165	5	0	0	1	0	2	0
	Standing	2	5	0	121	1295	0	0	0	0	0	0	0
	Laying	0	0	0	0	0	1406	0	0	0	6	0	1
	Standing to sit	3	7	2	0	2	0	26	4	0	0	3	0
	Sit to Stand	1	1	0	1	0	0	5	7	5	0	3	0
	Sit to Lie	0	0	2	0	0	0	1	2	44	1	23	2
	Lie to Sit	0	0	0	1	0	5	0	0	4	26	5	19
	Stand to Lie	1	11	5	0	1	1	3	1	28	1	35	3
	Lie to Stand	0	0	0	1	0	2	0	0	1	21	4	28

Confusion Matrix Experiment 3

Table 6. *Confusion Matrix without Normalisation for Experiment 3*

True Values		Predicted Values											
		Walking	Walking Upstairs	Walking Downstairs	Sitting	Standing	Laying	Standing to sit	Sit to Stand	Sit to Lie	Lie to Sit	Stand to Lie	Lie to Stand
	Walking	737	283	206	0	0	0	0	0	0	0	0	0
	Walking Upstairs	157	780	118	2	12	0	0	0	2	0	2	0
	Walking Downstairs	212	109	666	0	0	0	0	0	0	0	0	0
	Sitting	3	1	0	1084	197	8	0	0	0	0	0	0
	Standing	8	10	0	137	1268	0	0	0	0	0	0	0
	Laying	0	0	0	0	0	1403	0	0	0	7	0	3
	Standing to sit	32	11	0	1	3	0	0	0	0	0	0	0
	Sit to Stand	12	2	0	1	1	1	0	0	6	0	0	0
	Sit to Lie	20	4	2	12	0	0	0	0	33	2	0	2
	Lie to Sit	0	1	0	2	0	17	0	0	7	14	0	19
	Stand to Lie	38	15	9	2	1	1	0	0	20	3	0	1
	Lie to Stand	0	0	0	1	0	16	0	0	8	15	0	17

Tables 4, 5 and 6 represent the confusion matrices of each the LSTM model for different experiment respectively. Because of the significant class imbalance (as shown in Figure 4) there is lots of confusion around the postural transitions. This is because there is not enough data to accurately train the model to identify these classes. In order to combat this and see if the results could be further improved, the postural activities were grouped together as done in Reyes-Ortiz et al. (2016) - giving only 7 classes in total.

Grouping Postural Transitions

Using the same parameters as the most accurate model (experiment 1, all of the postural transitions were grouped into a singular class. Therefore, seeing the effects of an LSTM model comparing it directly with those completed in literature under similar conditions. Table 7 shows the LSTM parameters used and the number of training epochs and number of classes.

Table 7. *Number of Epochs and Neurons for Grouped Experiment*

	Number of Epochs	Number of Neurons	Number of Classes
Experiment 4	50	350	7

The classification results on the HAR dataset when postural transitions are grouped together are shown in Table 8 and Table 9. They show an average best loss of 0.1430 and an average accuracy of 0.95% using 10-fold cross validation. This is comparable to the work completed by Reyes-Ortiz et al. (2013a).

Table 8. *Best Accuracy and Best Loss per Fold in during Group Postural Transition Training*

	Experiment 4	
Fold	**Accuracy**	**Loss**
1	0.94465	0.16102
2	096525	0.10930
3	0.94079	0.17676
4	0.95238	0.13211
5	0.96267	0.11365
6	0.93822	0.16284
7	0.94337	0.15059
8	0.94974	0.17733
9	0.95876	0.13726
10	0.95360	0.10990

Table 9. *Average Best Accuracy & Average Best Loss for Experiment 4 over the 10 Folds*

Experiment 4	Average Best Accuracy	0.9509475049500213
	Average Best Loss	0.14307998480867862

Comparing the confusion matrix for grouped postural transitions (Table 10) to those shown in Tables 4, 5, and 6 demonstrates that the grouping of postural transitions reduces the misclassifications shown in the confusion matrices. It is clear that the number of false positives and true positives has been greatly reduced.

The results obtained and detailed in Table 9 and Table 10 have been shown to outperform Karantonis et al. (2006) as their work which makes use of special purpose sensors has produced accuracies in the range of 90%-96%. Our work has shown accuracy in the range 93%-96%, and moreover it is more convenient to carry a smartphone that have bespoke sensors than sensors attached to different parts of the body. Similarly the work completed by Hanai et al. (2009) where a chest mounted accelerometer was used to record the HA has achieved an accuracy of 90.8% which is not as good as our results obtained using smartphone data. The argument for use of smartphones to for HAR is greatly increased as a direct result of these tests as on all occasions we have either outperformed or produced comparable results to those with bespoke sensors worn on the body.

Table 10. *Confusion Matrix without Normalisation for Experiment 4*

True Values		Predicted Values						
		Walking	Walking Upstairs	Walking Downstairs	Sitting	Standing	Laying	Postural Transitions
Walking		307	4	17	3	9	2	10
Walking Upstairs		1	1198	19	13	0	0	0
Walking Downstairs		3	23	1026	21	0	0	0
Sitting		1	10	19	957	0	0	0
Standing		5	0	0	0	1147	140	1
Laying		2	2	1	0	139	1279	0
Postural Transitions		3	0	0	0	0	0	1410

Device Utilisation

Table 11. *Device Utilisation Table*

Device	Utilisation
Epochs Used	350
Time Per Epoch (s)	14
Times Repeated Cross Validation:	10
NVIDIA INFORMATION	GeForce GTX1050

Conclusions & Further Work

Throughout this work an alternative and novel approach to reliably detect human activities making use of smartphones has been presented. The classification architectures presented in this paper make use of Long Short-Term Memory

techniques to classify both standard activities and postural transitions. The final model proposed considers the trade-offs of the time needed to train the model against the performance of the classifier. This paper then also compares the proposed model with existing literature.

The scope of the work is to apply existing technology to real world situations whilst still maintaining comparable results but improving processing times and use of the systems resources. The continual development of this research could then be applied to a wide range of industries including: the military, assisted living facilities and health & fitness tracking.

The results of the experiments confirm that is possible to make use of LSTM classifiers to correctly identify human activities, although further experimentation should be completed to evaluate the model with more representative conditions (such as a smartphone held by a user under real-world conditions throughout the day). These tests would allow further refinement of the model.

Acknowledgments

This study has been carried out with the help and support of the ACES and C3RI faculties within Sheffield Hallam University who have allowed the use of their equipment and space.

References

Brownlee J (2017) *How to Tune LSTM Hyperparameters with Keras for Time Series Forecasting.* [Online]. [Accessed 12/4/2017]. https://bit.ly/2LpXIH2.

Brownlee J (2018) *A Gentle Introduction to K-Fold Cross Validation.* [Online]. [Accessed 23/5/2018]. https://bit.ly/2BxuR0k.

Coley B, Najafi B, Aminian K (2005) Stair Climbing Detection during Daily Physical Activity using a Miniature Gyroscope. *Gait & Posture* 22(4): 287-294.

Dua D, Karra Taniskidou E (2017) *UCI Machine Learning Repository.* [Online]. http://archive.ics.uci.edu/ml/index.php.

Ermes M, Parkka J, Cluitmans M (2008) Advancing from Offline to Online Activity Recognition with Wearable Sensors. *IEEE Engineering in Medicine and Biology Society Conference* (Feb): 4451-4.

Hanai Y, Nishimura J, Kuroda T (2009) Haar-Like Filtering for Human Activity Recognition using 3D Accelerometer. *Digital Signal Processing Workshop and 5th IEEE Signal Processing Education Workshop.* DSP/SPE 2009. 13th IEEE.

Hardwick T (2018) *Apple Watch Owners can Compete in WatchOS 5, Auto-Detection of Workouts Coming Too.* [Online]. [Accessed 4/6/2018]. https://bit.ly/2UYw5JA.

Hassan M, Uddin M, Mohamed A, Almogren A (2017) A Robust Human Activity Recognition System using Smartphone Sensors and Deep Learning. *Future Generation Computer Systems* 81(Apr): 307-313.

Hochreiter S, Schmidhuber J (1996) LSTM can Solve Hard Long Time Lag Problems. *NIPS'96 Proceedings of the 9th International Conference on Neural Information Processing Systems.* Denver, Colorado: MIT Press Cambridge, 473-479.

Karantonis DM, Narayanan MR, Mathie M, et al. (2006) Implementation of a Real-Time Human Movement Classifier using a Triaxial Accelerometer for Ambulatory Monitoring. *IEEE Transactions on Information Technology in Biomedicine* 10(1).

Khan A, et al. (2010) Human Activity Recognition via an Accelerometer-Enabled Smartphone using Kernal Discriminant Analysis. *International Conference on Future Information Technology.*

Liu J, Shahroudy A, Xu D, Wang G (2016) Spatio-Temporal LSTM with Trust Gates for 3D Human Action Recognition. In *Computer Vision – ECCV 2016. Lecture Notes in Computer Science* 9907. Edited by Leibe B, Matas J, Sebe N, Welling M. Springer.

Maurer U, et al. (2006) Activity Recognition and Monitoring Multiple Sensors on Different Body Positions. *IEEE International Workshop on Wearable and Implantable Body Sensor Networks* 4.

Reyes-Ortiz J, et al. (2012) Human Activity Recognition on Smartphones using a Multiclass Hardware-Friendly Support Vector Machine. *4th International Workshop of Ambient Assisted Living* 216.

Reyes-Ortiz J, et al. (2013a) Energy Efficient Smartphone-Based Activity Recognition using Fixed-Point Arithmetic. *Journal of Universal Computer Science* 19(9).

Reyes-Ortiz J, et al. (2013b) A Public Domain Dataset for Human Activity Recognition Using Smartphones. In *ESANN.*

Reyes-Ortiz J, et al. (2014) Human Activity Recognition on Smartphones with Awareness of Basic Activities and Postural Transitions. In *ICANN.*

Reyes-Ortiz J, et al. (2016) Transition-Aware Human Activity Recognition using Smartphones. *Neurocomputing* 171(Jan): 754-767.

Srivastava P (2017) *Introduction to Long Short-Term Memory.* [Online]. [Accessed 10/12/2017]. https://www.analyticsvidhya.com/blog/2017/12/fundamentals-of-deep-learning-introduction-to-lstm/.

Staudemeyer R, Omlin C. (2016) Evaluating Performances of Long Short-Term Memory Recurrent Neural Network on Intrusion Detection Data. *SAICSIT '13 Proceedings of the South African Institute for Computer Scientists and Information Technologists Conference.* East London, South Africa.

Tensorflow (2018) *An Open Source Machine Learning Framework for Everyone.* [Online]. https://www.tensorflow.or.

EnergyPlus vs. Monthly ISO 13790 for Israeli Climatic Zones

By Samuel Hassid[*]

The energy efficiency, as predicted using on one hand the comprehensive building energy calculation program EnergyPlus and on the other hand the simplified monthly method of Standard ISO (EN) 13790, is compared for the four climatic zones of Israel. In two of those zones (Coastal and Negev Zones) cooling is dominant but heating is important; in another one, the Mountain Region, heating is dominant but cooling important and in the fourth one (Syrian-African Rift) there is essentially only cooling. The energy efficiency predicted by the two models is quantified as the percent reduction of annual heating plus cooling energy per unit area with respect to a pre-defined reference building. It is shown to be in fair agreement - with the simplified model being consistent with slightly better energy efficiency. The comparison is thought to be of relevance not only for the climates of Israel, but also for other climates in which cooling energy is as important as heating energy or more. The limitations of the comparison are discussed – especially the 24 hour heating/cooling assumption and the neglect of cooling latent heat in some regions.

Keywords: *Building Simulation, Cooling, Energy Efficiency, Energy Standards, Heating.*

Introduction

The effort to reduce energy consumption in most countries resulted in standards or regulations aiming at classifying buildings on the basis of their energy efficiency. These required ways of estimating the average energy consumption and performance of buildings. The differences between the predictions of the various software packages for estimating energy consumption of buildings are analyzed in numerous references (Crawley et al., 2005; Kokogiannakis et al., 2008; Kalema et al., 2008; Raslan and Davies, 2010, 2012; Summerfield et al., 2011; Schwarz and Raslan, 2013; Zhou et al., 2013).

In Israel the grading of the energy performance of buildings is required by the relatively new Energy Standards on Energy Performance of the Envelope of Buildings (Israel Standard 5280)[1] as well as the Standards on Green Buildings (Israel Standard 5281)[2] and Energy Rating of Buildings (Israel Standard 5282/1).[3] IS 5281 on Green Buildings is concerned with many issues including soil, water, materials, health and welfare, waste disposal, transport, site management and innovation, but energy is by far the most important one (but not the unique). To evaluate the energy performance – a standard for classifying different kinds of

[*]Associate Professor, Technion – Israel Institute of Technology, Israel.

[1]Israel Standard 5280, 2012 – Part 1.1. Energy in Buildings: Building envelope – Residential Buildings (2012). [In Hebrew].

[2]Israel Standard 5281, 2005. Buildings with Reduced Environmental Impact. ("Green Buildings"). [In Hebrew].

[3]Israel Standard 5282/1, 2011 Energy Rating of Buildings: Residential Buildings. [In Hebrew].

buildings was established, IS 5282, Standard for Energy Rating for Buildings, in which two options are considered, the Prescriptive one (not further considered in this work) and the Performance one.

Figure 1. *Schematic View of Reference Apartment for Energy Performance*

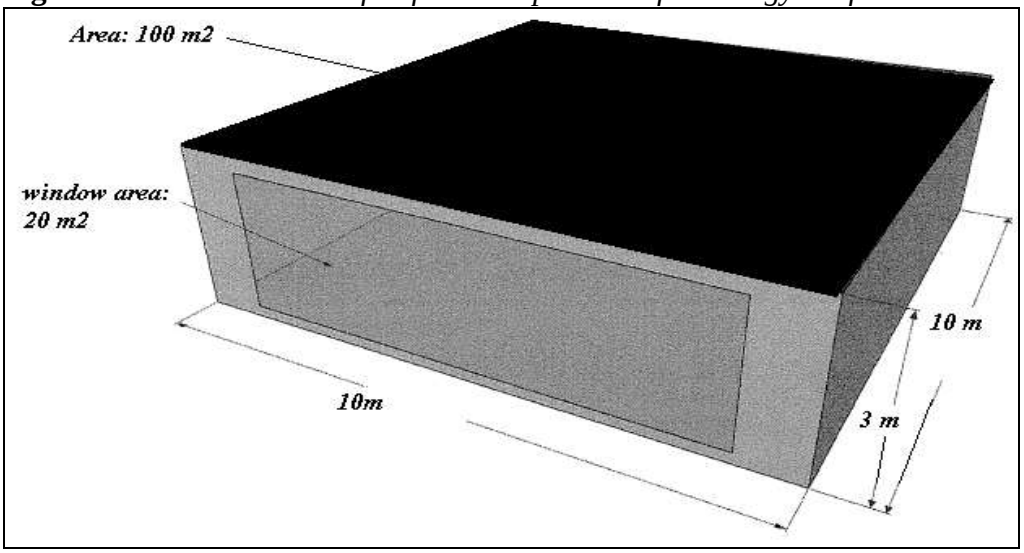

In the performance option - first the predicted, EP_{res}, the Annual Energy Consumption per square meter (sqm) of a (mediocre) reference building of 100 sqm is calculated (Figure 1). The properties of the envelope (consistent with the minimum requirements of Israeli Insulation Standard for Buildings 1045)[4] as well as predetermined schedules for lighting, equipment and shading of openings are specified for each climate zone in Israel Standard 5282. Subsequently the Annual Energy Consumption per sqm (*EP*) of the actual building under design is calculated, for the specified operation schedules. The percent reduction of the annual energy consumption of the building under design relatively to the reference building is used as a basis for classification (Table 1 – for the four climate regions of Israel, to be discussed later).

In addition to the Standard for Energy Grading of Buildings, a Standard for Energy Performance of the Building Envelope (IS 5280) has been established for several categories of buildings. It provides for three methodologies – prescriptive, semi-prescriptive and performance. For the performance methodology – a procedure similar to the one of the previously outlined IS 5282 is used – but in this standard there is a requirement for the maximum energy consumption per unit area:

1. For building unit area equal or above 70 sqm, the Annual Energy per Unit Area (*EP*) should not exceed $0.9 \times EP_{res}$ ($EP < 0.9\ EP_{res}$).

2. For building unit area below 70 sqm, the Annual Energy per Unit Area should not exceed $1.06 \times EP_{res}$ ($EP < 1.06\ EP_{res}$).

[4]Israel Standard 1045 Insulation of Buildings. [In Hebrew].

Table 1. *Classification vs. % Energy Reduction in Residential Buildings according to Israel Standard IS 5280*

Category	Region A	Region B	Region C	Region D
A+	**>35**	**>35**	**>40**	**>29**
A	**>30**	**>30**	**>34**	**>26**
B	**>25**	**>25**	**>27**	**>23**
C	**>20**	**>20**	**>20**	**>20**
D	**>10**	**>10**	**>10**	**>10**
E	**10>**	**10>**	**10>**	**10>**
F	**0>**	**0>**	**0>**	**0>**

To calculate EP_{res} and EP, as required by both IS 5280 and 5282, a model for energy calculation is needed. The standards mention that the calculation model should satisfy the requirements of EN 15265[5] for general criteria and validation of calculation methods of energy needs for space heating and cooling using dynamic methods. In IS 5280 ENERGY*ui*[6] is mentioned, a program based on EnergyPlus with a suitable front end developed in the Architecture Faculty of the Technion – Israel Institute of Technology, designed to test compliance with Israeli Energy Standards 5282 and 5280. This application has been received favorably by the community of architects in Israel.

Climatic Regions of Israel

Although Israel is a small country, it is characterized by several climatic zones very different from each other, reflecting its being located in the transition region from Mediterranean climate to Desert Sub-Tropical climate (Figure 2).

1. Mediterranean Coast (A - Aleph) with a Mediterranean climate
2. Internal Coastal Area and Negev climate (B - Bet)
3. Mountain climate (C - Gimel)
4. Sub-tropical climate along the African-Syrian rift valley (D - Dalet)

In Regions A and B the cooling period is dominant, in the Mountain Region (C) the heating period is dominant but the cooling energy is still appreciable and in Region D there is almost no heating. The exact boundaries of the above regions are not well defined. They were originally defined in the Israel Insulation Standard IS 1045 and modified subsequently. In the actual standard today there is a list of all towns and villages in Israel with the corresponding zone classification. The characteristics of those climate zones are summarized in Table 2A,B.

[5]EN 15265 Energy performance of buildings - Calculation of energy needs for space heating and cooling using dynamic methods - General criteria and validation procedures.
[6]ENERGY*ui*. Energyui.com. [In Hebrew].

Figure 2. *Climatic Zones in Israel (Approximately and for Insulation of Buildings Only)*

Table 2A. *Main Characteristics of Climate Zones in Israel (Long. 35E, Lat. 32N)*

Region		Koeppen climate class[7]	Heating Degree Days (18.3°C)	Monthly Av. Temp Jan., °C	Monthly Av. Temp Aug., °C
A	Tel-Aviv	Csa	550	12.1	25.5
B	Beer-Sheva	Csb	600	11.7	26.1
C	Jerusalem	Csb	1050	8	23
D	Eilat	Bwh	180	14.9	33

Source: Bitan and Rubin, 1991.

Table 2B. *Main Characteristics of Climate Zones in Israel (Long. 35E, Lat. 32N)*

Region		Koeppen climate class[8]	Relative Humidity Aug. 14:00, %	Average Daily Hor. Global Radiation, Wh/m^2	Average Daily Hor. Diffuse Radiation,Wh/m^2
A	Tel-Aviv	Csa	72	5130	1300
B	Beer-Sheva	Csb	67	5420	1780
C	Jerusalem	Csb	64	5370	1730
D	Eilat	Bwh	29	5560	1360

Source: Bitan and Rubin, 1991.

[7]http://www.weatheronline.co.uk/reports/climate/Israel-and-Palestine.htm.
[8]http://www.weatheronline.co.uk/reports/climate/Israel-and-Palestine.htm.

ISO 13790 on Simplified Ways of Estimating Sensible Heating and Cooling

Most European countries base their estimate of energy performance on European Norm/International Standard ISO/EN 13790.[9] The standard contains two simplified approaches – one "monthly/yearly" (the term "static" is often used, perhaps not appropriately since the thermal mass/thermal time constant is taken into account, albeit empirically) and one "hourly". We will focus on the first, which is the most common simplified model used for classification of residential buildings. The climates of Israel give an opportunity to test ISO 13790 in climates dominated by cooling rather than heating needs, contrary to what is the case in Northern European climates, at least for residential buildings. Note that the comparison between software packages in the works mentioned in the introduction (see References list) do not consider ISO 13790.

Simplified Monthly Model of ISO 13790

The methodology of the monthly method of ISO 13790 consists of the following steps:

1. Calculate L – the losses, in Wh, through the envelope by conduction and infiltration, based on the difference between the mean monthly temperature and the assumed set-point temperature.

$$L = 24M\left(\sum U_i A_i + \frac{\rho c_{pair} NV}{3600}\right)(T_{set} - T_o) \quad (1)$$

where A_i is the area of each element, U_i is the conductance of each element, N is the infiltration rate in air changes per hour, V the volume of the housing unit, T_{set} the internal set point temperature, T_o the outside average monthly temperature and M the number of days in the month.

2. Calculate the monthly solar loads S (through glazings) and internal heating loads I, in Wh.

$$S = M\sum G_i A_i \quad (2)$$

where G_i is the mean daily solar heat gain per unit area through window i.

3. Derive the gain to loss ratio $\gamma_H = (S+I)/L$ ratio for the months of the heating season and the loss to gain ratio $\gamma_C = L/(S+I)$ ratio for the months of the cooling one.

[9]ISO 13790 Energy Performance of Buildings - Calculation of Energy Use for Space Heating and Cooling.

4. For the heating season, the utilization factor η_H depends on γ_H. Once η_H is calculated, the monthly heating needs H can be calculated

$$\eta_H = \frac{1-\gamma_H^{\alpha}}{1-\gamma_H^{\alpha+1}} \tag{3}$$

$$H = L - \eta_H (S + I) \tag{4}$$

5. For the cooling season, the heat transfer processes are usually dominated by internal and solar energy gains. Thus the cooling utilization factor η_C depends on $\gamma_C = L/(S+I)$.

$$\eta_C = \frac{1-\gamma_C^{\alpha}}{1-\gamma_C^{\alpha+1}} \quad \text{for } L>0$$

$$\eta_C = 1 \quad \text{for } L<0 \tag{5}$$

$$C = (S + I) - \eta_C L \tag{6}$$

L is positive if the set-point temperature exceeds the average monthly temperature and negative in the opposite case. The exponent α in both the expressions for heating and cooling is a function of the total thermal time constant τ, i.e. the total thermal capacity of the building divided by the total loss coefficient.

$$\tau = \frac{\sum C_i A_i}{\sum U_i A_i + \rho_{air} c_{pair} NV / 3600} \tag{7}$$

where C_i is the thermal capacity per unit area of surface element i and the last term in the denominator is the loss coefficient due to infiltration/ventilation rate. The exponent α in Eqs. (3) and (5) is given by:

$$\alpha = 1 + \frac{\tau}{\tau_{ref}} \tag{8}$$

where the reference time constant τ_{ref} is 15h. Exponent α may vary from 1 for no thermal mass to approximately 7 for very high thermal mass. (In ISO/EN 13790 one is allowed to introduce national rules for exponent α).

Subject of the Investigation

The subject of this work is to calculate Heating, Cooling and Total Energy Needs for the Reference Home + an improved version of that Home (Improvement in insulation of walls and roofs, double glazing, infiltration reduced by 20%) using:

1. EnergyPlus (Version 7.0)[10]
2. ISO 13790 (monthly method)

This is done for several apartments:

1. Middle Floor
2. Upper Floor
3. Detached House above Raised Columns (Pilotis) (or Roof + Pilotis).
4. Detached House above Ground (or Roof + Ground Floor)

The calculations are repeated for the each of the four climate regions of Israel (A, B, C and D).

Calculations

The calculations are based on the reference building as defined in the Israeli Standards 5282 and 5280, in which the properties of the walls, the roof and the floor are defined, as well as the properties of the window and the amount of lighting and equipment internal load. The apartment is 10m×10m (100 sqm floor area) and 3m high with a 20 sqm single-glazing on one face – and the basis of comparison of other buildings is the average annual energy for the four apartments with windows facing South, North, East and West. Subsequently the improved building is chosen, with *U*-values of walls equal to 80% of the corresponding ones in the reference building and infiltration equal to 80% of the one of the reference building and the single glazing of the reference building is replaced by double glazing. Contrary to the stipulations of IS 5282, it is not possible to incorporate night cooling for the cooling season. This cooling strategy is not properly taken into account in the monthly method of ISO 13790 in hot countries. Therefore 24 hour heating to 20^{o}C during the heating period and 24 hour cooling to 24^{o}C during the cooling period is assumed. For consistency, a uniform 50% shading of the glazing is assumed, although in the actual standard there is some differentiation of the shading between seasons and climatic regions.

The climate data are based on the ones used in EnergyPlus (Bet-Dagan for Region A, Beer-Sheva for Region B, Jerusalem for Region C and Eilat for Region D) which can be downloaded from the EnergyPlus website. From these data the mean monthly temperature and the mean daily solar irradiation in different directions are calculated, to be used as simplified climate input for ISO 13790. The EnergyPlus version used is 7.0.0.

[10]EnergyPlus. http://apps1.eere.energy.gov/buildings/energyplus/. EnergyPlus Energy Simulation Software.

Results

In Figures 3 to 4 the total annual heating and cooling energy per unit area, as calculated using EnergyPlus and ISO 13790, are shown for some of the chosen configurations and the four climatic zones for Israel. Agreement between the predictions of the two calculation methods can be judged to be fairly good, even though in some cases especially in Regions A (and B) this is a result of the difference in the cooling energy cancelled by the corresponding one in the heating energy. Cooling energy is shown to be dominant in Regions A and B whereas heating energy is dominant in Region C and in Region D there is almost no heating.

Figure 3A. *Annual Heating + Cooling Energy per sqm for Middle Floor Apartment – Bet-Dagan (Region A)*

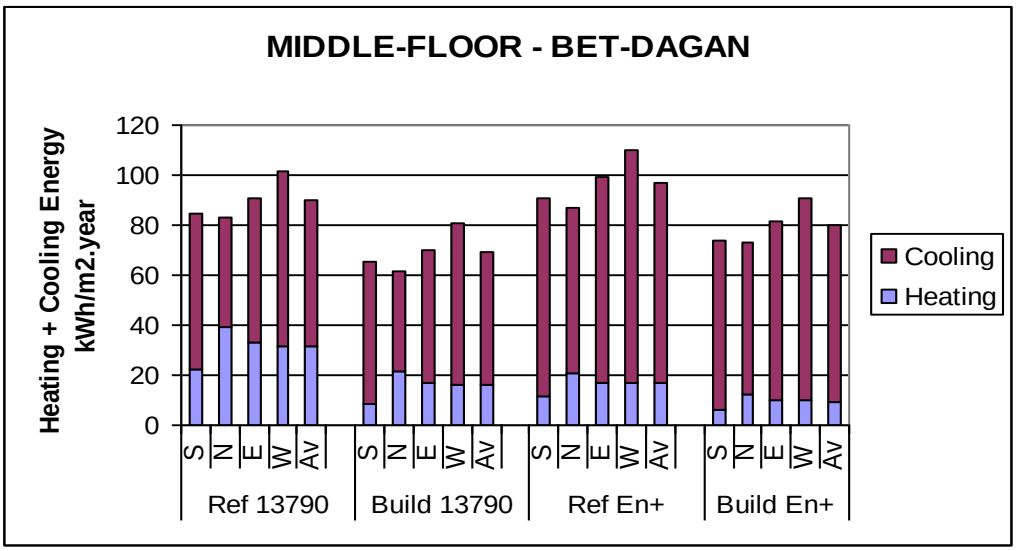

Figure 3B. *Annual Heating + Cooling Energy per sqm for Middle Floor Apartment – Jerusalem (Region C)*

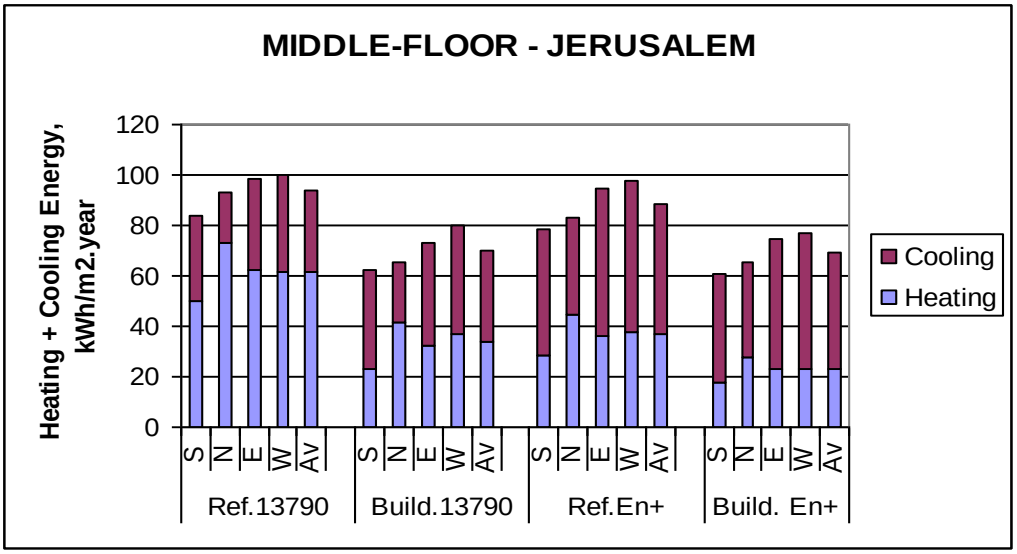

Figure 3C. *Annual Heating + Cooling Energy per sq.m. for Middle Floor Apartment – Eilat (Region D)*

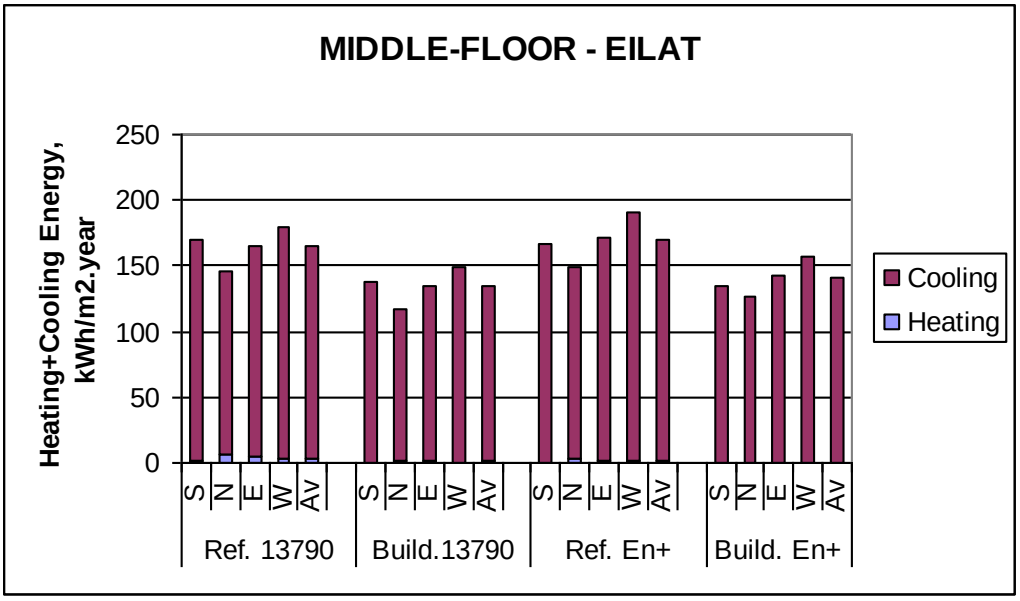

Figure 4A. *Annual Heating + Cooling Energy per sqm for Upper Floor Apartment – Bet-Dagan (Region A)*

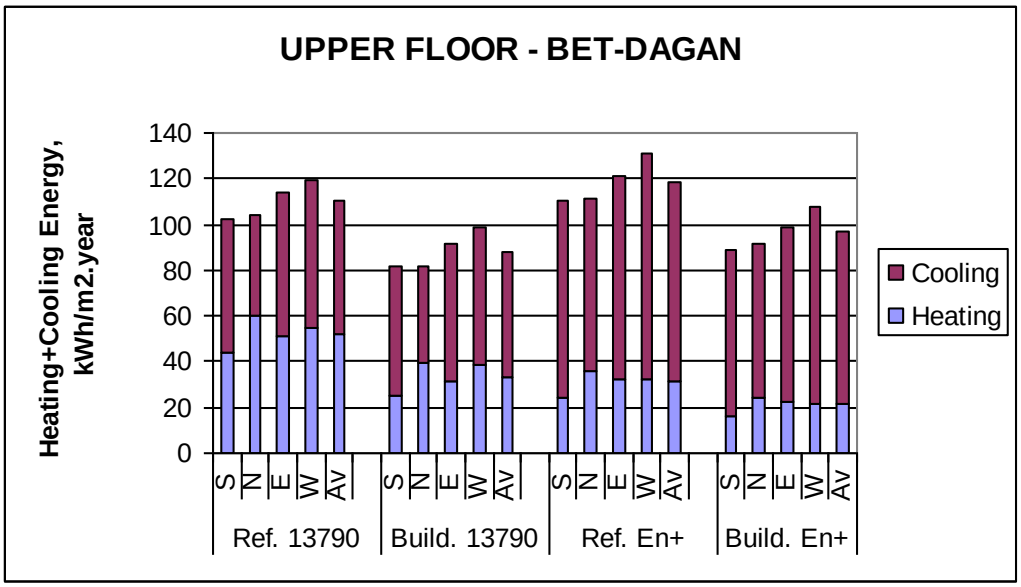

Figure 4B. *Annual Heating + Cooling Energy per sqm for Upper Floor Apartment – Jerusalem (Region C)*

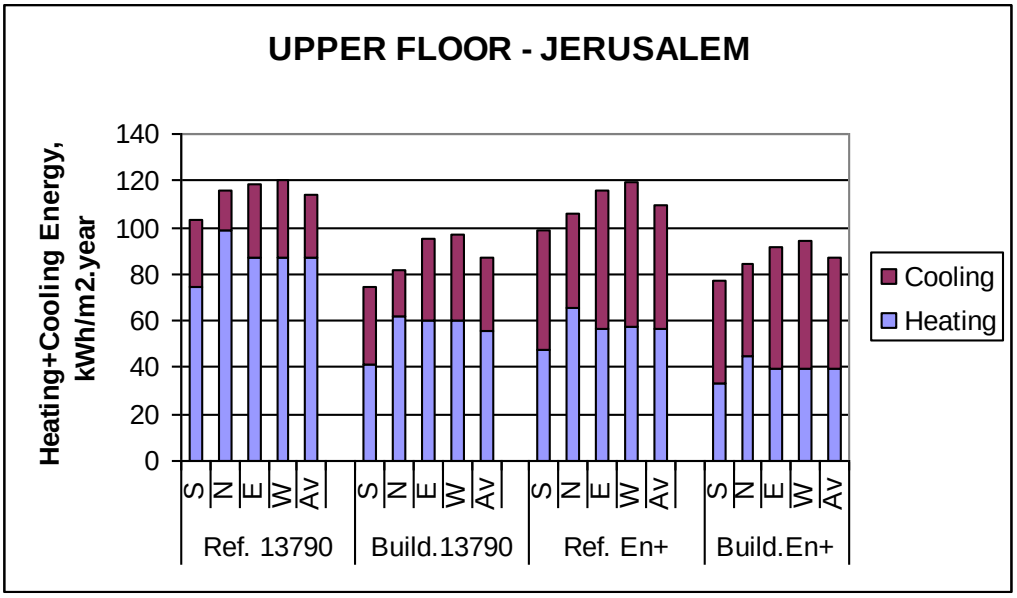

Figure 4C. *Annual Heating + Cooling Energy per sqm for Upper Floor Apartment – Eilat (Region D)*

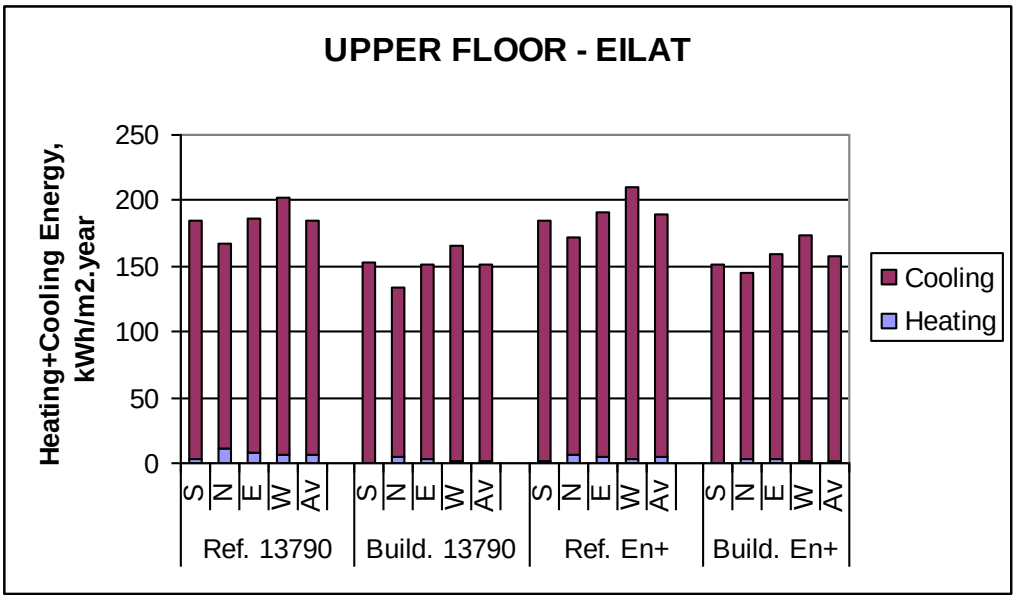

In Figures 5 to 8 the predicted reduction in annual energy needs of the improved building relative to the reference one is shown (Tables 3 to 6).

Table 3A. *Reduction of Cooling + Heating Energy + Category Bet-Dagan (Region A) Middle Floor*

Window orientation	Reduction % - ISO 13790	Reduction % - EnergyPlus	Energy category – ISO13790	Energy category – EnergyPlus
S	27.4	24.0	B	C+B
N	31.3	24.8	A	C+B
E	22.0	15.6	C	D
W	10.5	6.1	D-E	E
Average	22.8	17.6	C	D

Table 3B. *Reduction of Cooling + Heating Energy + Category Beer-Sheva (Region B) – Middle Floor*

Window orientation	Reduction % - ISO 13790	Reduction % - EnergyPlus	Energy category – ISO13790	Energy category – EnergyPlus
S	24.8	24.8	C+B	C+B
N	27.0	24.3	B	C+B
E	17.4	15.9	D	D
W	7.4	6.9	E	E
Average	19.1	18.0	D+C	D

Table 3C. *Reduction of Cooling + Heating Energy + Category Jerusalem (Region C) – Middle Floor*

Window orientation	Reduction % - ISO 13790	Reduction % - EnergyPlus	Energy category – ISO13790	Energy category – EnergyPlus
S	33.9	31.7	B+A	B
N	30.3	26.2	B	C+B
E	22.1	15.9	C	D
W	14.7	12.8	D	D
Average	25.3	21.7	C	C

Table 3D. *Reduction of Cooling + Heating Energy + Category Eilat (Region D) – Middle Floor*

Window orientation	Reduction % - ISO 13790	Reduction % - EnergyPlus	Energy category – ISO13790	Energy category – EnergyPlus
S	16.0	20.2	D	C-D
N	29.2	25.5	A+-A	A-B
E	18.2	16.1	D	D
W	9.3	7.1	E+D	E
Average	18.2	17.2	D	D

Table 4A. *Reduction of Cooling + Heating Energy + Category Bet-Dagan (Region A) – Upper Floor*

Window orientation	Reduction % - ISO 13790	Reduction % - EnergyPlus	Energy category – ISO13790	Energy category – EnergyPlus
S	25.7	25.1	B-C	B-C
N	25.9	22.7	B-C	C
E	17.1	16.6	D	D
W	9.9	9.4	E+D	E+D
Average	19.6	18.5	D+C	D

Table 4B. *Reduction of Cooling + Heating Energy + Category Beer-Sheva (Region B) – Upper Floor*

Window orientation	Reduction % - ISO 13790	Reduction % - EnergyPlus	Energy category – ISO13790	Energy category – EnergyPlus
S	22.5	25.4	C	B-C
N	24.4	22.3	C+B	C
E	18.1	16.5	D	D
W	10.9	9.5	D-E	E+D
Average	19.0	18.4	D	D

Table 4C. *Reduction of Cooling + Heating Energy + Category Jerusalem (Region C) – Upper Floor*

Window orientation	Reduction % - ISO 13790	Reduction % - EnergyPlus	Energy category – ISO13790	Energy category – EnergyPlus
S	34.6	29.9	A-B	B
N	28.3	23.2	B	C
E	16.9	16.6	D	D
W	15.2	14.0	D	D
Average	23.8	20.9	C	C-D

Table 4D. *Reduction of Cooling + Heating Energy + Category Eilat (Region B) – Upper Floor*

Window orientation	Reduction % - ISO 13790	Reduction % - EnergyPlus	Energy category – ISO13790	Energy category – EnergyPlus
S	17.4	20.7	D	C-D
N	27.9	23.6	A	B-C
E	18.5	16.0	D	D
W	11.0	8.6	D-E	E
Average	18.7	17.2	D	D

Table 5A. *Reduction of Cooling + Heating Energy + Category Bet-Dagan (Region A) – Roof + Pilotis Floor*

Window orientation	Reduction % - ISO 13790	Reduction % - EnergyPlus	Energy category – ISO13790	Energy category – EnergyPlus
S	25.6	18.0	B-C	D
N	23.8	14.7	C	D
E	19.3	10.0	D+C	E+D
W	12.8	3.9	D	E
Average	20.4	11.6	C-D	D

Table 5B. *Reduction of Cooling + Heating Energy + Category Beer-Sheva (Region B) – Roof + Pilotis Floor*

Window orientation	Reduction % - ISO 13790	Reduction % - EnergyPlus	Energy category – ISO13790	Energy category – EnergyPlus
S	25.5	18.2	B-C	C
N	22.9	14.6	C	C-D
E	18.4	10.0	D	D
W	12.7	4.1	D	D-E
Average	19.8	11.7	D+C	D

Table 5C. *Reduction of Cooling + Heating Energy + Category Jerusalem (Region C) – Roof + Pilotis Floor*

Window orientation	Reduction % - ISO 13790	Reduction % - EnergyPlus	Energy category – ISO13790	Energy category – EnergyPlus
S	35.9	28.8	A	B
N	28.5	21.6	B	C
E	26.8	17.4	C+B	D
W	25.7	15.2	C	D
Average	29.2	20.8	B	C-D

Table 5D. *Reduction of Cooling + Heating Energy + Category Eilat (Region D) – Roof + Pilotis Floor*

Window orientation	Reduction % - ISO 13790	Reduction % - EnergyPlus	Energy category – ISO13790	Energy category – EnergyPlus
S	19.0	20.8	D	C-D
N	26.0	21.8	B+A	C
E	18.5	15.8	D	D
W	12.6	9.7	D	E+D
Average	19.0	17.0	D+C	D

Table 6A. *Reduction of Cooling + Heating Energy + Category Bet-Dagan (Region A) – Roof + Ground Floor*

Window orientation	Reduction % - ISO 13790	Reduction % - EnergyPlus	Energy category – ISO13790	Energy category – EnergyPlus
S	26.7	25.5	B	B-C
N	26.8	22.9	B	C
E	20.2	18.3	C-D	D
W	12.4	11.6	D	D
Average	21.5	19.6	C	D+C

Table 6B. *Reduction of Cooling + Heating Energy + Category Beer-Sheva (Region B) – Roof + Ground Floor*

Window orientation	Reduction % - ISO 13790	Reduction % - EnergyPlus	Energy category – ISO13790	Energy category – EnergyPlus
S	27.2	26.2	B	B
N	23.8	22.9	C	C
E	19.3	18.3	D+C	D
W	11.2	11.6	D	D
Average	20.4	19.7	C-D	D+C

Table 6C. *Reduction of Cooling + Heating Energy + Category Jerusalem (Region C) – Roof + Ground Floor*

Window orientation	Reduction % - ISO 13790	Reduction % - EnergyPlus	Energy category – ISO13790	Energy category – EnergyPlus
S	33.6	28.7	B+A	B
N	24.8	21.0	C	C
E	24.0	17.7	C	D
W	23.0	15.5	C	D
Average	26.3	20.7	C+B	C-D

Table 6D. *Reduction of Cooling + Heating Energy + Category Eilat (Region D) – Roof + Ground Floor*

Window orientation	Reduction % - ISO 13790	Reduction % - EnergyPlus	Energy category – ISO13790	Energy category – EnergyPlus
S	18.2	15.2	D	D
N	26.2	16.2	A-B	D
E	18.3	9.7	D	E+D
W	12.1	3.2	D	E
Average	18.7	11.1	D	D

This is different from the actual calculations according to the Israeli Standard 5280 and 5282 where one takes into account the total annual electric energy consisting of heating, cooling plus lighting electric energy. In those standards the electric energy consumption of the air-conditioning devices for heating and

cooling is obtained by dividing the heating and cooling energy needs by a coefficient of performance (COP) of 3. Given that in Israel most electric air-conditioners are used for both heating and cooling, it is assumed in Standards 5282 and 5280 that both heating and cooling is done by electric air-conditioners with equal COP in summer and winter. In this work though, no assumptions are necessary for the value of COP and calculations of efficiency are based on heating plus cooling energy through the envelope of the building unit, with no consideration for the actual heating or cooling system. On the basis of energy needs reduction relatively to the reference unit and Table 1 the energy category is determined and shown in Figures 5 to 8 and Tables 3 to 6. In the marginal cases (less than 1% from the border value of energy percentage reduction between two categories), both categories are shown. For example, if the reduction is 19.5% then Category D+C is indicated, whereas for 20.5% the Category is C-D.

Figure 5A. *Reduction of Heating + Cooling Energy for Middle Floor Apartment – Bet-Dagan (Region A). Categories shown above*

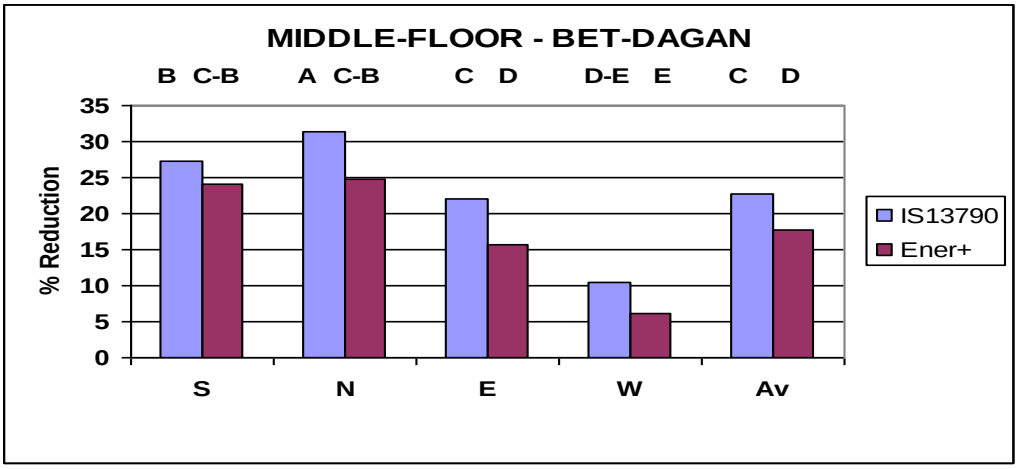

Figure 5B. *Reduction of Heating + Cooling Energy for Middle Floor Apartment – Beer-Sheva (Region B)*

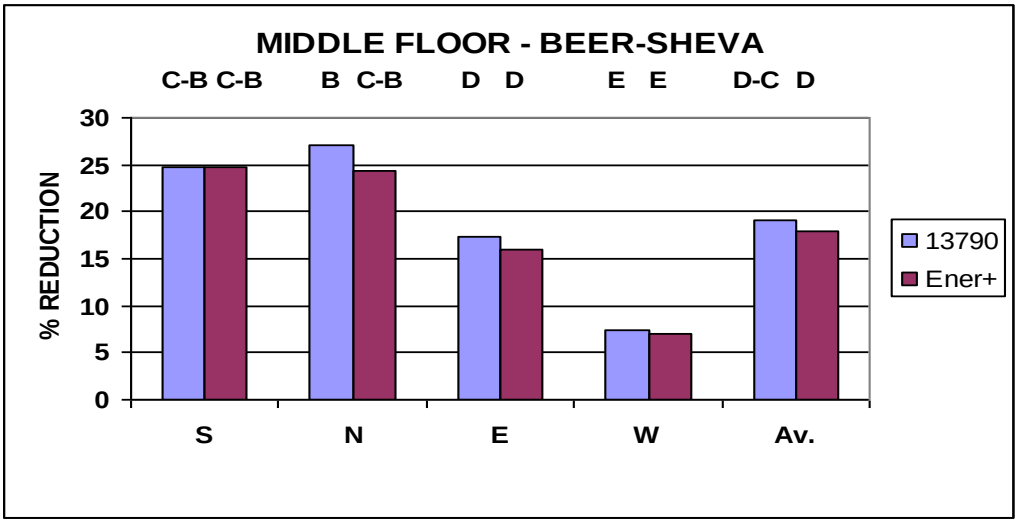

Figure 5C. *Reduction of Heating + Cooling Energy for Middle Floor Apartment – Jerusalem (Region C)*

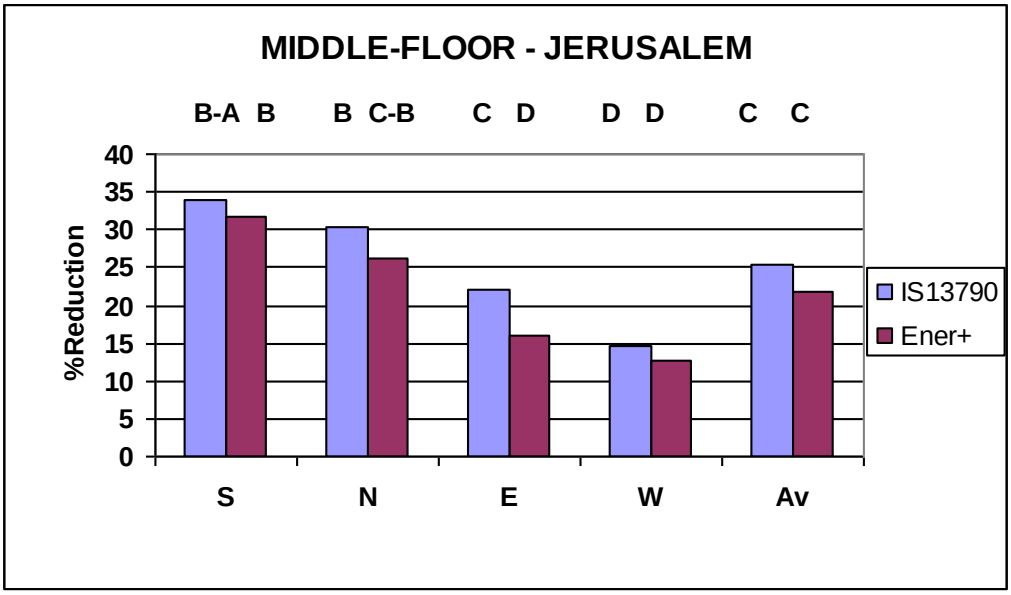

Figure 5D. *Reduction of Heating + Cooling Energy for Middle Floor Apartment – Eilat (Region D)*

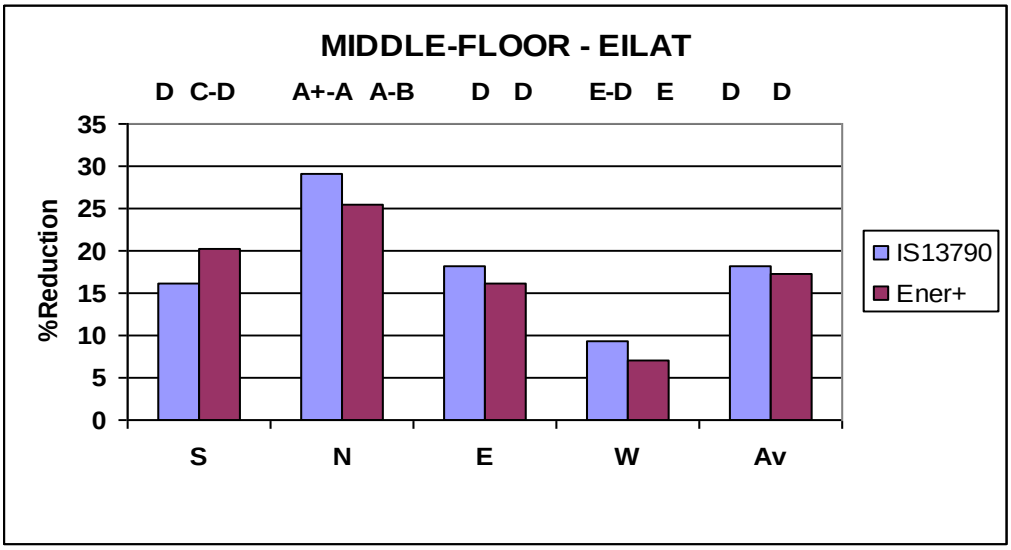

The reduction of the heating plus cooling energy as calculated by the two methods show an average difference of 3.4%. This an average of 4.2%, 2.6%, 5.1% and 3% for Climatic Zones A, B, C and D respectively or 2.7%, 1.5%, 6.5% and 4% for Middle Floor, Upper Floor, Upper Floor + Pilotis and Ground Floor respectively. This corresponds approximately to half a Category average (with borderline cases ±1% from the limit between two categories) considered as half-way between the two neighboring categories). The calculations using ISO 13790 are generally slightly more "optimistic" than the ones of EnergyPlus (that by their nature are considered more reliable), i.e. the reduction of annual energy needs

relative to the reference building is higher for the ISO 13790 monthly method calculations. This however does not necessarily mean that the actual total energy needs are smaller. The largest differences are encountered in the case of the Pilotis apartments – to some extent due to the difference in the algorithm used for calculating losses/gains through the elevated floor. In general, differences between the detailed EnergyPlus model and the very simplified monthly method of ISO 13790 are expected, since concentrating the temperature information for a month into one single monthly mean temperature is bound to lead to discrepancies and errors. This is particularly so when the month consists of different days with temperatures both above and below the set-point, as in Regions A and B – especially during the transition seasons.

Figure 6A. *Reduction of Heating + Cooling Energy for Upper Floor Apartment – Bet-Dagan (Region A)*

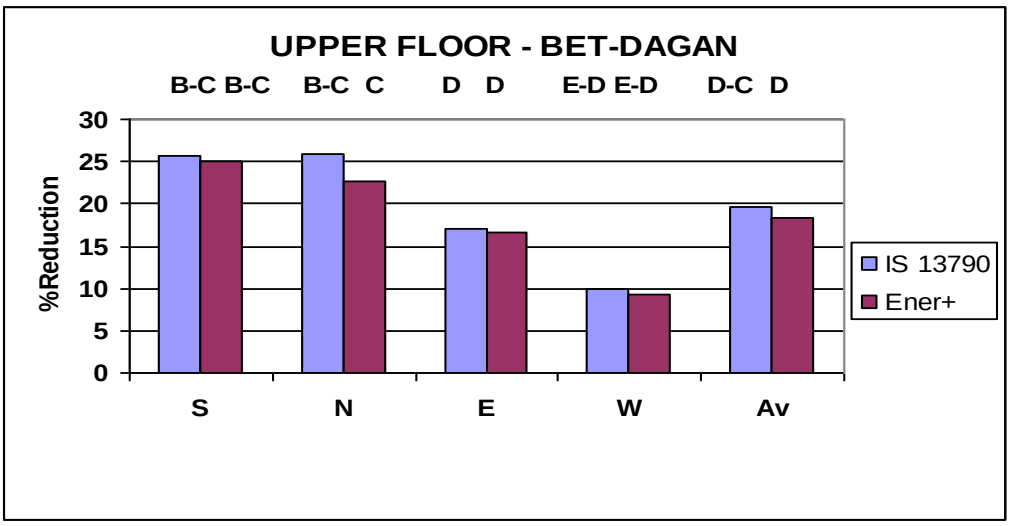

Figure 6B. *Reduction of Heating + Cooling Energy for Upper Floor Apartment – Beer-Sheva (Region B)*

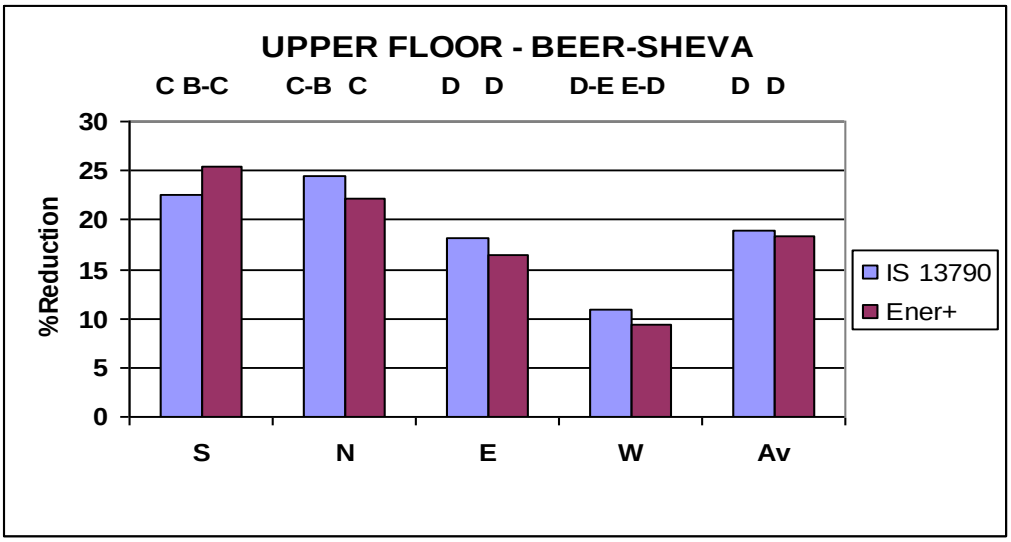

Figure 6C. *Reduction of Heating + Cooling Energy for Upper Floor Apartment – Jerusalem (Region C)*

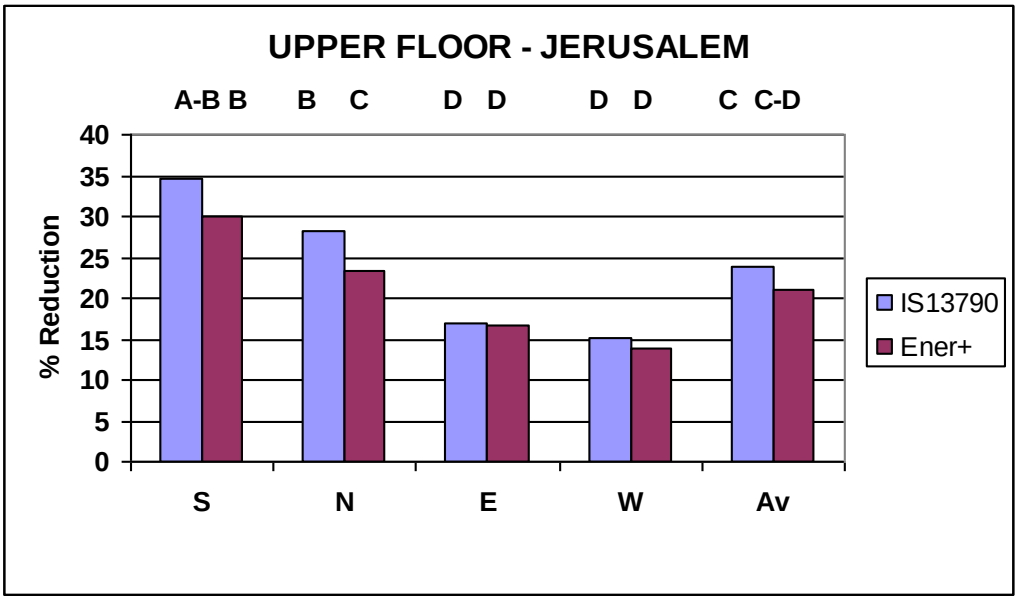

Figure 6D. *Reduction of Heating + Cooling Energy for Upper Floor Apartment – Eilat (Region D)*

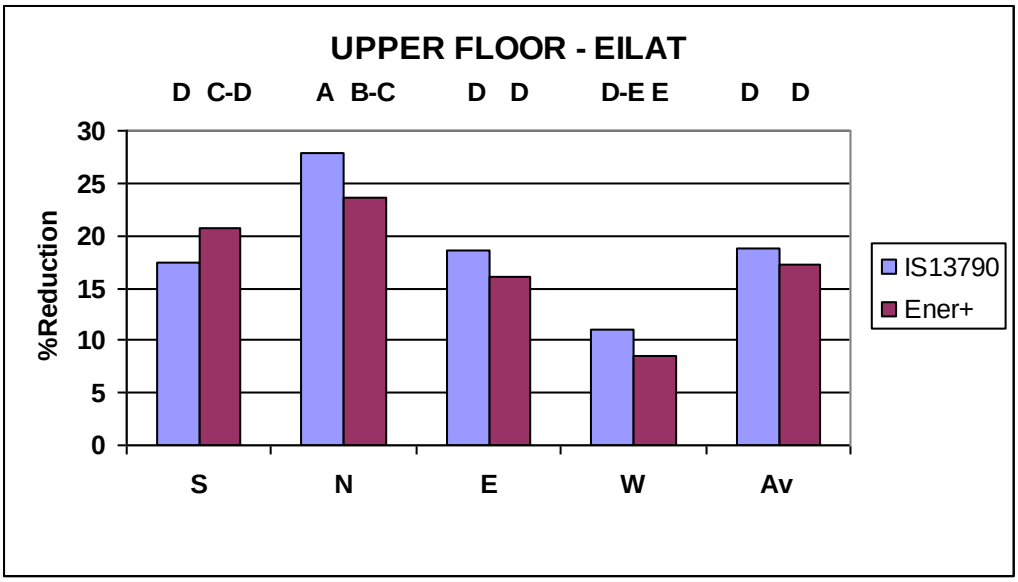

Figure 7A. *Reduction of Heating + Cooling Energy for Roof + Pilotis Floor Apartment – Bet-Dagan (Region A)*

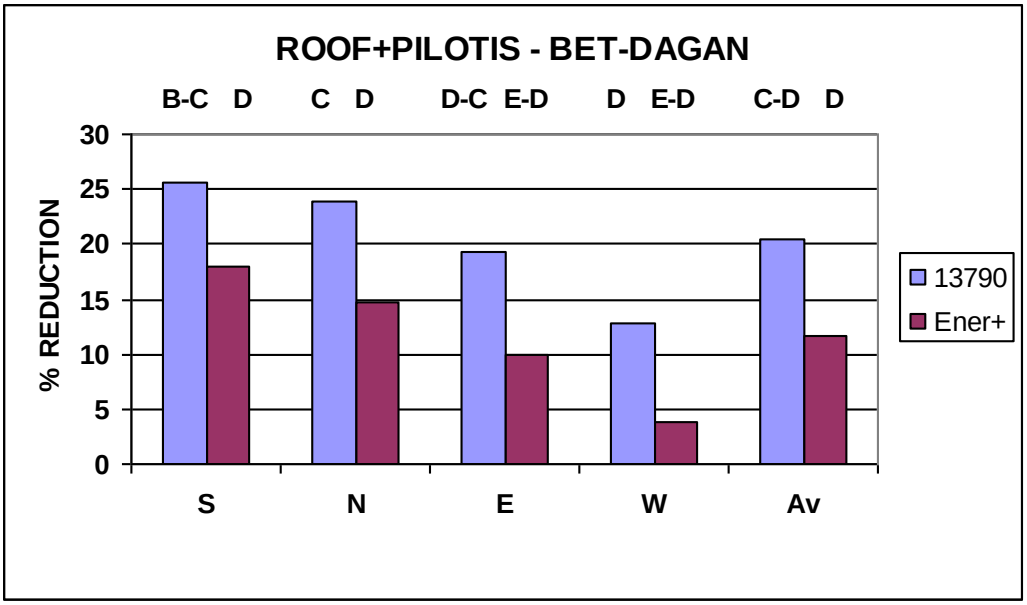

Figure 7B. *Reduction of Heating + Cooling Energy for Roof+Pilotis Floor Apartment – Beer-Sheva (Region B)*

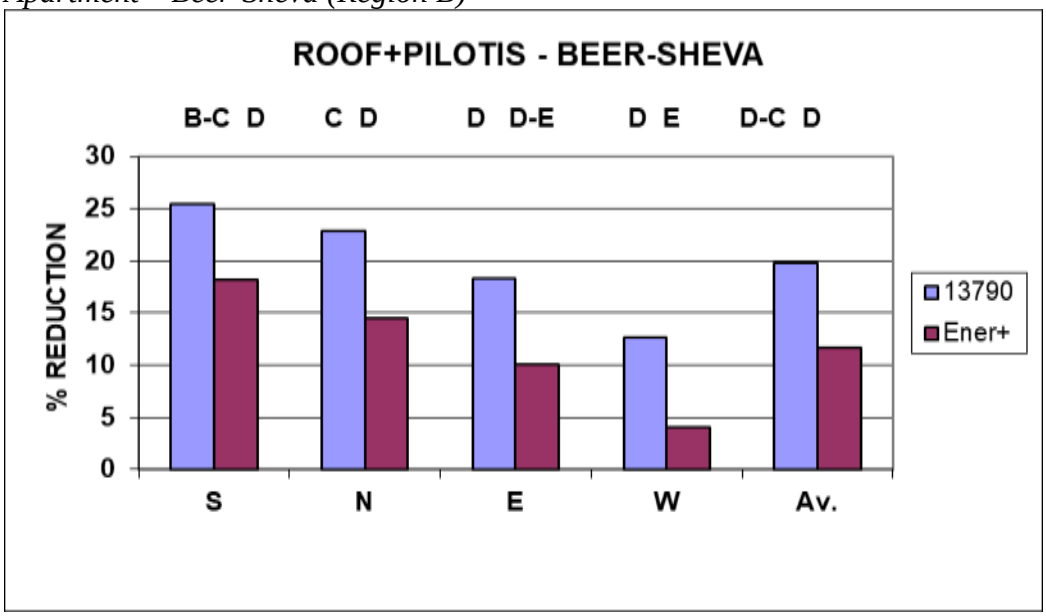

Figure 7C. *Reduction of Heating + Cooling Energy for Roof + Pilotis Floor Apartment – Jerusalem (Region C)*

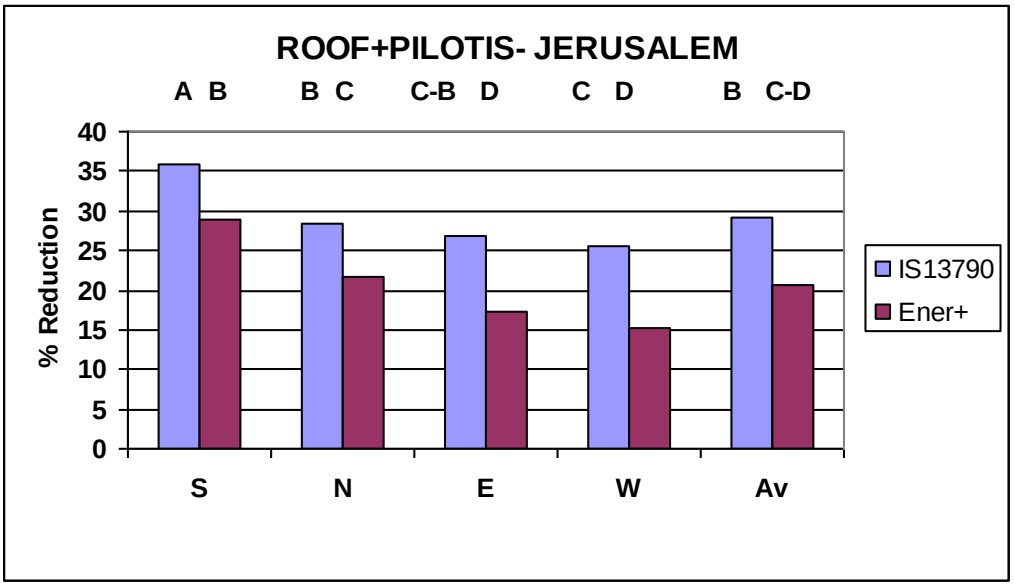

Figure 7D. *Reduction of Heating + Cooling Energy for Roof + Pilotis Floor Apartment – Eilat (Region D)*

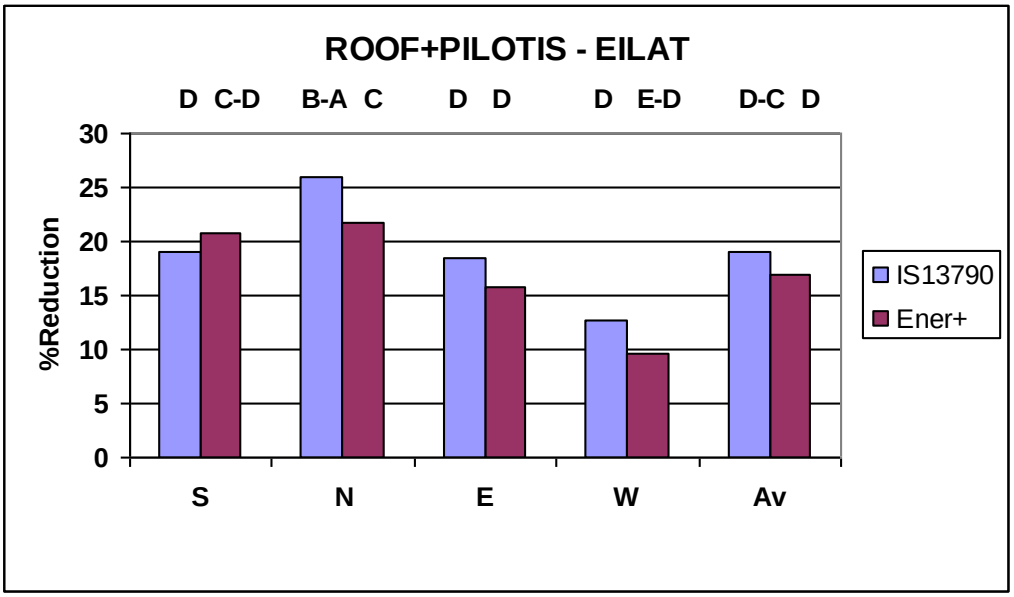

Figure 8A. *Reduction of Heating + Cooling Energy for Roof + Ground Floor Apartment – Bet-Dagan (Region A)*

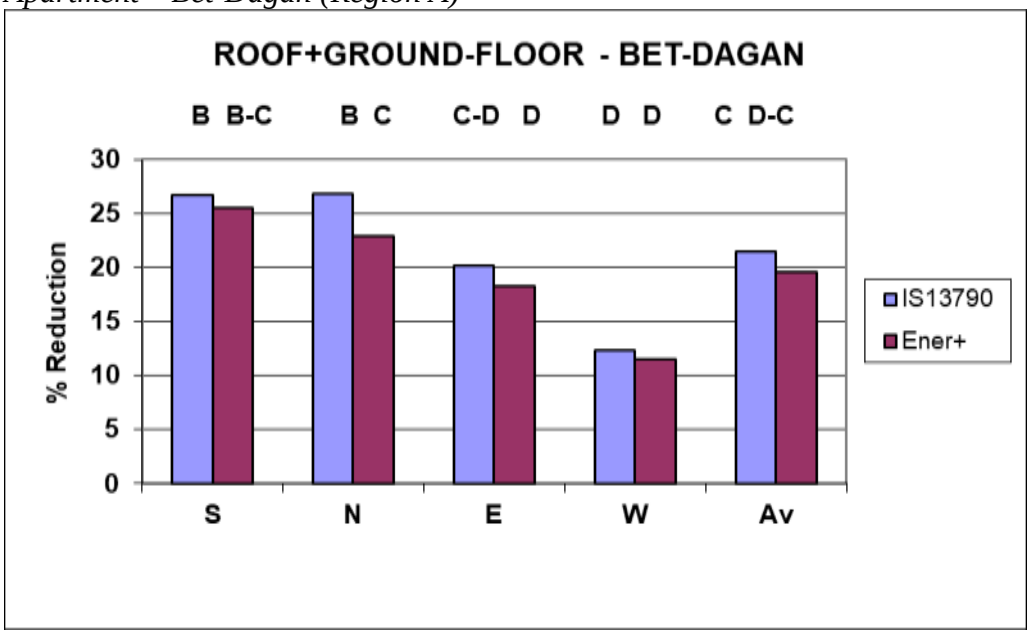

Figure 8C. *Reduction of Heating + Cooling Energy for Roof + Ground Floor Apartment – Jerusalem (Region C)*

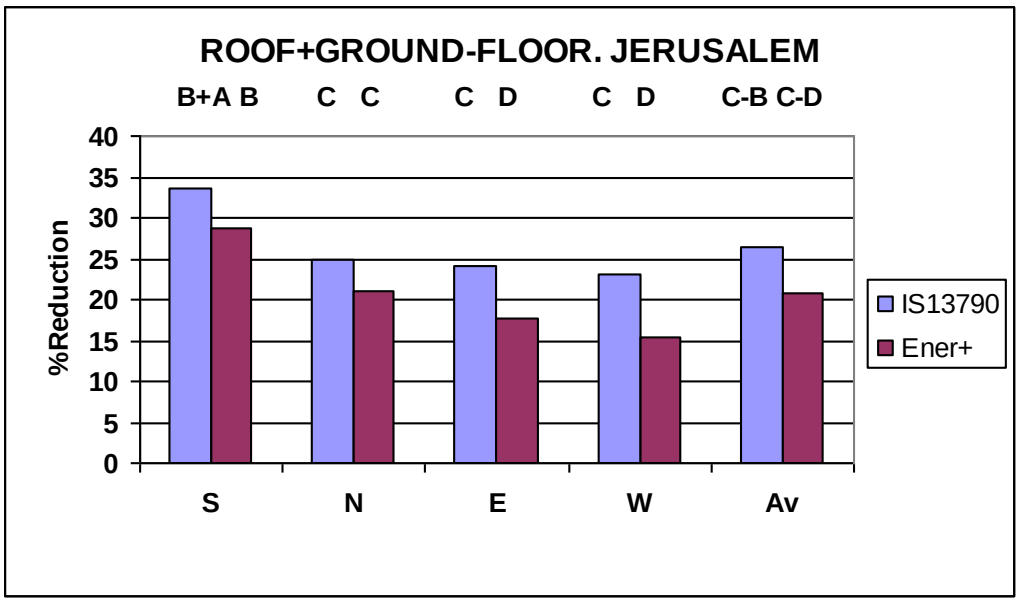

Figure 8D. *Reduction of Heating + Cooling Energy for Roof + Ground Floor Apartment – Eilat (Region D)*

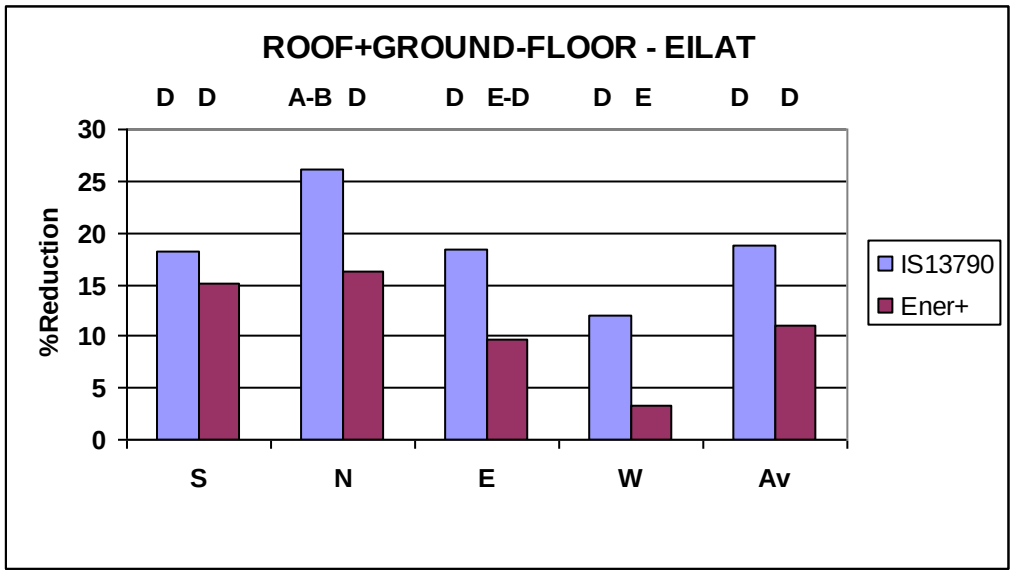

Discussion

The reduction of annual heating plus cooling energy per unit area as predicted by the ISO 13790, the most widely used simplified model, is compared to the one predicted by EnergyPlus, the most widely used comprehensive model, and shown to be in fair agreement for the four characteristic climatic zones in Israel. Of course, the comparison is not exhaustive and has many limitations.

The improved building is very similar in shape to the reference one – except for improved envelope properties and reduced infiltration. The choice of the reference apartment/building is itself problematic, given that apartments of different wall to area ratio and glazing to wall ratio have a different total energy per unit area.

For climatic zones A and B, where cooling dominates but heating is still substantial, this somehow hides bigger differences if one compares heating and cooling separately. The general agreement is slightly worse for heating-dominated Region C. Agreement is slightly better in exclusively-cooling region D, where for most of the year the effect of energy gains through the envelope and solar and internal gains is additive and the cooling energy efficiency factor η_C for the months accounting for most of the cooling energy is independent of the losses-to-internal-and-solar-gains ratio and equal to 1. Based on predicted reduction of heating and cooling energy for the improved building, it is shown that the predictions of ISO 13790 are slightly optimistic (i.e. predict a bigger reduction relative to the chosen reference building).

There are many reasons that differences appear between the two methods, the monthly one of 13790 and EnergyPlus, which is far more reliable from the point of view of heat transfer processes, even though many simplifications are involved

in it too. The theoretical basis of EnergyPlus is obviously much better, but ISO 13790 has the advantage that it is much more transparent whereas EnergyPlus to many frustrated constructers is considered an obscure black box. In Israel one can expect differences in the spring and the autumn, in which the weather is characterized by successions of cool and hot days and the mean monthly temperature as in ISO 13790 is insufficient to describe it. The contribution of these periods to annual energy needs however is relatively small.

As in all standards, the arbitrarily defined Categories may be problematic – especially in the vicinity of borderlines between them. This is why it was chosen to show, for cases close to the borderline (less than 1%), the alternative category, although this is not stipulated in the standards. Categories also become particularly problematic when the difference between the lower and the upper limit is only 3%, less than the mean estimated difference between the two models examined here. In such circumstances it is possible for the two models to predict a difference of two categories – unacceptable when it comes to characterizing buildings.

The comparison is done for Israel climates only under idealized conditions, since the geometry of the compared buildings (the reference and the improved one) is the same. In an attempt to estimate the effect of wall-to-floor-area ratio, the effect of that ratio on total energy consumption (relative to the reference building) was calculated for different values of that ratio – both larger and smaller than the one relevant for the reference building, with the window area and the properties of the envelope are being kept constant. The difference between the predictions of EN 13790 and EnergyPlus is shown to vary between 0 and 10%, depending on the climate, for the middle floor apartment. The effect of the wall-to-floor-area on the other kinds of buildings can be shown to be smaller, since there are conductive losses through the horizontal envelope elements, not affected by the differences of wall-to-floor-area ratio.

A sensitivity analysis of the results points that the relative energy reduction per unit area is more sensitive by 5 to 15% to changes in different parameters when calculated using ISO 13790 than with Energy Plus, for middle apartments. To estimate the effect of the wall-to-floor area, a sensitivity analysis of the reference building allowed for two alternative middle floor buildings – a 15x10 m building and a 10x7.5m building – the first one for a wall-to-surface ratio of 1 m/m^2 and 1.4 m/m^2 respectively, compared to the 1.2 m/m^2 of the reference building. The window-to-floor area ratio is kept constant throughout and so is the internal loads per-unit area ratio. The predicted relative energy change in the case of the ISO 13790 was approximately 20% higher than the corresponding one of EnergyPlus for the three regions in which cooling is dominant but approximately 35% for Jerusalem. Similar results were found for changing the infiltration rate. The predicted ratio of the relative energy increase resulting from increasing the window was found to be 40% higher for ISO 13790 when compared to EnergyPlus. In general – the relative energy reduction/increase predicted by ISO 13790 is larger than the corresponding one by EnergyPlus.

The main problem though for cooling-dominated regions (not the cooling-only Eilat (D) region though, where the night outside air temperature is above the set point temperature required) - is that cooling by night ventilation is not taken

into account as is the case of the requirements of Israeli Standard 5282. This may change the resulting classification radically in many cases. ISO 13790 proposes a monthly method that takes night ventilation into account, but is rather inappropriate for the Israeli conditions when there is a conductive and convective gain (as opposed to a loss) through the envelope. This is very important especially for zones A and B – since this way the importance of the cooling energy is increased and made dominant. Night cooling cannot be taken into account without differentiating between average night and day temperature. The monthly ISO 13790 calculation does provide for an approximate way to account for lack of cooling and increased air-flow rate during a part of the day, but it is still based on the average outside air temperature only and cannot properly take into account the difference between the day and the night temperature. This can only be accomplished by modifying the ISO 13790 monthly procedure so that the difference between the day and the night average temperature is somehow taken into account, as well as the storage of cooling energy in the building during the night. Note also that for the chosen all-day-cooling (and all-day-heating) pattern the internal thermal mass has a much smaller influence than it does in the case of partially heated and partially cooled buildings.

Another important problem for some cooling-dominated regions – not Region D where humidity is low – is accounting for latent heat. This may be particularly important in the Mediterranean Coastal Region A where it can account for up to 30% of actual cooling energy. This can be done with EnergyPlus, but ISO 13790 is not concerned with calculating latent heat. It can be modified appropriately by adding to the sensible heat either the latent heat involved in reducing the humidity ratio to the one of the dew point at the set-point temperature – or to a relative humidity at the set-point temperature of, say, 50%. Of course, the actual reduction in the humidity ratio depends on the cooling system and equipment, which cannot be properly modelled by a monthly method. A standard for latent heat approximate estimation is currently elaborated (Standard EN ISO 52016-1)[11].

The appropriateness of a 24h cooled and heated building can also be questioned, since most buildings in Israel, especially in Regions A, B and C which account for the vast majority of the population, are not operated in this mode. The reasoning behind it is to estimate the maximum energy savings potential of the building, but when later in a post-occupancy evaluation study one compares the calculation procedure with actual results, one can expect substantial differences. The shading (and ventilation) strategies which are central for energy conservation during cooling periods cannot be properly taken into account using the monthly ISO 13790, even in the simplified way that they are required by IS 5280.

[11] EN ISO 52016-1 Energy performance of buildings — Calculation of the energy needs for heating and cooling, internal temperatures and heating and cooling load in a building or building zone — Part 1: Calculation procedures (in preparation).

Conclusions

It is attempted to address the problem whether monthly ISO 13790 – the most well-established simplified energy model and the basis of energy classification of buildings in most countries of the EU – is appropriate for Israel, but also, indirectly, for many countries with similar climate where the cooling period is the dominating one. It can be concluded that the monthly ISO 13790 can serve as an alternative to EnergyPlus, the most common comprehensive building energy estimation model, in calculations for energy standards and energy ratings in simple cases (Residential Buildings for example) – but caution should be used and one can expect some deviations between the calculated and the actually achievable energy efficiency. It is shown that in the hottest (almost cooling only) region the difference between the two models is actually smaller than in other regions with both heating and cooling.

It is desirable to integrate in the monthly ISO 13790 method a way to account for night ventilation – an imperative for some climates where cooling is at least or more important than heating. The present method in ISO 13790 for taking into account night ventilation is not always appropriate for climates where cooling is the predominant consideration – since the difference between the night and the day temperature is not properly taken into account. In addition – the latent heat should also be considered, using the ISO standard currently under preparation, in hot and relatively humid climates – since it can easily account for 30% or more of the cooling energy – and cannot be reduced by the usual passive cooling strategies of shading and night ventilation.

Acknowledgements

The advice and help of Dr. Rokia Raslan, Architect Y. Schwartz and Prof. T. Oreszczyn of University College, London and of Prof. E. Erell of the Desert Research Institute, Ben-Gurion University of the Negev, Israel, are gratefully acknowledged.

References

Crawley, D. B., Hand, J. W., Kummert, M. and Griffith, B. T. 2005. "Contrasting the capabilities of building energy programs programs." *US DOE, University of Strathclyde and University of Wisconsin.*

Kalema, T., Johanesson, G., Hagengran, P. and Elmarsson, B. 2008. Accuracy of energy analysis of buildings: A comparison of a monthly energy balance method and simulation methods in calculating the energy consumption and the effect of thermal mass. *Journal of Building Physics* 32, p. 101-130.

Kokogiannakis, G., Strachan, P. and Clarke, J. 2008. Comparison of the simplified methods of the ISO 13790 standard and detailed modelling programs in a regulatory context. *Journal of Building Performance Simulation* 1, p. 209-219.

Raslan, R. and Davies, M. 2010. Results variability in accredited building energy performance compliance demonstration software in the UK: an inter-model comparative study. *Journal of Building Performance Simulation* 3, p. 63-85.

Raslan, R. and Davies, M. 2012. Legislating building energy performance: putting EU policy into practice. *Building Research & Information* 40, p. 305-316.

Schwartz, Y. and Raslan, R. 2013. Variations in results of building energy simulation tools, and their impact on BREEAM and LEED ratings: A case study. *Energy and Buildings* 52, p. 350-359.

Summerfield, A., Raslan, R., Lowe, R. and Oreszczyn, T. 2011. How useful are building energy models for policy? A UK perspective. *IBPSA* 12, p. 2477-2482.

Zhou, X., Hong, T., Yan, D. 2013. Comparison of Building Energy Modeling Programs: HVAC Systems. *Ernest Orlando Lawrence Berkeley National Laboratory* LBNL-6432E (2013).

Electrochemical Healing Techniques for Concrete Reinforcement Restoration

By Tomas Lovasi[*]
Sarka Msallamova[†]
Milan Kouril[‡]

Electrochemical chloride extraction (ECE) from a reinforced concrete structure may be accompanied with an electrochemical injection of healing agents (EICI) if such agents are positively charged and are able to migrate towards the activated reinforcement. Positive charge carrying nanoparticles or cationic corrosion inhibitors might be the proper choice. Organic substances with a positive charge and their salts are mostly such inhibitors. In this study, critical concentration of chlorides was investigated for fresh and carbonated concrete pore solution. Corrosion inhibition efficiency was evaluated by means of polarization resistance as a measure of corrosion rate. Sodium nitrite was taken as a reference corrosion inhibitor. As a second objective were migration tests. ECE and EICI were performed in order to test the migration ability of promising cation corrosion inhibitors, namely tetrabutylammonium bromide and tetrabutylphosphonium bromide. Concentration profile of the inhibitors and chlorides was investigated in the testing concrete blocks. The best results have been obtained for tetrabutylammonium bromide.

Keywords: *Chloride Extraction, Concrete, Corrosion, Electrochemical Injection.*

Introduction

Corrosion of steel in concrete is a major threat to structure, especially when it is caused by chloride ions. As a result of such attack, premature failure of the reinforced concrete structure may occur. Steel embedded in chloride-free Portland cement concrete can have high corrosion resistance. The reason is that concrete provides an alkaline environment that protects steel from corrosion. This corrosion resistance consists of passive layer, which covers the steel surface after insertion into fresh concrete. Such a protective film is stable in the highly alkaline environment of fresh concrete, the pH of which is in the range of about 12.5-13.8. At such a high pH range there is availability of free oxygen in the concrete that contributes to retain; the steel is in a passive state. If the steel is placed in concrete under such conditions, corrosion rate is negligible. The main cause of passive layer break down is carbonation of the concrete and penetration of chloride ions in to the steel surface (Orellan et al., 2004). During the carbonation process, carbon dioxide penetrates through the concrete, dissolves in the concrete pore solution; and reacts

[*]Student, University of Chemistry and Technology, Czech Republic.
[†]University of Chemistry and Technology, Czech Republic.
[‡]University of Chemistry and Technology, Czech Republic.

with calcium hydroxide to produce calcium carbonate. This reaction (Equation 1) leads to a reduction in the alkalinity of the concrete (Ihekwaha et al., 1996).

$$Ca(OH)_2 + CO_2 \rightarrow CaCO_3 + H_2O \quad (1)$$

This process does not have a significant impact on corrosive rate. Carbonation leads to changes in the structure of the concrete and the water and ions permeability (Ihekwaha et al., 1996).

Conduction of chloride ions into the concrete has little effect on pH change, but their presence affects the breakage of the protective layer on the steel surface. While carbonation is more likely to lead to even corrosion, chloride ions concentrate on specific locations where they indicate pitting corrosion, as to shown in the Figure 1.

Figure 5. *Types of Steel Corrosion in Concrete (Vavpetic, 2008)*

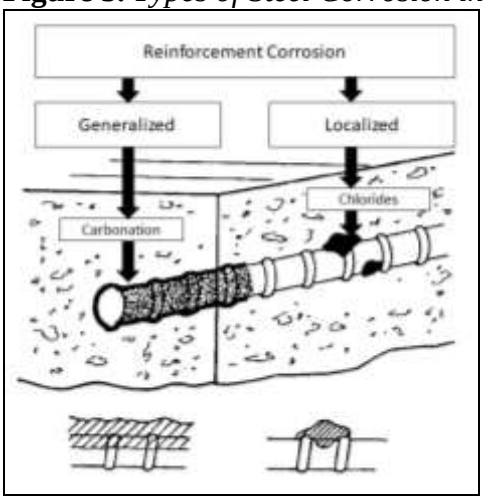

The steel corrosion process is an electrochemical process in which certain requirements must be met. One of them is a sufficient amount of dissolved oxygen, which is needed to react at cathode sites. Another requirement is to withhold moisture to maintain low electrical resistance in the concrete between the anode and the cathode sites (Karthick et al., 2016). After the initiation of the corrosion, the electrochemical process of the corrosion itself can lead to an overall deterioration of the reinforced concrete structure (Soylev and Richardson, 2008). Depending on the pH close to the steel surface and the availability of oxygen, corrosion of the steel reinforcements proceeds according to the reactions mentioned in Ormellese et al., 2009. Oxygen is the most harmful in this process, because without oxygen the steel reinforcement is not subject to corrosion even in the presence of aggressive ions (Ormellese et al., 2009).

During corrosion already iron corrodes, respectively oxidizes, at the anode to form ferric ions and releases two electrons (Garcia et al., 2012; Miranda et al., 2006).

$$Fe \rightarrow Fe^{2+} + 2e^{-} \quad (2)$$

Released electrons flow through the steel and are combined with the presence of oxygen or humidity at the cathode to form hydroxide ions (Miranda et al., 2006; Lovasi et al., 2017).

$$H_2O + 1/2O_2 + 2e^- \rightarrow 2OH^- \quad (3)$$

The hydroxide ions further react with ferrous ions at the anodes to form the ferrous hydroxide

$$Fe^{2+} + 2OH^- \rightarrow Fe(OH)_2 \quad (4)$$

Subsequently, the ferrous hydroxide can react in the presence of water to form ferric hydroxide $Fe(OH)_3$ and ferric oxide Fe_2O_3. It is possible that species other than those mentioned above may be formed. As a result of these reactions, the corrosion products occupy a larger volume than the original (primary) steel, resulting in cracking or crumbling of the concrete after its tensile strength has been exceeded. The most common chloride ions come from marine environments and from mixtures that are used for road maintenance in winter (Shi et al., 2012; Fajardo et al., 2016; Yeih et al., 2006). Such accumulated chloride ions can initiate corrosion of the steel rebars if their concentration in concrete exceeds a threshold level. In various published literature, the threshold level of chloride ions is within a wide range of values (Page et al., 1986). Under normal conditions, the chloride ion threshold typically ranges from 0.2% to 0.5% by weight of cement (Gaidis, 2004; Angst et al., 2009).

In concrete, chloride ions can migrate mainly by three mechanisms. Natural diffusion, electrical migration and transport through the pore solution due to capillary forces or external pressure gradient (Kouril et al., 2017). In concrete, chloride ions move primarily by natural diffusion. When using an external electric field, the chloride ions are moved by electrical migration. The natural diffusion of chloride ions depends primarily on their concentration gradient (Pan et al., 2008). Chloride-induced corrosion of the steel rebars may be alleviated by reducing the chloride ion level in concrete using various mechanisms (Miranda et al., 2007). During the corrosion of steel reinforcement, it is possible for chloride ions to migrate from local cathodes to local anodes within the generated electric field (Li and Page, 2000). Such an external electric field is most often applied to the controlled transport of chloride ions from concrete (Martinez et al., 2015). For example, electrochemical extraction of chlorides (ECE) may be a possible method (Elsener and Angst, 2007). It is possible to use cathodic protection, electrochemical chloride extraction mentioned, as well as electrochemical injection of a corrosion inhibitor (EICI) for the overall treatment of the reinforced concrete structure (Parthiban et al., 2008; Xu and Yao, 2011; Sawada et al., 2007). In order to alleviate corrosion caused by chloride ions, it is also possible to use effective chemical agents serving as corrosion inhibitors. Such inhibitors may be mixed into fresh concrete in new structures or applied to the surface, when such inhibitors are used to rehabilitate previously existing structures. In the latter case, it is

possible to use an external electric field to drive inhibitors into concrete (Kubo et al., 2008; Gong et al., 2018).

Cathodic protection uses lower current densities (15-20 m $A.m^{-2}$) that are maintained for a long period of time to prevent corrosion of the steel reinforcement in the concrete. This method also helps to prevent accumulation of chloride ions on the surface of the steel reinforcement (Pedeferri, 1996). At ECE, electric fields with a current density typically ranging from 1-5 $A.m^{-2}$ are applied to the concrete structure for several weeks (Liu and Shi, 2009). Within this time period, chloride ions migrate from concrete to an external solution mostly located on the surface of the concrete in which an external anode is incorporated (Herrera et al., 2006). By using a similar set-up as in ECE, the EICI can deliver the inhibitor via concrete to the steel surface while simultaneously removing chloride ions from the concrete. EICI is a relatively new method that has recently emerged as a promising solution to corrosion for reinforcing steel in concrete structures, and also as an effective method for the addition of corrosion inhibitors for rehabilitation measures to prevent or inhibit already exiting corrosion on the surface of the steel reinforcement (Nguyen et al., 2015; Daniyal and Raja, 2016).

This method has a number of advantages, such as a non-destructive character, is a "novelty" and requires only a temporary installation (a few days). At the beginning, high potential and current density were used 5-10 $V.cm^{-1}$ a 4.6 – 12.4 $A.m^{-2}$ (Asaro et al., 1990). Recently, the National Association of Corrosion Engineers (NACE) proposed a lower current density application. Current density values should not exceed 4 $A.m^{-2}$. Over time, the conditions for the experiment have improved. Nowadays, mostly reported current densities range between 0.5 and 5 $A.m^{-2}$ (Carmona et al., 2015). The Strategic Higway Research Program (SHRP) study resulted in a proposal of quaternary ammonium and phosphonium salts as corrosion inhibitors, which could be injected into the concrete by means of an electric field (Pan et al., 2008). These inhibitors are positively charged; i.e., they are cationic corrosion inhibitors. This study has proven, these corrosion inhibitors are able to reduce the adverse effects of chlorides in terms of corrosion and to provide adequate protection to steel reinforcement in concrete. Only a few new studies have been published since this study. The reason could be the high cost of corrosion inhibitors. Since then, several other studies have been conducted focusing on other types of corrosion inhibitors (Pan et al., 2008).

An example is a study examining the electromigration of two organic-based inhibitors, namely ethanolamine and guanidine (Sawada et al., 2005). In this study, the EICI process applies the electric field between a steel reinforcement embedded in concrete and the external anode (typically Ti mesh or stainless steel mesh) with a current density in the range of 1-5 $A.m^{-2}$ for 3-14 days. With the same conditions, experiments were performed by applying a corrosion inhibitor in the form of an external electrolyte. However, no electric field was used. Concentration profiles induce successful injection of both inhibitors. Better effects have been achieved in carbonated concrete where inhibitors were more concentrated around the steel reinforcement. In non-carbonated concrete, treatment with guanidine injection for 2 weeks at current density 5 $A.m^{-2}$ did not provide sufficient results. In this case, the inhibitor did not get deep enough. Even the injection of ethanolamine into non-

carbonated concrete was not significantly increased by used the electric field (Sawada et al., 2005).

In another study, Xu et al. (2016) performed laboratory tests using triethylentetramine in chloride-contaminated concrete samples. They have used a new method called bidirectional electromigration rehabilitation (BIEM). The electric field and the corrosion inhibitor were applied in the same way as at the standard EICI method. Electrochemical chloride extraction using a saturated solution $Ca(OH)_2$ as an external electrolyte was used as the reference experiment. After the treatment, the samples were drilled to determine concentration profiles of the chloride ions, hydroxide ions and corrosion inhibitor in the concrete. Using this technique, the author succeeded in reducing the chloride ions content and, after treatment, increased alkalinity in the concrete. The concentration of the corrosion inhibitor injected around the embedded steel rebars was sufficient to protect against corrosion. Kubo et al. (2013) in their contribution describe an electrochemical inhibitor injection test, which was applied to the 40-year old carbonated high-speed railway viaduct in Tokyo. The experiment found that the electrochemical injection of a corrosion inhibitor on an organic base, ethanolamine, was successful. An adequate amount of the inhibitor was penetrated into to existing railway viaduct. Inhibitor was near the steel surface for passivation of the steel in sufficient concentration under the conditions under study.

However, these methods can be used only for concrete with increased porosity. These are older constructions, where new types of concrete have not been used yet. For High Performance Concrete and Ultra High Performance Concrete, these methods are not expected to be used. The reasons are that these types of concrete have very low porosity and reduces transport of corrosive media (chloride, water, CO_2, O_2) in material.

The aim of this study was to investigate the corrosion inhibition efficiency of tetrabutylammonium bromide and tetrabutylphosphonium bromide as a corrosion inhibitor with prospective cationic action in alkaline concrete environment and compare their efficiency with commercially used corrosion inhibitor. Subsequently, their migration ability in concrete was proved. Other corrosion inhibitors have been evaluated in our study (Kouril et al., 2017).

Experimental Part

Model Solutions and Corrosion Inhibitors

As a model solution, a concrete pore solution of calcium hydroxide with pH value of 13 (adjusted with sodium hydroxide) was used to simulate the environment of fresh concrete. The other solution, a saturated solution of calcium carbonate with pH value of 8 was used. This solution simulates the environment of carbonated concrete. The sodium chloride was added to the saturated solution of calcium carbonate at various concentrations. To the calcium hydroxide solution, sodium chloride was added in one concentration and corrosion inhibitors were

added at two different concentrations. The particular concentrations of chloride anions and/or corrosion inhibitors are shown in Table 1.

Table 1. *Composition of the Model Solutions*

Solution	Cl^- content	Inhibitor content
$Ca(OH)_2$	15 $g.l^{-1}$	0.423 $mol.l^{-1}$
		2.115 $mol.l^{-1}$
$CaCO_3$	0 $g.l^{-1}$	0.423 $mol.l^{-1}$
	0.1 $g.l^{-1}$	
	1 $g.l^{-1}$	
	10 $g.l^{-1}$	

During the experiment, two cationic corrosion inhibitors and a reference inhibitor (sodium nitrite) as a representative of a well-established corrosion inhibitor for concrete were tested. All related information is summarized in Table 2. During the experiment, concentration of 0.423 $mol.l^{-1}$ for solution was used. This concentration was determined from the critical chloride content for activation of corrosion process. The value of critical chloride content is 0.4 weight % of Cl^- per cement, which corresponds approximately to 15 $g.l^{-1}$ or 0.423 $mol.l^{-1}$ of Cl^- in concrete pore solution at normal humidity. Sodium nitrite was used only for the calcium hydroxide solution. Since this inhibitor is largely commercially used (in most cases as an additive to fresh concrete), it was not an objective to further test its inhibitory efficacy.

Table 2. *Corrosion Inhibitors used in the Tests*

Name	Chemical purity [%]	Molar Weight [$g.mol^{-1}$]	pH of solution	Supplier
Sodium nitrite	≥ 99.0	69.00	9	Sigma - Aldrich
Tetrabutylammonium bromide (ReagentPlus®)	≥ 99.0	322.37	6.9	
Tetrabutylphosphonium bromide	98.0	339.33	4.9	

Concrete Specimens

Real concrete specimens were used for an experiment of migration ability for both corrosion inhibitors. For the preparation of a cubic meter of OPC concrete specimens the components listed in Table 3 were used. From this mixture, concrete cylinder specimens (100 mm in diameter and 50 mm in height) were cast. The specimens were kept in water for 28 days. Afterwards, the specimens were dried at 105 °C overnight to stabilize their weight. Unexposed surface of the specimens was painted by a synthetic paint, IZOBAN (Detecha). Poor quality concrete was chosen on purpose to accelerate the transport processes. Water-to-

cement ratio corresponded to 0.8. This value corresponded to low quality of concrete.[1]

Table 3. *Composition of OPC Concrete Cubic Meter*

Components	**Mass [kg]**
Cement (grade CEM I 42.5R)	262
Water	210
Sand (grain size 4-8 mm)	1150
Aggregate (grain size 4-8 mm)	291
Aggregate (grain size 8-16 mm)	582

Steel Specimens

The carbon steel (W.Nr. 1.0330), a ferritic-perlite steel (Figure 2) with elements content: 0.045% C, 0.382% Mn, 0.007% P, 0.009% S, was used.[2] This carbon steel was cut in the form of strips 35 x 175 mm. Subsequently, these strips were degreased with a 10% sodium hydroxide solution. Subsequently, the samples were thoroughly washed with distilled water after pickling with a 5% hydrochloric acid. The surface was polished with sandpaper P180 and rinsed with ethanol prior to exposure.

Figure 6. *Microstructure of Carbon Steel*

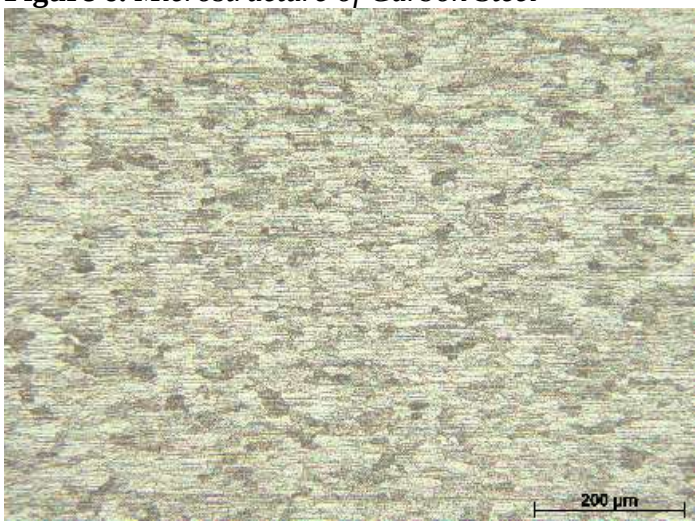

[1]http://www.concretecountertopinstitute.com/the-importance-of-watercement-ratio/.
[2]https://online.ferona.cz/detail/23985/plech-valcovany-za-studena-k-tvareni-za-studena-en-10131-rozmer-2x1250x2500.

Electrochemical Measurements

For Testing in Model Solutions

Polypropylene corrosion cells were fastened onto the non-corroded steel specimens. The cells were filled with different solutions (approximately 5 ml) one after the other. Firstly, saturated calcium hydroxide solution and calcium carbonate, or both solutions were used. After 24 hours, the corrosion cells were emptied and filled with a new solution that differs only in chloride anions content. After another 24 hours, the solution was replaced by a new solution, which contained chloride anions and a corrosion inhibitor.

At the defined time interval, after 24 hours after the corrosion cells were filled with the solution, the polarization resistance was measured as shown in Figure 3. A reference electrode with the counter electrode was immersed in the solution. The reference electrode was a saturated calomel electrode (SCE) and platinum wire (CE) was used as the counter electrode. The exposed area was 2.81 cm^2. The polarization resistance was measured within ± 20 mV from an open circuit potential (E_{oc}) with a scan rate of 0.1 mV/s. The polarization resistance value was then determined from the slope of the curve within ± 5 mV from E_{oc}. Among the measurements, the corrosion cells were closed to prevent carbon dioxide from being absorbed from the air. The resulting polarization resistance value was determined an average of five measurements. Inaccuracies of individual measurements were displayed as error bars in graphics processing.

Figure 7. *Configuration of the Corrosion Cells*

Testing of Migration Ability

The concrete specimen was fixed in between two chambers with the volume of 0.5 liters. Stainless steel mesh were built in the chamber parallel to both flat surfaces of the concrete specimen at a distance of approximately 3 mm, as shown in Figure 4.

Figure 8. *Experimental Cell for Electrochemical Treatment*

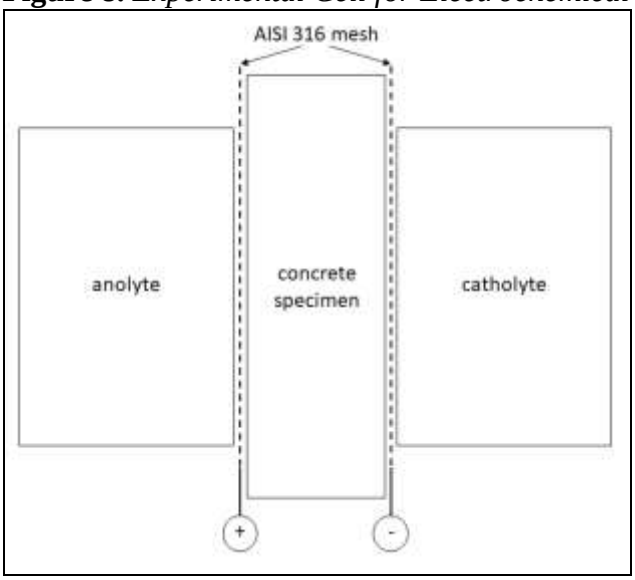

The catholyte chamber (Figure 5, right side) was filled with 3% NaCl solution and the anolyte chamber was filled with solution of corrosion inhibitors. Galvanostatic mode was used for electrochemical injection of corrosion inhibitor with simultaneous electrochemical chloride extraction. Constant current with values of 2.53 mA and 16.65 mA was applied between stainless steel mesh electrodes for 7 days. These values correspond to current density of 1 $A.m^{-2}$ or 5 $A.m^{-2}$. Constant current was introduced by a Radelkis OH-404/A potentiostat, which was used as galvanostat. The current flow was measured with a METEX M 3650 multimeter and recorded with a METEX Control Software Client every 5 minutes. The resulting voltage was recorded using a IEC1010-1 voltmeter. In addition to the migration tests, the so-called plain diffusion was performed. The diffusion experiment was set exactly in the same way as the electrochemical injection, but no current was used.

Figure 9. *3D Model of Corrosion Cell*

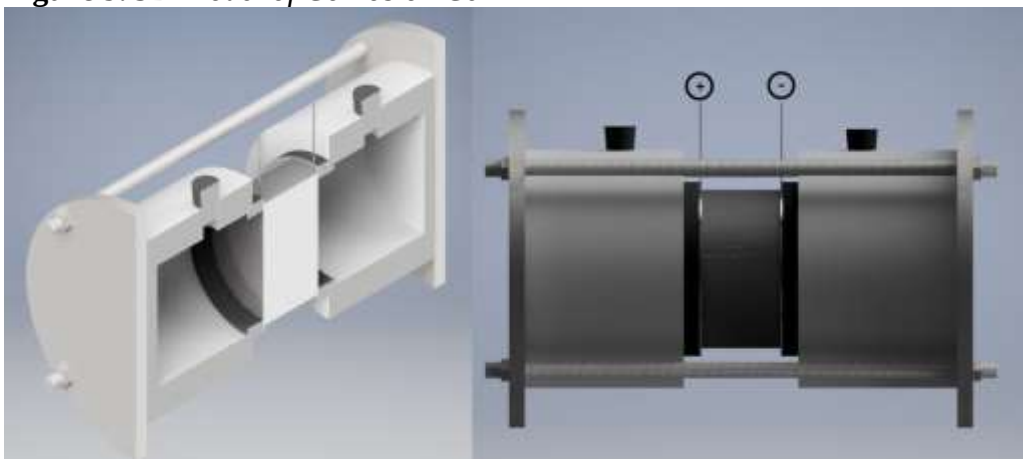

Analysis Method

After the injection and/or extraction or diffusion, two 5 mm thick slices were taken from the catholyte side of the concrete cylinder. Three 5 mm thick slices were taken from the anolyte side (Figure 6). The concentration profile of the injected corrosion inhibitor and chloride anions was determined by analysing these slices. The slices were pulverized using a laboratory mill. The powder was dried at 80 °C overnight. 20 grams of the powder was then mixed with 50 ml of distilled water and the mixture was ultrasonicated for one hour. The liquid phase was separated from the solid by means of centrifugation and analyzed. The guanidine concentration was determined using a mass spectrometer, LC-MS LTQ-Orbitrap Velos. The chloride concentration was determined using an absorption spectrophotometer, FIA lab 2000. The concentration profile obtained by electrochemical injection was compared with that resulting from a plain diffusion.

Figure 10. *The Analyzed Parts of the Sample*

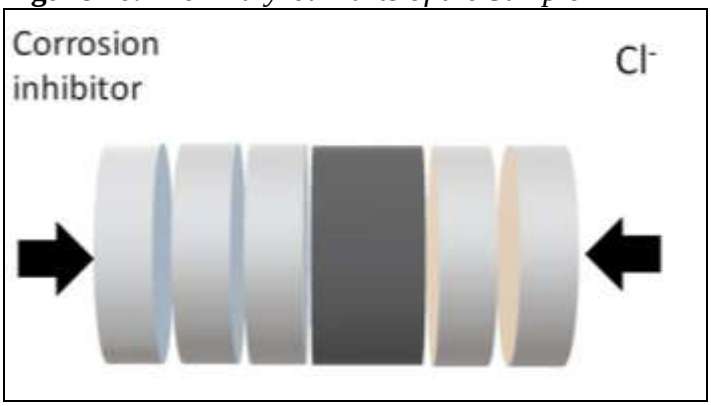

Results and Discussion

Polarization Resistance

Calcium Hydroxide Solution

In solution simulating fresh concrete, the polarization resistance values were in tens of $\Omega.m^2$. Such high values indicate the passive state of carbon steel in chloride-free model solution. The values of the open circuit corrosion potential also correspond to the passive state of the steel. Negligible corrosion rate is thus expected. After addition of the chloride anions to the base solution, the polarization resistance values are declined by an order of magnitude, as shown in Figure 7.

Figure 11. *Fresh Concrete Pore Solution with Two Levels of Corrosion Inhibitors and 15 g.l^{-1} Cl^{-}*

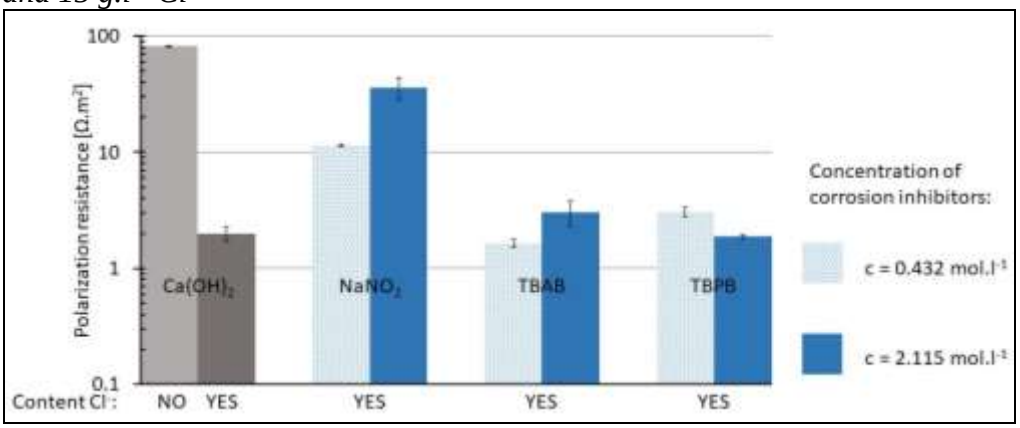

The decrease in the values of the polarization resistance was followed by a decrease in the open circuit corrosion potential; the values of which shifted to negative values. By adding a corrosion inhibitor to solution containing chloride anions, it was assumed that the passive state of the steel could be restored. When tetrabutylammonium bromide (TBAB) was applied at a 1:1 concentration, no significant increase in polarization resistance was recorded. When increasing the corrosion inhibitor concentration five times, there was a slight increase in polarization resistance, but this increase was only two-fold compared to the previous concentration. Using tetrabutylphosphonium bromide (TBPB), the opposite effect was observed. At a higher concentration of corrosion inhibitor, the polarization resistance decrease by one third. The low polarization resistance values for both tetrabutylammonium bromide and tetrabutylphosphonium bromide responded to open circuit corrosion potential values ranging from -490 mV to -570 mV (Figure 8).

Figure 12. *Open Circuit Potential for Fresh Concrete Pore Solution with Content Corrosion Inhibitors and Chloride Ions*

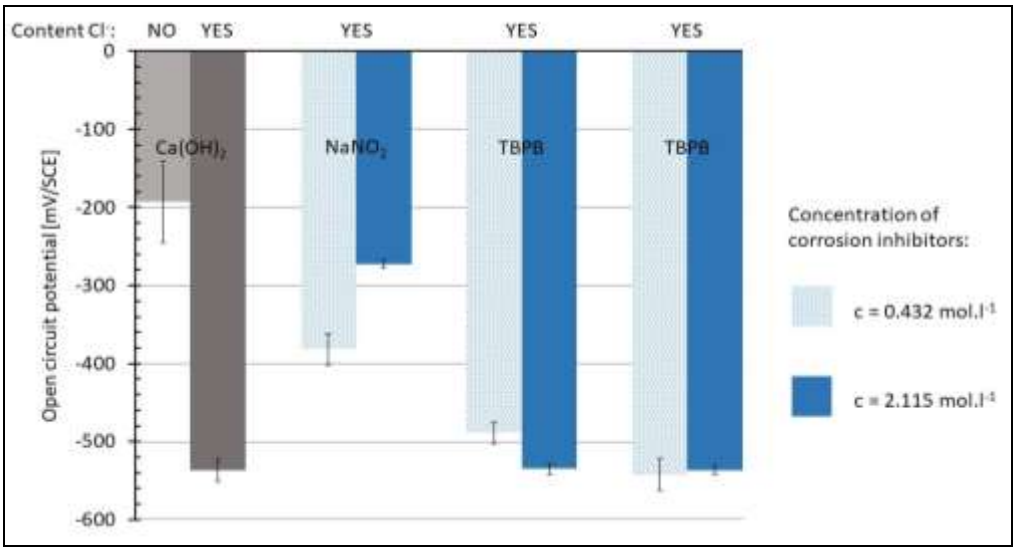

Calcium Carbonate Solution

As expected, the calcium carbonate solution activates the steel immediately after the start of the experiment. The reason is the low pH of the solution as compared to the calcium hydroxide solution. In this solution, steel does not have the ability to form a protective layer composed of stable oxide on its surface; thus, depassivation was observed as shown in Figure 9. The value of polarization resistance decreases to multiples of 10^0 of $\Omega.m^2$ in this environment without corrosion inhibitor. When the chloride ions content increase, the polarization resistance decreased to lower values than those measured with the basic solution. However, when corrosion inhibitors were added to the basic solution, the value of polarization resistance slightly increased. However, there was no significant change in polarization resistance values. After addition of the chloride anions in concentration $0.1 g.l^{-1}$ to the calcium carbonate solution with content corrosion inhibitor, a slight decrease in the values of the polarization resistance for tetrabutylammonium bromide was observed, while a slight rise in the polarization resistance values was observed in the case of tetrabutylphosphonium bromide.

Figure 13. *Polarization Resistance of Steel in Carbonated Concrete Pore Solution with Content 0.1 g.l^{-1} Chlorides*

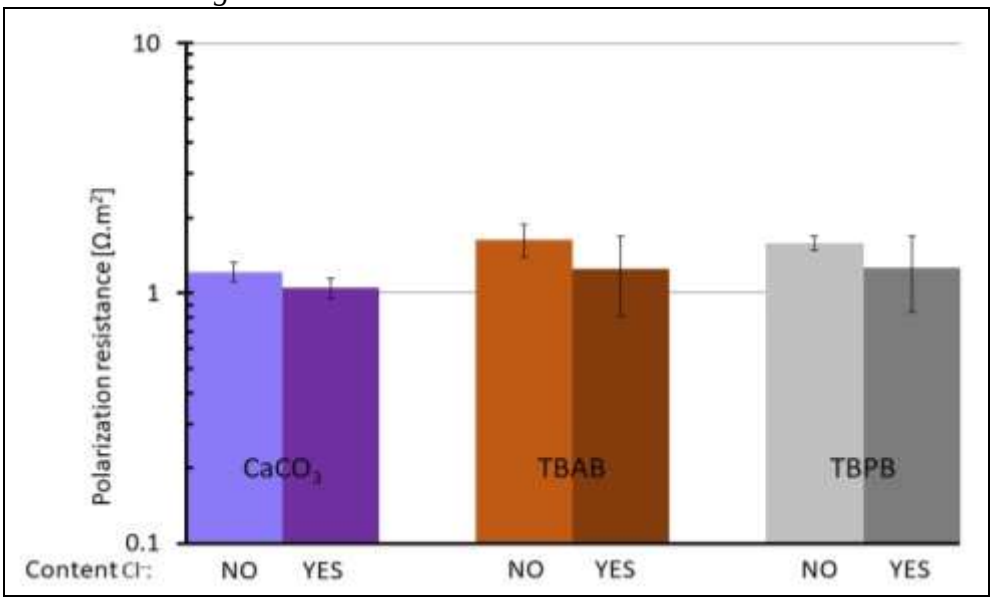

The gradual increase in chloride ion concentration ($1 g.l^{-1}$) in calcium carbonate solution resulted in a decrease in the polarization resistance value of both the basic solution and the tetrabutylammonium bromide (Figure 10). However, the values of the polarization resistance of tetrabutylphosphonium bromide remained constant at the concentration of chloride anions of $1 g.l^{-1}$ as well as in $0.1 g.l^{-1}$. However, after increasing the concentration of chloride ions ten-fold, none of the inhibitors tested showed significant polarization resistance (Figure 11). However, some inhibition was detected. What remains unanswered is whether the transport of such a corrosion inhibitor might be accelerated by

electrochemical injection into chloride contaminated and/or carbonated concrete while chlorides are being extracted from the concrete and/or the concrete surrounding the depassivated steel realkalizes. Another question is whether its effectiveness increases when chloride ions are removed from the surface of the steel using electrochemical extraction.

Figure 14. *Polarization Resistance of Steel in Carbonated Concrete Pore Solution with Content 1 g.l^{-1} Chlorides*

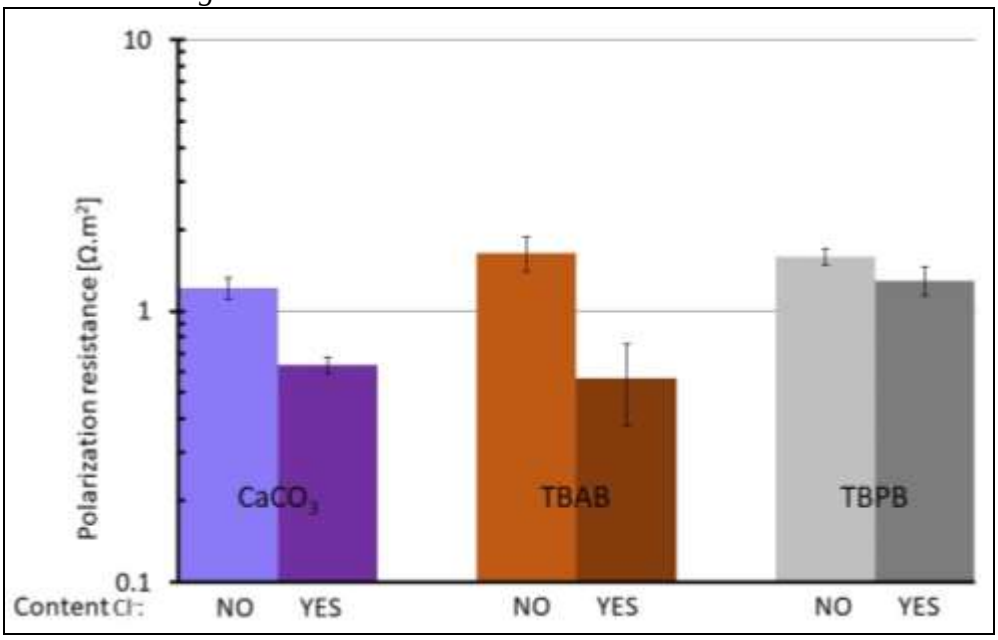

Figure 15. *Polarization Resistance of Steel in Carbonated Concrete Pore Solution with Content 10 g.l^{-1} Chlorides*

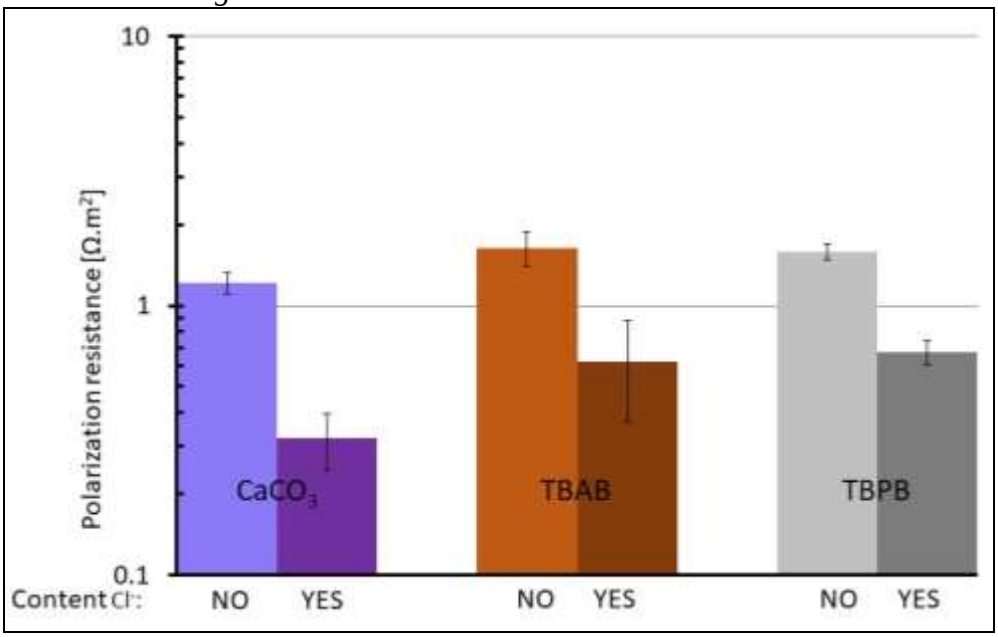

Migration Ability

Chloride Extraction

The process of chloride extraction (Figures 12 and 13) has been significantly affected by the use of an electric field. While in the test of plain diffusion, the concentration values were low, (was in the other of 10^0 mmol.l^{-1}; concentration of chloride ions or inhibitor in the extract). Using tetrabutylammonium bromide, the concentration of chloride ions after the diffusion test is low and uniform throughout the whole sample. Using tetrabutylphosponium bromide the increase chloride concentration was detected only in the surface layer and further sections contained only the original amount of chloride ions. An increase values of concentration of chloride ions to tens mmol.l^{-1} occurred, when current density 1 and 5 A.m^{-2} was applied. At a current density of 1 A.m^{-2}, the concentration was significantly higher at the surface layer of the sample compared to diffusion for both corrosion inhibitors. However, at a depth of 35 mm or more, the concentration of chloride ions was very similar to those detected after diffusion. At the highest current density used, chloride ions were able to get through the whole sample at a relatively high concentration, up to approximately, 7 mmol.l^{-1}. By using this current density, it was possible to get the largest amount of chloride ions through the sample.

Figure 16. *Concentration Profile of Cl^- after Application of TBAB*

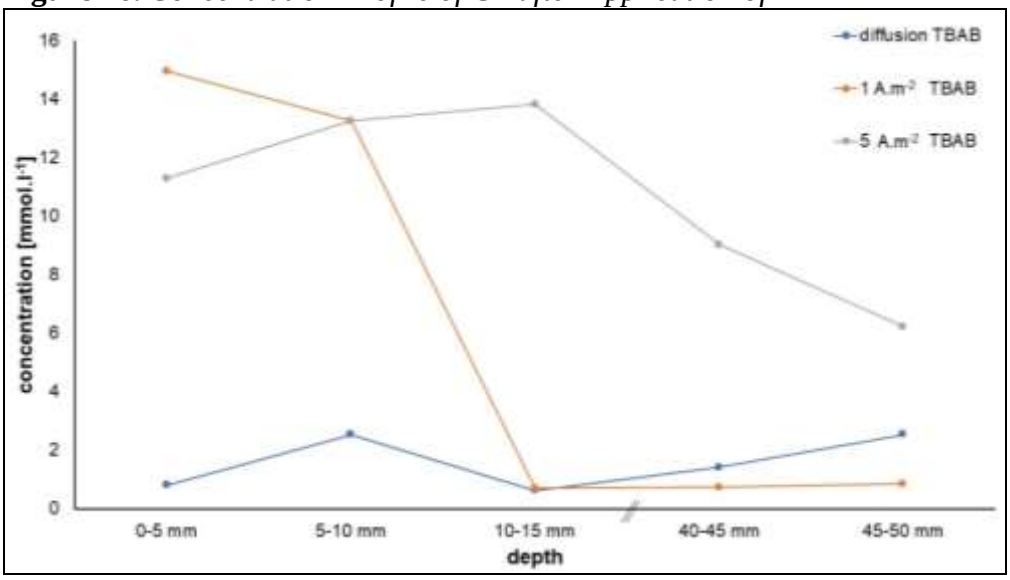

Figure 17. *Concentration Profile of Cl^- after Application of TBPB*

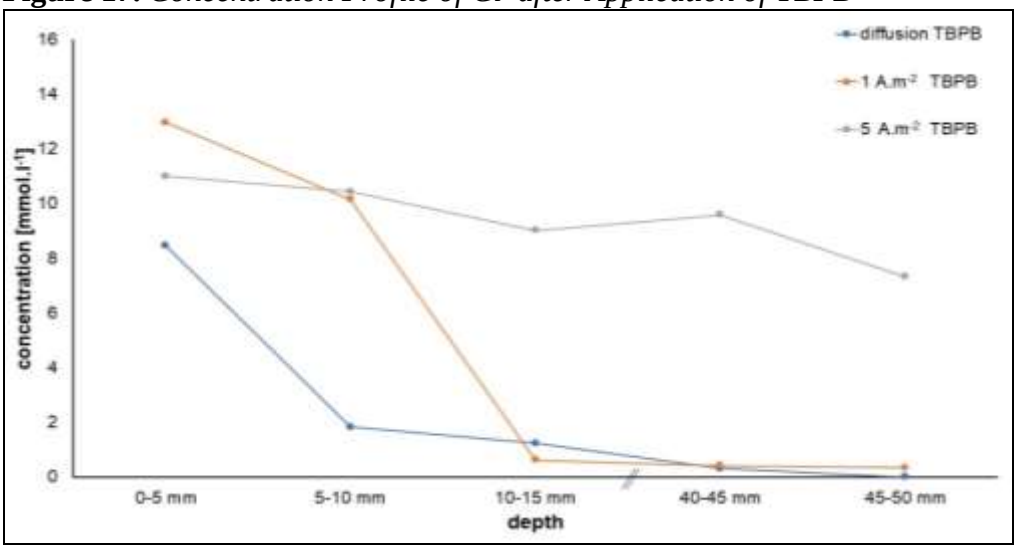

Injection of Corrosion Inhibitors

With regard to tetrabutylammonium bromide, it was injected only within 10 to 15 mm of the sample surface. At greater depth, the inhibitor was not detected. Figures 14 to 16 show the concentration profiles for the particular test methods. As mentioned, the samples were subjected to electrochemical chloride extraction with simultaneous electrochemical injection of a corrosion inhibitor for seven days. As can be seen, during diffusion (Figure 14), the inhibitor concentration on the surface of the sample is quite high, but the tetrabutylphosphonium bromide concentration is almost five times smaller. From the surface, the concentration decreases rapidly (at tetrabutylammonium bromide) and is almost undetectable in the other sections.

Figure 18. *Concentration Profile of TBAB and TBPB after Diffusion for Seven Days*

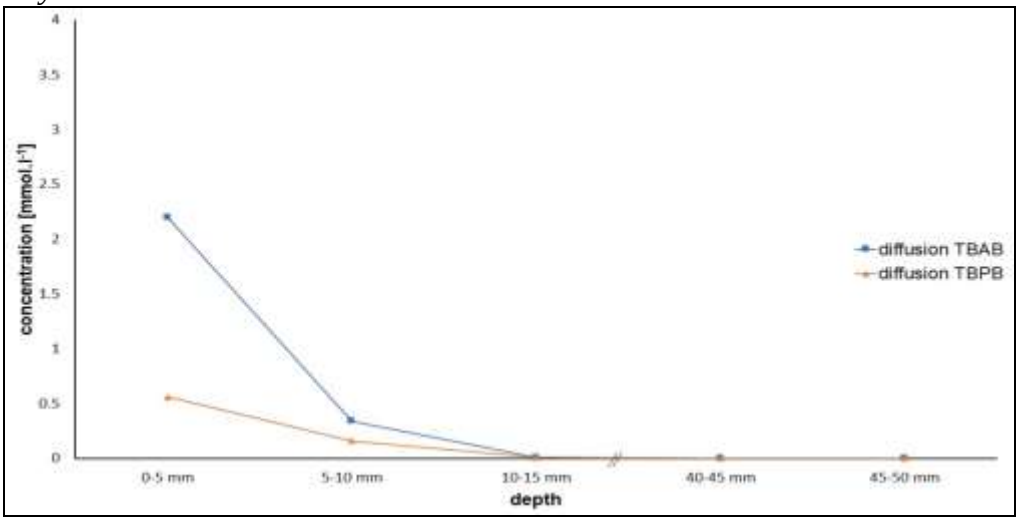

When using a current density of 1 A.m^{-2}, the concentration of tetrabutylammonium bromide on the surface of the sample is almost two times higher compared to diffusion (Figure 15). Considering only diffusion, better results were obtained in the case of tetrabutylammonium bromide. Using a current density of 1 A.m^{-2}, there was no significant change when using the tetrabutylphos-phonium bromide. The concentration of the inhibitor was very similar to the application without an electric field. In the second and third sections, the concentration gradually decreases.

Figure 19. *Concentration Profile of TBAB and TBPB after Application Current Density 1 A.m^{-2} for Seven Days*

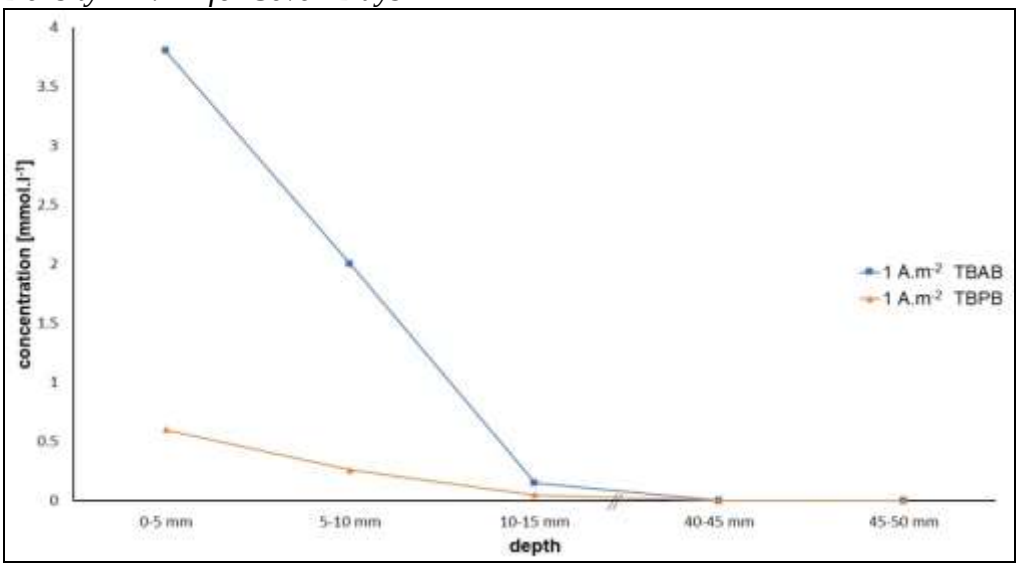

Figure 20. *Concentration Profile of TBAB and TBPB after Application Current Density 5 A.m^{-2} for 7 Days*

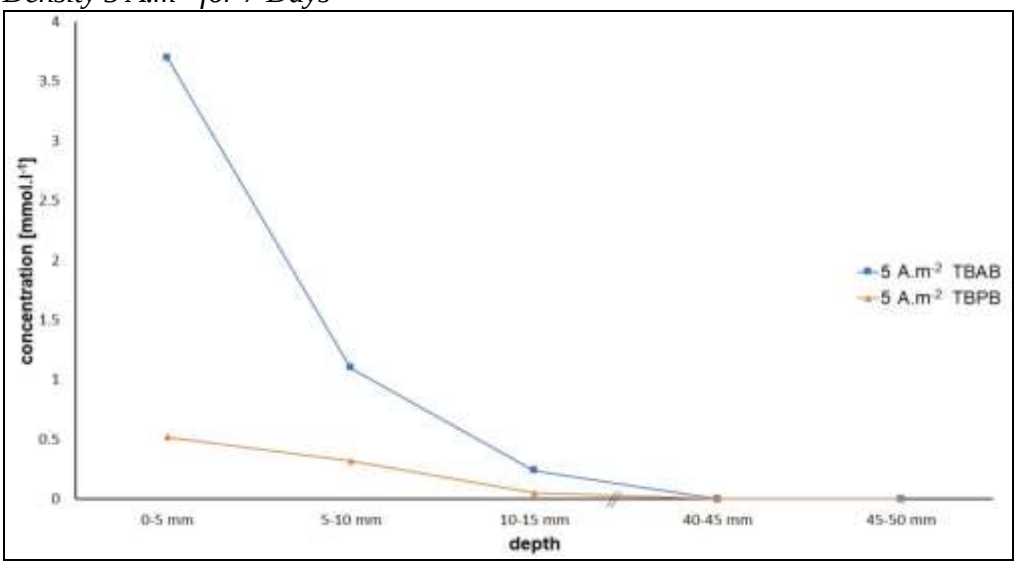

The transport was not significantly affected by migration, when the current density of 5 $A.m^{-2}$ was used (Figure 16). The inhibitors were also identified in a section 10 to 15 mm distant from the concrete surface. The results proved that tetrabutylammonium bromide is transportable by migration in fresh concrete, but for tetrabutylphosphonium bromide this property was not proven. With respect to the tetrabutylphosphonium bromide, no significant changes have been observed here, either in spontaneous diffusion or in the application of the electric field. The values of concentration of tetrabutylphosphonium bromide were approximately the same for all three methods tested.

Conclusions

Electrochemical measurements have demonstrated low efficiency of both corrosion inhibitors. Nevertheless, better results were achieved using TBAB. The behavior of this inhibitor in a pore solution of fresh concrete was better compared to TBPB. TBAB reached higher polarization resistance values at increased concentration. It is assumed, that the inhibitor's effectiveness was influenced by the presence of bromides, which have similar effect as chloride anions. Since bromide belongs to the group of aggressive elements, it is also Cl or S. These may result in more aggressive substances in the solution which interfere with the formation of a passive layer on the steel surface. The final result is therefore a solution of 0.423 $mol.l^{-1}$ of bromides to which Cl is still attached.

In the second part, tetrabutylammonium and tetrabutylphosphonium cathions have demonstrated their ability to migrate in the alkaline environment of concrete. Their transport can be efficiently accelerated by the action of an electric field where the anode is placed on the surface of the reinforced concrete structure in the inhibitor solution and the cathode is a steel reinforcement in the chloride contaminated concrete. At the same time, electrochemical injection of a corrosion inhibitor and electrochemical extraction of chlorides may occur. The lowest increase in inhibitor concentration in concrete was observed in the case of tetrabutylphosphonium cation, using a current density of 1 and 5 $A.m^{-2}$. On the other hand, the largest concentration was observed in the case of tetrabutylammonium cation, when the concentration of corrosion inhibitor in the surface layer was approximately four times higher in comparison with tetrabutylphosphonium.

Acknowledgments

The authors gratefully acknowledge the support by the Czech Science Foundation in the frame of the research project 16-11879S.

References

Angst, U., et al. Critical chloride content in reinforced concrete — A review. Cement and Concrete Research. 2009. vol. 39, no. 12, pp. 1122-1138.

Asaro, M. F., et al. Electrochemical chloride removal and protection of concrete bridge components (injection of synergistic corrosion inhibitors). No. SHRP-S-310. 1990. pp. 53.

Carmona, J., et al. Shape Effect Of Electrochemical Chloride Extraction In Structural Reinforced Concrete Elements Using A New Cement-Based Anodic System. Materials. 2015. vol. 8, pp. 2901-2917.

Daniyal, Md. and Raja, Md. A. Use of Corrosion Inhibitors for Steel Protection in Cementitious Composites-A Review. 2016. vol. 3, no. 6, pp. 171-175.

Elsener, B. and Angst, U. Mechanism of electrochemical chloride removal. Corrosion Science. 2007. vol. 49, no. 12, pp. 4504-4522.

Fajardo, G., Escadeillas, G., Arliguie, G. Electrochemical chloride extraction (ECE) from steel-reinforced concrete specimens contaminated by "artificial" sea-water. Corrosion Science. 2006. vol 48, no. 1, pp. 110-125.

Gaidis, J. M. Chemistry of corrosion inhibitors. Cement and Concrete Composites. 2004. vol. 26, no. 3, pp. 181-189.

García, J., et al. Effect of cathodic protection on steel–concrete bond strength using ion migration measurements. Cement and Concrete Composites. 2012. vol. 34, no. 2, pp. 242-247.

Gong, J., et al. Electrochemical Chloride Extraction and Inhibitor Injection in Salt-Contaminated Repair Mortar. International Journal of Electrochemical Science. 2018. vol. 13, pp. 498-513.

Herrera, J. C., Escadeillas, G., Arliguie, G. Electro-chemical chloride extraction: Influence of C_3A of the cement on treatment efficiency. Cement and Concrete Research. 2006. vol. 36, pp. 1939-1946.

Ihekwaha, N. M., Hope, B. B., Hansson, C. M. Carbonation and electrochemical chloride extraction from concrete. Cement and Concrete Research. 1996. vol. 26, vo. 7, pp. 1095-1107.

Karthick, S. P., et al. Electrochemical process to improve the durability of concrete structures. Journal of Building Engineering. 2016. vol. 7, pp. 273-280.

Kouril, M., Lovasi, T., Msallamova, S., Nemecek, J., Sulc, R. Electrochemical injection of cathionic corrosion inhibitors. In ACSEE 2017. Sixth International Conference on Advances in Civil, Structural and Environmental Engineering. Rome, 2017. pp. 40-44.

Kubo, J., et al. Electrochemical inhibitor injection for control of reinforcement corrosion in carbonated concrete. Materials and Corrosion. 2008. vol. 59, no. 2, pp. 107-114.

Kubo, J., Tanaka, Y., Page, C. L., Page, M. M. Application of electrochemical organic corrosion inhibitor injection to a carbonated reinforced concrete railway viaduct. Construction and Building Materials. 2013. vol. 39, pp. 2-8.

Li, L. Y. and Page, C. L. Finite element modelling of chloride removal from concrete by an electrochemical method. Corrosion Science. 2000. vol. 42, pp. 2145-2165.

Liu, Y. and Shi, X. Electrochemical chloride extraction and electrochemical injection of corrosion inhibitor in concrete: state of the knowledge. Corrosion Reviews. 2009. vol. 27, no. 1-2, pp. 53-822.

Lovasi, T., Msallamova, S., Kouril, M., Jamborova, T., Stoulil, J., Nemecek, J., Sulc, R. Cathionic corrosion inhibitors for protection of steel in chloride contaminated

concrete. In METAL 2017: 26rd International Conference on Metallurgy and Materials. Brno, 2017, pp. 1361-1367.
Miranda, J. M. et al. Several questions about electrochemical rehabilitation methods for reinforced concrete structures. Corrosion Science. 2006. vol. 48, no. 8, pp. 2172-2188.
Miranda, J. M., et al. Limitations and advantages of electrochemical chloride removal in corroded reinforced concrete structures. Cement and Concrete Research. 2007. vol. 37, no. 4, pp. 596-603.
Martinez, I., et al. Chloride Electroremediation in reinforced structures: preliminary electrochemical tests to detect the steel repassivation during the treatment. Electrochimica Acta. 2015. vol. 181, pp. 288-300.
Nguyen, T. H., et al. Effect of Electrical Injection of Corrosion Inhibitor on the Corrosion of Steel Rebar in Chloride-Contaminated Repair Mortar. International Journal of Corrosion. 2015. vol. 2015, pp. 1-10.
Orellan, J. C., G. Escadeillas, G. Arliguie. Electrochemical chloride extraction: efficiency and side effects. Cement and Concrete Research. 2004. vol. 34, no. 2, pp. 227-234.
Ormellese, M., et al. A study of organic substances as inhibitors for chloride-induced corrosion in concrete. Corrosion Science. 2009. vol. 51, no. 12, pp. 2959-2968.
Page, C. L., et al. The influence of different cements on chloride-induced corrosion of reinforcing steel. Cement and Concrete Research. 1986. vol. 16, pp. 79-86.
Pan, T., Nguyen, T. A., Shi, X. Assessment of Electrical Injection of Corrosion Inhibitor for Corrosion Protection of Reinforced Concrete. TRB Annual Meeting 2008, Washington D.C.
Parthiban, G. T., et al. Cathodic protection of steel in concrete using magnesium alloy anode. Corrosion Science. 2008. vol. 50, no. 12, pp. 3329-3335.
Pedeferri, P. Cathodic protection and cathodic prevention. Construction and Building Materials. 1996. vol. 10, no. 5, pp. 391-402.
Sawada, S., Page, C. L., Page, M. M. Electrochemical injection of organic corrosion inhibitors into concrete. Corrosion Science. 2005. vol. 47, no. 8, pp. 2063-2078.
Sawada, S., et al. Electrochemical injection of organic corrosion inhibitors into carbonated cementitious materials: Part 1. Effects on pore solution chemistry. Corrosion Science. 2007. vol. 49, no. 3, pp. 1186-1204.
Shi, X., et al. Longevity of corrosion inhibitors and performance of liquid deicer products under field storage. Canadian Journal of Civil Engineering. 2012. vol. 39, no. 2, pp. 117-127.
Söylev, T. A. and M. G. Richardson. Corrosion inhibitors for steel in concrete: State-of-the-art report. Construction and Building Materials. 2008. vol. 22, no. 4, pp. 609-622.
Vavpetič, V. Corrosion in concrete steel, seminar. University of Ljubljana, Faculty of mathematics and physics. 2008.
Xu, J., Yao, W. Electrochemical studies on the performance of conductive overlay material in cathodic protection of reinforced concrete. Construction and Building Materials. 2011. vol. 25, no. 5, pp. 2655-2662.
Xu, C., et al. Organic corrosion inhibitor of triethylenetetramine into chloride contamination concrete by eletro-injection method. Construction and Building Materials. 2016. vol. 115, pp. 602-617.
Yeih, W., Chang, J. J., Hung, C. C. Selecting an adequate procedure for the electrochemical chloride removal. Cement and Concrete Research. 2006. vol. 36, no. 3, pp. 562-570.